12-16-2014 12:00 AM

Wind and Thermal Effects on Ground Mounted Photovoltaic (PV) Panels

Chowdhury Mohammad Jubayer
The University of Western Ontario

Supervisor
Dr. Horia Hangan
The University of Western Ontario

Graduate Program in Civil and Environmental Engineering
A thesis submitted in partial fulfillment of the requirements for the degree in Doctor of Philosophy

Recommended Citation

Jubayer, Chowdhury Mohammad, "Wind and Thermal Effects on Ground Mounted Photovoltaic (PV) Panels" (2014). *Electronic Thesis and Dissertation Repository*. 2589.
https://ir.lib.uwo.ca/etd/2589

WIND AND THERMAL EFFECTS ON GROUND MOUNTED PHOTOVOLTAIC (PV) PANELS

(Thesis format: Integrated Article)

by

Chowdhury Mohammad Jubayer

Graduate Program in Engineering Science
Department of Civil and Environmental Engineering

A thesis submitted in partial fulfillment
of the requirements for the degree of
Doctor of Philosophy

The School of Graduate and Postdoctoral Studies
The University of Western Ontario
London, Ontario, Canada

ABSTRACT

A combination of Computational Fluid Dynamics (CFD) simulations and wind tunnel experiments are carried out to investigate the effects of wind on the aerodynamic loading and heat transfer of a ground mounted stand-alone photovoltaic (PV) panel with tilt angle of 25^o in open country atmospheric boundary layer. Several azimuthal wind directions are considered: Southern 0^o, Southwest 45^o, Northwest 135^o and Northern 180^o. Three dimensional Reynolds-Averaged Navier-Stokes (RANS) approaches with an unsteady solver using Shear Stress Transport (SST) k-ω turbulence closure are employed for the CFD simulations, whereas Particle Image Velocimetry (PIV) and Hot Wire Anemometry (HWA) methods are applied for the wind tunnel experiments. The mean wind flow fields obtained from PIV and CFD for the stand-alone PV system are compared and an overall reasonable agreement is found. Further on, the same CFD simulation approaches are employed to evaluate aerodynamic loading of an array of ground mounted PV panels.

For the stand-alone PV system, maximum mean uplift is observed for 180^o wind direction and maximum overturning moment for 45^o and 135^o wind directions. For 135^o and 180^o wind directions, higher level of turbulence on the leeward side of the panel are noticed based on the PIV experiment. Employing Hot Wire Anemometry, a weak shedding of vortices from the leading edge is detected only for the 180^o wind direction. For the array configuration, all trailing rows are completely in the wake of the first windward row for 0^o and 180^o wind directions, which results in lower mean wind loads (drag, lift and overturning moments) on the trailing rows. Higher overturning moments are found for all rows for 45^o and 135^o wind directions cases. From the heat transfer simulation for the stand-alone system, dominance of natural convection over forced convection is observed for Reynolds number of 1.0×10^5. A correlation between dimensionless convective heat transfer coefficient, Nusselt number and Reynolds number is established for 0^o and 180^o wind directions. This work provides a new and in-depth analysis of surface pressures and heat transfer rates correlated to the flow field around ground mounted PV panels.

Keywords: Solar (PV) panels, ground mounted, CFD, RANS, PIV, wind loading, heat transfer, atmospheric boundary layer, shedding of vortices.

CO-AUTHORSHIP STATEMENT

Chapter Two is published in the Journal of Wind Engineering and Industrial Aerodynamics under the co-authorship of Jubayer, C. M. and Hangan, H.

Chapter Three will be submitted for publication under the co-authorship of Jubayer, C. M., Hangan, H. and Siddiqui, K.

Chapter Four will be submitted for publication under the co-authorship of Jubayer, C. M. and Hangan, H.

Chapter Five will be submitted for publication under the co-authorship of Jubayer, C. M., Hangan, H. and Siddiqui, K.

ACKNOWLEDGMENTS

First, I would like to express my sincere gratitude to my research supervisor Dr. Horia Hangan for his guidance, support and encouragement throughout the course of this research. I would also like to thank him for believing in me and his openness to whatever ideas I had over the past four years.

I would also like to thank Dr. Kamran Siddiqui. His wide knowledge regarding PIV experiment and heat transfer provided a good basis for the thesis.

I was really fortunate to be surrounded by wonderful people who helped me in different stages of this research. I would like to extend my thanks to Dr. Maryam Refan, Dr. Ahmed Elatar, Adrian Costache, Gerry Dafoe, Dan Parvu and Ayodeji Abiola for helping me during the experiments. I greatly appreciate the help I received from Dr. Ashkan Rasouli and Ziad Boutanios while working on the CFD simulations. Special thanks to Djordje Romanic for reviewing the final version of the manuscript. I also thank Dr. Jeong Hee Oh, Nicholas Pratt, Fahad Akon, Zoheb Nasir, Andrew Mathers, Zeinab Samani and Ryan Kilpatrick for all the interesting discussion that we had over the past years. I am grateful to all my colleagues at the Wind Engineering, Energy and Environment (WindEEE) Research Institute and Boundary Layer Wind Tunnel Laboratory.

I would like to thank the Shared Hierarchical Academic Research Computing Network (SHARCNET:www.sharcnet.ca) and Compute/Calcul Canada for their facilities.

I would also like to acknowledge the financial support from the Department of Civil and Environmental Engineering at Western University, Ontario Centres of Excellence and

Natural Sciences and Engineering Research Council of Canada (NSERC) Discovery Grants.

Last but not the least; I owe my loving thanks to my wife Easmine Akter, my parents Mir Hossain Chowdhury and Jigar Khairun Nafia and my brother Chowdhury Mohammad Junayed. Without their encouragement and support it would not have been possible for me to finish this work.

DEDICATION

This thesis is dedicated to my only sister, Jinatun Safia Jainun, who lost her life in a road accident on April 13, 1998 at the age of 18. There isn’t a day goes by that I don’t miss her.

Contents

Abstract .... **ii**

Co-authorship statement .... **iv**

Acknowledgments .... **v**

Dedication .... **vii**

List of tables .... **xii**

List of figures .... **xiii**

List of appendices .... **xviii**

Nomenclature .... **xix**

Chapter 1 .... **1**

1 Introduction 1

1.1 General introduction 1

1.2 Literature review 4

1.2.1 Wind loading on PV panels 4

1.2.1.1 Background 4

1.2.1.2 Previous studies 6

1.2.2 Heat transfer from PV panels 16

1.2.2.1 Background 16

1.2.2.2 Previous studies 18

1.3 Motivation and objectives 23

1.4 Organization of the thesis 25

References 27

Chapter 2 33

2 Numerical simulation of wind effects on a stand-alone ground mounted Photovoltaic (PV) system..33

2.1 Introduction 33

2.2 Numerical model 37

2.3 Results and discussion 44

2.3.1 Surface pressures 44

2.3.2 Aerodynamic loading..47

2.3.3 Wind flow field 50

2.4 Conclusions 55

References 57

Chapter 3 62

3 Experimental analysis of wind flow around a ground mounted stand-alone solar panel 62

3.1 Introduction 62

3.2 Experimental details 64

3.2.1 Wind tunnel and the solar panel model...64

3.2.2 Instrumentation and measurements..66

3.2.2.1 Particle Image Velocimetry 66

3.2.2.2 Hot Wire Anemometry 70

3.2.3 Boundary layer simulation..72

3.3 Results and discussion 74

3.3.1 Mean velocity field 74

3.3.2 Reynolds normal and shear stresses 81

3.3.3 Vortex shedding characteristics 83

3.4 Conclusions 85

References 87

Chapter 4 92

4 Effect of wind on an array of ground mounted solar panels 92

4.1 Introduction 92

4.2 Methodology 95

4.2.1 Solar panel model details 95

4.2.2 Computational grid 96

4.2.3 Numerical model details 98

4.3 Numerical model validation 101

4.4 Results and discussion 106

4.4.1 Wind flow field characteristics 106

4.4.2 Surface pressure distribution 108

4.4.3 Aerodynamic loading 113

4.5 Concluding remarks 115

References 117

Chapter 5 122

5 CFD analysis of convective heat transfer from ground mounted solar panels 122

5.1 Introduction 122

5.2 CFD model 125
5.2.1 Solar panel geometry 125
5.2.2 Computational domain and mesh...126
5.2.3 Boundary conditions 129
5.2.4 Solver, turbulence model and numerical schemes 130
5.3 Validation of the CFD model 132
5.4 Results and discussion 135
5.4.1 Convective heat transfer coefficient (CHTC) 135
5.4.2 Correlation between flow field and heat transfer.......................................138
5.4.3 Comparison with existing correlations 142
5.4.4 Example case 144
5.5 Conclusions 146
References 148
Chapter 6 152
6 Conclusions and recommendations 152
6.1 Conclusions 152
6.2 Contributions 155
6.3 Recommendations for future study 156
References 158
Appendices...159
References 177
Curriculum Vitae 178

List of Tables

1.1 Studies on wind loading of solar panels and their specifications 14

1.2 Convective heat transfer studies on inclined surfaces 22

2.1 SST k-ω turbulence model constants employed in the present study..........................42

3.1 Location of the center of vortices and thickness of vortices 78

C.1 SST k- ω turbulence model constants 165

E.1 Precision uncertainty of the measurement of mean streamwise velocity at the empty wind tunnel (here, Y is the height from the wind tunnel floor and H is the panel height) 171

E.2 Precision uncertainty of the mean streamwise velocity in the wake of the solar panel at different heights (here, Y is the height from the wind tunnel floor and H is the panel height) 172

List of Figures

1.1 Total solar PV global capacity (Ren 21, 2014)..2

1.2 Electrical efficiency of typical silicon based PV cell with operating temperature (Skoplaki and Palyvos, 2009) 3

1.3 Aerodynamic forces on an inclined flat plate 6

2.1 Computational model of the stand-alone PV system (a) front view (b) side view 38

2.2 Wind direction α^o 38

2.3 Computational domain..39

2.4 (a) 3D isometric and (b) 2D sectional view of the computational grid 39

2.5 Inlet and incident velocity and turbulence intensity profiles 42

2.6 Mean C_p contours on the panel surfaces 45

2.7 Mean C_p profiles along the mid-line of the panel surface for wind directions of (a) 0^o and (b) 180^o. Here, b is the distance from the leading edge along the breadth of the panel 46

2.8 Time history of drag (CD) and lift coefficient (CL) averaged over the entire PV panel 48

2.9 Mean drag, lift, net pressure and moment coefficients for different wind directions and the direction of positive momentum 48

2.10 Comparison of mean drag and lift coefficients with ASCE 7-10 building code 49

2.11 Streamlines on the plane parallel to the side edges of the panel through the middle support leg with the mean C_p profiles for the wind directions of (a) 0^o (b) 45^o (c) 135^o and (d) 180^o 51

2.12 Corner vortices on the leeward side of the panel for (a) 45^o and (b) 135^o wind directions 52

2.13 Contours of spanwise vorticity (ω_z) on the plane parallel to the side edges of the panel through the middle support leg for different wind directions (a) 0^o, (b) 45^o, (c) 135^o and (d) 180^o 53

2.14 Isosurface of spanwise vorticity at the final time step (20 s) for all four wind directions..54

3.1 Experimental model of the solar panel 65

3.2 Wind direction (α^o) 67

3.3 Schematic of the experimental setup (not to scale) 67

3.4 Schematics of the measurement planes in a plan-view (not to scale) for (a) 0^o and 180^o and (b) 45^o and 135^o wind directions 68

3.5 Location of measurement frames on a plane (for 0^o wind direction). Dashed line (black) represents when the laser was upstream and dash-dotted (grey) when the laser was downstream of the solar panel 69

3.6 Image processing steps (a) raw image (b) masking image and (c) corrected vectors (only every 5th vectors are shown here)..70

3.7 (a) Mean velocity and (b) Turbulence Intensity (TI) profiles in the wind tunnel 73

3.8 Spectra of the (a) streamwise and (b) vertical velocity fluctuations at the solar panel height, H 74

3.9 Normalized mean velocity contours with superimposed streamlines for (a) α = 0^o, Plane 1, (b) α = 0^o, Plane 2, (c) α = 180^o, Plane 1, (d) α = 180^o, Plane 2, (e) α = 45^o, Plane 3, windward, (f) α = 45^o, Plane 3, leeward, (g) α = 135^o, Plane 3, leeward, (h) α = 135^o, Plane 3, windward....................77

3.10 Normalized velocity profiles for (a) α = 0^o, streamwise, (b) α = 0^o, vertical, (c) α = 180^o, streamwise, (d) α = 180^o, vertical, (e) α = 45^o, streamwise and vertical, (f) α = 135^o, streamwise and vertical velocity components....................79

3.11 Reynolds normal and shear stress components for (a) α = 0^o, (b) α = 180^o, (c) α = 45^o and (d) α = 135^o 83

3.12 Spectra of the vertical velocity fluctuation at Y/H = 1.14....................84

3.13 Streamwise velocity gradient at X/H = 3.8 at Plane 1....................84

4.1 Computational model of a single array with wind direction (α^o) shown in the XZ plane 96

4.2 Computational domain and mesh for 0^o wind direction (a) sectional view (b) isometric view....................98

4.3 Boundary conditions 99

4.4 Inlet and incident velocity and turbulence intensity profiles....................101

4.5 Comparison of the normalized mean streamwise ($\overline{U}$) and vertical ($\overline{V}$) velocity profiles on the surfaces of the solar panel between CFD and PIV for (a) α = 0^o, $\overline{U}$, (b) α = 0^o, $\overline{V}$, (c) α = 45^o, $\overline{U}$, (d) α = 45^o, $\overline{V}$, (e) α = 135^o, $\overline{U}$, (f) α = 135^o, $\overline{V}$, (g) α = 180^o, $\overline{U}$ and (h) α = 180^o, $\overline{V}$....................105

4.6 Normalized mean velocity magnitude contours with streamlines at the plane through the center of the panel and parallel to the side edge of the panel for (a) 0^o, (b) 45^o, (c) 135^o and (d) 180^o wind directions..108

4.7 Mean C_p distributions on the upper and lower surfaces of the solar panels for (a) 0^o, (b) 45^o, (c) 135^o and (d) 180^o wind directions 112

4.8 Comparison of the net mean C_p between the present study and Kopp et al. (2012)..112

4.9 Mean drag (C_D) and lift coefficients (C_L)...114

4.10 Mean overturning moment coefficients about Z axis (C_{Mz}) 115

5.1 Thermal energy balance of a stand-alone ground mounted solar panel 123

5.2 Computational model of the stand-alone PV system with wind direction (α^o) convention 126

5.3 Computational grid for 0^o wind direction. (a) Isometric view (b) X-Y plane view with a close-up view of the mesh at the lower edge of the panel 128

5.4 Inlet and incident velocity and turbulence intensity profiles. Here, heights (Y) are normalized with the height of the solar panel (H) and wind speeds ($\overline{U}$) are normalized with the velocity at H ($\overline{U_H}$) 130

5.5 Comparison of the normalized mean streamwise ($\overline{U}$) and vertical ($\overline{V}$) velocity components on the surfaces of the solar panel between CFD and PIV for 0^o and 180^o wind directions. Here, four figures are for (a) 0^o-$\overline{U}$, (b) 0^o-$\overline{V}$, (c) 180^o-$\overline{U}$ and (d) 180^o-$\overline{V}$. Here, distances are normalized with the panel height (H) and velocities are normalized by the velocity at H in the undisturbed flow ($\overline{U_H}$) 134

5.6 CHTC contours on the upper and lower surfaces of the solar panel for (a) Re 1.0×10^5-0^o wind, (b) Re 5.5×10^5 -0^o wind, (c) 1.1×10^6-0^o wind, (d) 1.0×10^5-180^o wind, (e)

5.5×10^5-180^o wind and (f) 1.1×10^6-180^o wind. For each image pair, upper contour is for the upper surface and the lower contour is the lower surface of the panel......................136

5.7 Mean CHTC profile at the line on the surfaces of the solar panel along the breadth of the panel between two support legs for (a) 0^o and (b) 180^o wind directions. Here, b is the local distance from the leading edge along the breadth (B) of the solar panel................139

5.8 Streamlines at the plane between two support legs for (a) Re $1.0\text{x}10^5$-0^o wind, (b) Re $1.0\text{x}10^5$-180^o wind, (c) $5.5\text{x}10^5$-0^o wind, (d) $5.5\text{x}10^5$-180^o wind, (e) $1.1\text{x}10^6$-0^o wind and (f) $1.1\text{x}10^6$-180^o wind 140

5.9 Correlation between Nusselt number (Nu) and Reynolds number (Re)....................142

5.10 Comparison of the Nusselt number values obtained from the present study with previous studies...144

5.11 Temperature (^{o}C) contours on the surfaces of the panel for (a) Re 1.0×10^5-0^o wind, (b) Re 5.5×10^5 -0^o wind, (c) Re 1.1×10^6-0^o wind, (d) Re 1.0×10^5-180^o wind, (e) Re 5.5×10^5-180^o wind and (f) Re 1.1×10^6-180^o wind. For each image pair, upper contour is for the upper surface and the lower contour is the lower surface of the panel 146

B.1 Mean C_p profiles along the mid-line of the panel surface. Here, b is the distance from the leading edge along the breadth of the solar panel 162

B.2 Normalized mean (a) streamwise ($\overline{U}$) and (b) vertical ($\overline{V}$) velocity profiles on the solar panel. Here, $\overline{U_H}$ is the mean streamwise velocity at height H 163

List of Appendices

Appendix A: Governing equations 159

Appendix B: Comparison between SST k-ω and Realizable k-ε turbulence models 161

Appendix C: Modification of turbulence model constants 165

Appendix D: PIV error calculation 167

Appendix E: HWA error calculation 170

Appendix F: Copyright agreement..175

NOMENCLATURE

Abbreviations

ASCE	American Society of Civil Engineers
ABL	Atmospheric Boundary Layer
a-Si	Amorphous Silicon
BIPV/T	Building Integrated Photovoltaic/Thermal
BLWT	Boundary Layer Wind Tunnel
CFD	Computational Fluid Dynamics
CHTC	Convective Heat Transfer Coefficient
COST	European Cooperation in Science and Technology
CTA	Constant Temperature Anemometer
DES	Detached Eddy Simulation
DNS	Direct Numerical Simulation
ESDU	Engineering Sciences Data Unit
FFT	Fast Fourier Transform
HWA	Hot Wire Anemometry
LES	Large Eddy Simulation
m-Si	Monocrystalline Silicon
PIV	Particle Image Velocimetry
PISO	Pressure Implicit with Splitting of Operators
PV	Photovoltaic
PVC	Polyvinyl Chloride

p-Si	Polycrystalline Silicon
RANS	Reynolds-Averaged Navier-Stokes
RSM	Reynolds Stress Model
SEAOC	Structural Engineers Association of California
SHARCNET	Shared Hierarchical Academic Research Computing Network
SST	Shear Stress Transport
TI	Turbulence Intensity

Latin symbols

a_1, c_1	SST k-ω turbulence model constants (-)
A	Surface area of a single row of panels in the array configuration (m^2)
A_{ref}	Surface area of the panel in the stand-alone configuration (m^2)
A_0	Reference area for calculating C_F for an inclined plate (m^2)
B	Breadth of the panel (m)
B′	Breadth of the panel in a measurement plane (m)
b	Distance from the leading edge of the panel on the panel surface along the breadth of the panel (m)
C_s	Roughness constant (-)
C_P	Coefficient of pressure (-)
c_p	Specific heat of air (J/kg-K)
C_F	Coefficient of aerodynamic force (-)
CD, C_D	Coefficient of drag (-)
CL, C_L	Coefficient of lift (-)
CM	Coefficient of moment (-)

CMx	Coefficient of moment about X axis (-)
CMz, C_{Mz}	Coefficient of moment about Z axis (-)
CN, C_N	Coefficient of net area weighted average pressure from both upper and lower surfaces of the panel (-)
Cr	Courant number (-)
C_μ	Turbulence model constant (= β^* for SST k-ω) (-)
d	Normal distance from the panel surface (m)
E	Integration constant (≈ 9.793) (-)
e	Emissivity (-)
f	Frequency (Hz)
F	Aerodynamic force (N)
F_1	Blending function in the SST k-ω turbulence model (-)
F_D	Drag force (N)
F_L	Lift force (N)
g	Gravitational acceleration (m/s^2)
G	Incoming solar flux (W/m^2)
G_f	Gust factor (-)
Gr	Grashof number (-)
Gr_L	Grashof number based on L_P (-)
H	Height of the panel (m)
h	Vertical projection of the inclined surface of the panel (m)
h_C	Convective heat transfer coefficient (W/m^2-K)
k	Turbulent kinetic energy (m^2/s^2)

k_{eff}	Effective thermal conductivity (W/m-K)
k_m	Molecular thermal conductivity (W/m-K)
k_P	Turbulent kinetic energy at the first cell center from the wall (m^2/s^2)
k_s	Roughness height (m)
L	Length scale in momentum calculation (m)
L_P	Length of the inclined plate (m)
M	Net moment from the upper and lower surfaces of the panel (N-m)
M_Z	Net moment from the upper and lower surfaces of the panel about Z axis (N-m)
Nu	Nusselt number (-)
P	Local pressure (Pa)
p	Design pressure (Pa)
P_k	Production of turbulent kinetic energy (Kg/ms^3)
$\overline{P}$	Mean pressure (Pa)
P_0	Reference pressure to calculate C_p for an inclined plate (Pa)
P_{ref}	Reference pressure used to calculate C_p for the stand-alone configuration (Pa)
Pr	Prandtl number (-)
q	Dynamic pressure (Pa)
Q_c	Convected heat flux from the PV panel (W/m^2)
Re	Reynolds number (-)
Re_L	Reynolds number based on L_P (-)
Re_{EH}	Reynolds number based on eaves height of a building (-)

Ri	Richardson number (-)
St	Strouhal number (= $fh/\overline{U_H}$) (-)
St_n	Stanton number (-)
$S_{u'}$	Spectra of streamwise velocity fluctuation ($m^2/s^2/Hz$)
$S_{v'}$	Spectra of vertical velocity fluctuation ($m^2/s^2/Hz$)
T_{PV}	Temperature of the PV panel (K)
T	Temperature of a computational cell (K)
$\overline{T}$	Mean temperature (K)
T_0	Reference temperature for Boussinesq approximation (K)
T_{amb}	Ambient temperature (K)
T_{ref}	Bulk temperature of air for calculating h_C (K)
t	Flow time (s)
t^*	Non-dimensional flow time (= $t\overline{U_H}/B$) (-)
U_0	Reference velocity to calculate C_p for an inclined plate (m/s)
U_∞	Free stream velocity (m/s)
$\overline{U}$, U	Mean streamwise velocity component (m/s)
$\overline{U_H}$	Mean streamwise velocity at height H (m/s)
U_R	Velocity at the top of the domain (m/s)
U_{ref}	Reference velocity (m/s)
U_{1mT}	Wind speed at 1 m above the top edge of the panel (m/s)
U_{10m}	Wind speed at 10 m height from the ground (m/s)
u^*	Friction velocity (m/s)
$\overline{u'u'}, \overline{v'v'}$	Reynolds normal stress components (m^2/s^2)

$\overline{u'v'}$	Reynolds shear stress component (m^2/s^2)
du/dy	Streamwise velocity gradient (/s)
$\overline{V}$	Mean vertical velocity component (m/s)
V	Wind velocity in the heat transfer correlation in the previous studies (m/s)
v	Local mean velocity in a cell (m/s)
W	Width of the panel (m)
y_0	Aerodynamics roughness length (m)
$y_{L.E.}$	Lower edge height of the panel from the bottom surface of the domain (m)
y_P	First cell center distance from the bottom surface of the domain (m)
y_R	Domain height (m)
y^*	Dimensionless wall distance (= $C_\mu^{1/4}k_P^{1/2}y_P/\nu$) (-)
y^+	Dimensionless wall distance (= u^*y_p/ν) (-)

Greek symbols

α	Wind direction (^{o})
α_S	Solar absorption coefficient (-)
β	Thermal expansion coefficient (1/K)
Δt	Time step (s)
Δt^*	Non-dimensional time step (= $\Delta t\overline{U_H}/B$) (-)
Δl	Grid cell size (m)
ΣC_p	Net mean C_p from the upper and lower surface of the panel (-)
ε	Dissipation rate of turbulence (m^2/s^3)
ε_{ps}	Particle size error (-)
ε_{dr}	Dynamic range error (-)

ε_{sd}	Seeding density error (-)
ε_g	Gradient error (-)
ε_{AGW}	Interpolation error (-)
ρ	Density of air (kg/m^3)
ρ_k	Effective kinematic density (-)
ρ_0	Effective kinematic density at T_0 (-)
θ	Panel inclination angle (^{o})
σ	Stefan-Boltzmann constant (= 5.67×10^{-8} W/m^2-K^4)
σ_U	Standard deviation of streamwise velocity component (m/s)
σ_V	Standard deviation of vertical velocity component (m/s)
μ	Dynamic viscosity (Pa.s)
μ_t	Turbulent eddy viscosity (Pa.s)
ν	Kinematic viscosity (m^2/s)
η_T	PV panel efficiency at temperature T (-)
η_{Tref}	PV panel efficiency at reference temperature T_{ref} (-)
ω	Specific dissipation rate of turbulence (s^{-1})
ω_z	Spanwise vorticity (s^{-1})
σ_k, σ_ω, α_n, α_{k1}, α_{k2}, $\alpha_{\omega1}$, $\alpha_{\omega2}$, β_n, β_1, β_2, β^*, γ_1, γ_2	SST k-ω turbulence model constants (-)

Chapter 1

Introduction

1.1 General introduction

Solar energy is available everywhere abundantly. The amount of incoming solar energy in earth’s atmosphere in one hour ($4.3x10^{20}$J) is almost equal to the energy consumed by the entire world in one year. In other words, if we tap only 1% of the incident solar energy on the earth’s surface at an efficiency of 1%, our present world energy consumption can be met (Abbott, 2010). Solar energy is usually harnessed in two ways; electrical energy using Photovoltaic (PV) systems and thermal energy using solar collector systems. Solar PV panels have become the fastest growing in terms of installed capacity among all the renewable energy sources. Almost 30% of the total installed PV capacity came into operation in 2013 alone (Ren 21, 2014) (Fig. 1.1). Utility scale PV power station or solar farms are rapidly growing in numbers and also in capacity. As of 2014, at least 53 solar farms with capacity more than 50MW are operating in 13 countries (REN 21, 2014), whereas before 2009, only one solar farm had installed capacity of more than 50MW (Olmedilla PV Park, Spain, 60MW). Solar farms usually employ large number of ground mounted PV panels arranged in arrays in a vast open field. Optimum designing of solar panel support structures to withstand aerodynamic forces has been a challenge for solar panel manufacturers and installers. Keeping this challenge in mind, an in-depth literature review on wind loads on ground mounted solar panels is presented in the next section (Section 1.2).

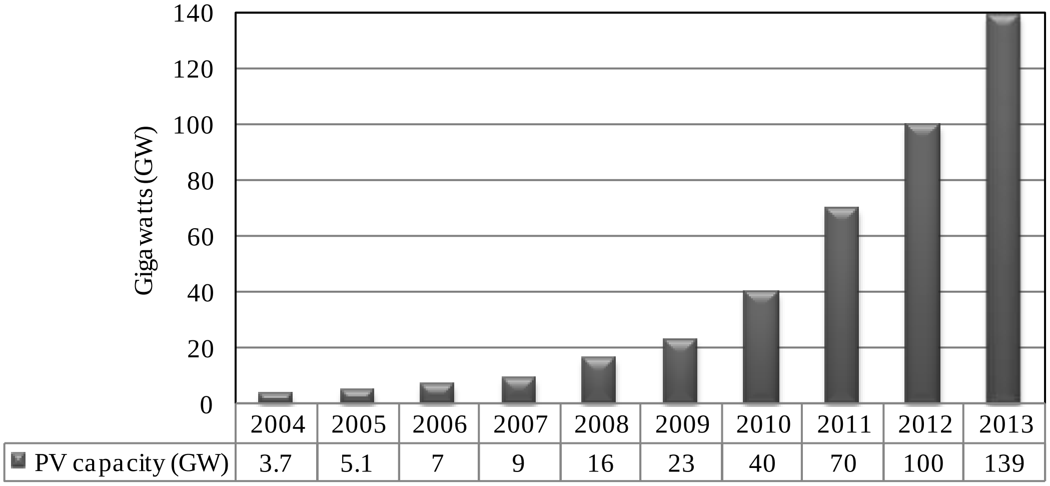

Figure 1.1: Total solar PV global capacity (Ren 21, 2014).

Another important aspect regarding the performance of the solar PV panels is the panel temperature as the electrical efficiency of the PV panel is greatly dependent on it. According to Skoplaki and Palyvos (2009), electrical efficiency of the commercial grade silicon cell PV modules decreases linearly with the operating temperature (Fig. 1.2). Therefore, an accurate prediction of the PV panel temperature is necessary to estimate the potential electrical power output from a PV module. The temperature of a PV panel can be estimated before actually installing the PV system at a known site by properly conducting the thermal energy balance calculation for the PV system. Convective heat loss due to the wind flowing over the PV panel is one of the major contributing factors to the thermal energy balance of the PV system (Karava et al., 2011) and thus an accurate measure of the wind induced convective heat loss is necessary for the optimal performance of the PV system. Previous studies have dealt with convective heat transfer from flat surfaces of different structures. The usefulness of these studies in finding wind induced convective heat loss from ground mounted solar panels, as well as their limitations, are discussed in Section 1.2.

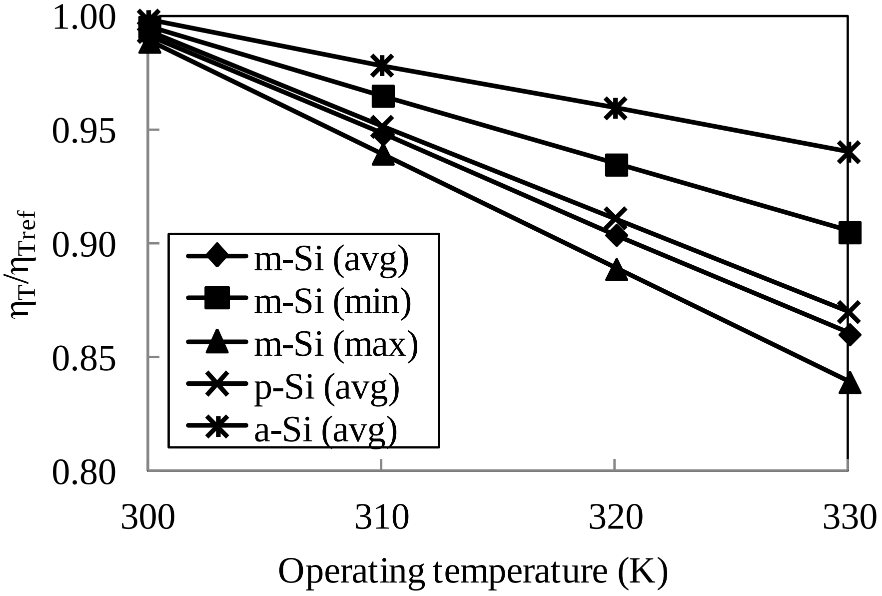

Figure 1.2: Electrical efficiency of typical silicon based PV cell with operating temperature (Skoplaki and Palyvos, 2009).

1.2 Literature review

1.2.1 Wind loading on PV panels

1.2.1.1 Background

The surface pressure on a body is usually expressed in terms of a dimensionless parameter, coefficient of pressure (C_P) and is defined as

$$C_P = \frac{P - P_0}{\frac{1}{2}\rho U_0^2} \tag{1.1}$$

where, P is the static pressure on the surface (Pa), P_0 is the pressure at a reference point without the influence of the body (Pa), ρ is the density of the fluid (kg/m^3) and U_0 is the fluid velocity at reference point (m/s). Similarly, force coefficient (C_F) is used to represent aerodynamic forces acting on a body and is defined as

$$C_F = \frac{F}{\frac{1}{2}\rho U_0^2 \, A_0} \tag{1.2}$$

where, F is the aerodynamic force (N) and A_0 is the reference area (m^2) (not necessarily the area over which the force acts). Often, A_0 is the projected frontal area. Aerodynamic forces are usually resolved into two orthogonal directions, either parallel and perpendicular to wind direction or parallel and perpendicular to a direction related to the geometry of the body. Parallel and perpendicular components of the aerodynamic forces, with respect to the incoming wind direction, are termed as drag (F_D) and lift (F_L) forces.

The coefficients of drag (C_D) and lift (C_L) can be calculated using Equation (1.2) by replacing F with F_D and F_L respectively.

Aerodynamic forces on an inclined flat plate are shown in Figure 1.3. The relation of C_D and C_L with C_P, based on Figure 1.3, are given by the following equations.

$$C_D = \frac{\sum_{i=1}^{n} C_{P_i} A_i \sin\theta}{A_0} \tag{1.3}$$

$$C_L = \frac{\sum_{i=1}^{n} C_{P_i} A_i \cos\theta}{A_0} \tag{1.4}$$

where, C_{P_i} is the pressure coefficient at a specific location on the plate, A_i is the tributary area associated with C_{P_i} (m^2) and θ is the inclination angle (^{o}).

Torque or momentum coefficient is used to express the torsional component of wind loading. Definition of torque coefficient (C_M) is given in Equation (1.5),

$$C_M = \frac{M}{\frac{1}{2} \rho U_0^2 \, A_0 L_P} \tag{1.5}$$

where, M is the moment about the center axis of the plate (N-m) (Fig. 1.3) and L_P is the length of the inclined plate (m).

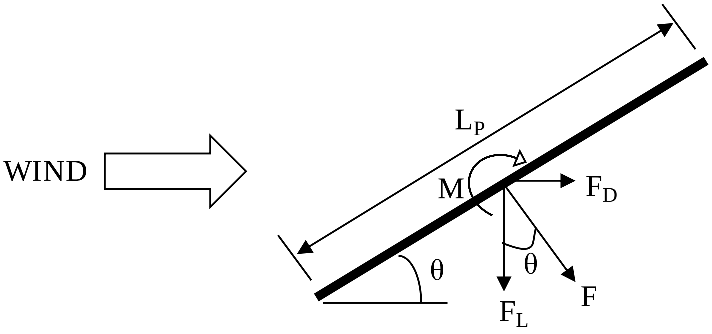

Figure 1.3: Aerodynamic forces on an inclined flat plate.

1.2.1.2 Previous studies

Based on the panel mounting location, published literatures on wind loading of solar panels can be categorized into two major classes, roof mounted and ground mounted. One of the earliest studies on roof mounted solar panels was by Radu et al. (1986) who conducted boundary layer wind tunnel experiments to investigate wind loads on arrays of solar collectors on the flat roof of a five storey building. It was observed that the lift force on the solar collectors is dominant for all wind directions as the flow separated at the leading edge of the roof and did not reattach. One of the principal findings of this study was that the sheltering effects of the first row of the collectors or the roof leading edge reduced the wind loads on solar collectors significantly. Radu and Axinte (1989) continued the study by Radu et al. (1986) to investigate the effect of building geometry on the wind loading of solar collectors. It was found that roof reduces by about 50% the velocity fluctuations on solar collectors and prevents the possible overturning of the solar collectors above the roof ridge.

Wind tunnel pressure tests on solar panel arrays mounted parallel to the flat roof of an industrial building (0^o inclination) were performed by Wood et al. (2001). The lateral spacing of the panel (4 to 8 mm at 1:100 scale) and height of the panel above the roof surface (6 to 14 mm at 1:100 scale) were found to have little effect on the pressures on the panel surface. However, the effect of the orientation of the panels with respect to wind direction and the proximity of the panel to the roof leading edge on the panel net pressure coefficients were more pronounced. Aerodynamically induced torque on six parallel concentrator type solar panels was studied by Kopp et al. (2002). The largest peak torque was found for two particular wind angles (270^o and 330^o) and a quasi-steady model was developed to predict the peak system torque considering the effects of vortex shedding and free stream turbulence intensity.

Chung et al. (2008) performed a wind tunnel experiment on a single flat plate solar water heater to reduce the possible damage due to strong wind lift. It was found that installing a guide plate normal to the flow reduces wind uplift effectively. The effect of a horizontal cylinder, placed above the top edge of the solar panel, on wind uplift for the same geometry as Chung et al. (2008) was investigated by Chung et al. (2011). It was reported that the presence of the cylinder decreases the differential mean pressure at the front edge of the panel causing a decrease in the mean uplift force. However, uniform oncoming flow, high blockage ratio (~ 8.75%) and low free stream turbulence intensity (0.3%) limited the applicability of both studies. Also, both experiments by Chung et al. (2008) and Chung et al. (2011) were performed on the wind tunnel floor, whereas these studies were aimed for roof mounted applications.

Kopp et al. (2012) studied the aerodynamic loads on roof mounted solar panel arrays using wind tunnel tests. A set of experiments with ground mounted arrays were also performed to investigate the effect of the building and it was found that presence of the building changed the loads substantially on the roof mounted system. Three critical wind directions were identified for the roof mounted system in terms of maximum uplift; northern (180^o), northern-cornering (120^o-150^o) and southern (0^o). Pratt and Kopp (2013) further investigated the aerodynamic mechanisms associated with peak loads using synchronized time resolved particle image velocimetry (PIV) and pressure measurements on the same roof mounted solar arrays. For 20^o solar panel tilt angle, large vertical gusts were responsible for the peak uplift for 180^o wind direction, whereas for 0^o wind direction, the peak uplifts were associated with the streamwise gusts.

Banks (2013) reported over 20 wind tunnel tests on the solar panel arrays on flat roofs of low rise buildings using variety of racking systems with tilt angles between 0^o and 25^o. One of the major findings of this study was that the corner vortices dictated the peak uplift loads on the roof mounted solar arrays. Cao et al. (2013) also investigated the uplift load on solar arrays mounted on a flat roof using wind tunnel measurements. While comparing the uplift loads between stand-alone and array cases, it was observed that the stand-alone system experienced higher loads than arrays of panels at the same location. Also, with the increase in tilt angle of solar panels or the distance between arrays, panel generated turbulence dominated the uplift loading. Effect of the parapet on the solar arrays (tilt angle 10^o) mounted on the flat roof of a building was studied by Browne et al. (2013). As in Banks (2013), Browne et al. (2013) also observed that the corner vortices were responsible for the peak wind loads. It was concluded that the parapet did not shelter the array rather parapets of heights 1 to 7 times the height of the array could increase the wind load by 1.7 times. Aly and Bitsuamlak (2014) performed wind tunnel tests on solar panels mounted on the gabled roof with two different slopes (3:12 and 5:12) to investigate wind loads on the panel under varying wind directions (0^o to 350^o with 10^o interval as well as 45^o, 135^o, 225^o, 315^o). Net pressure distribution on the solar panel was found to be substantially different than net external pressure distribution on the bare roof of the same building. Also close to the roof edge, corner and ridge, wind load was maximum and it was recommended to avoid those areas for mounting solar panels on gable roofs.

The study by Stathopoulos et al. (2014) examined the wind loads on a stand-alone solar panel placed on the ground, flat roof as well gable roof of a building. It was concluded that the wind directions in the range of 105^o to 180^o resulted in the extreme pressure coefficient values with 135^o being the critical one. For the various configurations studied by Stathopoulos et al. (2014), the effect of building height and the panel location were not significant for the roof mounted systems. For the ground mounted system, the maximum and minimum peak pressure coefficients were observed for 30^o and 135^o wind directions, respectively. Both maximum and minimum peak pressures occurred for 45^o inclination angle of the panel. Wind tunnel tests were performed by Warsido et al. (2014) to investigate the effect of row spacing on wind loads for a solar panel array mounted on the flat roof of a building and also on the ground. 1:30 geometric scale model with inclination of 25^o and wind directions ranging from 0^o to 180^o at 10^o interval were employed. For the roof mounted system, the corner region was critical in terms of wind loads for the oblique wind directions. Minimal influence of lateral spacing between panels was found on the inner panel columns of the ground mounted system. However, on the outer column, the wind loads were larger for the zero lateral spacing case. Also, increasing longitudinal spacing between panels increased wind loads on the panels. While comparing the wind loads between an isolated panel and the panels in an array, the isolated panel experienced higher loads than in an array configuration.

Published literatures solely on the ground mounted solar panel systems are discussed below. Aly and Bitsuamlak (2013) performed wind tunnel tests on a stand-alone ground mounted solar panels of five different geometric scales (1:50, 1:30, 1:20, 1:10 and 1:5) to investigate the effect of scales on wind loading of the panel with 25^o and 40^o tilt angles. Computational fluid dynamics (CFD) studies were also performed using 1:50, 1:20 and 1:10 geometric scales with 40^o tilt. It was observed that the mean surface pressures on the panel were not significantly affected by the different scale sizes. However, standard deviation and peak pressure coefficients varied with geometric scales. Also, except for 1:50 scale, similar 3-s peak force coefficient values were found for all scales. Abiola-Ogedengbe (2013) performed PIV measurements on a ground mounted solar panel and measured wind profiles only for 0^o incoming wind direction and also only at the windward side of the panel.

Shademan et al. (2014a) performed CFD simulations using 3D steady Reynolds-Averaged Navier-Stokes (RANS) approach to investigate wind loads on ground mounted solar panels in both stand-alone and array configuration with tilt angle of 45^o. Validation of the numerical model with an inclined flat plate study by Fage and Johansen (1927) showed that the shear stress transport (SST) k-ω (Menter, 1994) turbulence model performed better than the realizable k-ε (Shih et al., 1995) model. For the stand alone system, wind directions ranging from 0^{o} to 180^{o} and 30^{o} intervals were employed. Effects of the spacing between individual modules and ground clearance were studied for the stand-alone system for only 0^{o} wind direction. Similarly, the array configuration was tested for 0^{o} wind direction with three different spacing between two consecutive arrays. For the stand-alone system, the maximum wind loading was found for 0^{o} and 180^{o} wind directions. Increasing the spacing between individual modules increased the loading close to the gap. Increasing the ground clearance also resulted in higher wind loads. For the array configuration, the case with the smallest spacing in between two consecutive arrays produced the lowest wind loads on the panels. Shademan et al. (2014b) continued their investigation on wind loading on the ground mounted solar panel but this time using Detached Eddy Simulation (DES). It was reported that as the ground clearance increased, stronger vortex shedding (in the sense of vortices that are shed out of the shear layer) and larger unsteady forces were observed.

Similarities and variability among all studies discussed above are presented in Table 1.1.Table 1.1 shows that a significant number of studies have been performed on roof mounted PV systems. In contrast, studies on ground mounted solar panels are very limited. Also, due to the relative smaller structural size of solar panels, most of the studies are performed for a geometric scale of 1:50 or smaller (larger models). To simulate an atmospheric boundary layer profile at a scale of 1:50 or smaller (larger models) in the regular boundary layer wind tunnels, which are usually designed for 1:100 or larger (smaller models), is a challenging task and needs to be addressed. As for critical wind directions, in terms of maximum wind loads on the entire panel, quasi consensus can be reached for cornering (45^o, 135^o, 225^o, 315^o) and straight wind directions (0^o and 180^o). It is also observed that there is very little information available regarding wind flow field around the ground mounted solar panels, especially from experimental measurements. Experimental investigation of wind flow field around the ground mounted solar panel would be valuable in validating CFD results. Again, detail analysis of wind loads in relation to the wind flow field around the solar panels is also lacking in the literature and is necessary to completely understand the mechanism behind the wind loading on solar panels.

Existing building codes in North America (ASCE 7-10, 2010 and National Building Code of Canada, 2010) do not provide any information on minimum design wind loads for solar panel arrays, either ground mounted or roof mounted. However, in ASCE 7-10 (2010), wind tunnel tests (Method 3 in the building code) are suggested to obtain design wind loads for individual buildings. Kopp and Banks (2013) provided a detail discussion of using Method 3 to obtain design loads for roof mounted solar panel arrays. Again, in ASCE 7-10 (2010), the only structure, that resembles a stand-alone ground mounted solar panel, is the mono-slope free roof for which design loads for 0^o and 180^o wind directions are reported. However, to what extent the minimum design load for mono-slope free roofs are applicable to ground mounted stand-alone solar panels, needs to be investigated.

Building codes in Australia (AS/NZS 1170.2, 2011) and California (SEOAC, 2012) have some standards for roof mounted solar panels but not for ground mounted installations.

Table 1.1: Studies on wind loading of solar panels and their specifications.

Authors	Method	Geometric scale	Configuration	Mounting location	Tilt angle	Wind directions	Critical wind direction (Larger load)
Radu et al. (1986)	Wind tunnel test, Pressure	1:50	Array	Horizontal roof	30^o	0^o to 360^o at 15^o interval	225^o, 315^o
Radu and Axinte (1989)	Wind tunnel test, pressure	1:50	Array	Horizontal roof with attic	-	0^o, 30^o, 90^o, 180^o	-
Wood et al. (2001)	Wind tunnel test, pressure	1:100	Array	Horizontal roof	0^o	0^o and 90^o	-
Kopp et al. (2002)	Wind tunnel test, pressure	1:6	Array (concentrator panel)	Ground	10^o, 30^o, 45^o	225^o, 270^o and 330^o	Cornering winds and 270^o
Chung et al. (2008)	Wind tunnel test, pressure	1:1.7	Stand-alone (with cylinder at the top and guide plate)	Ground	25^o	180^o	-
Chung et al. (2011)	Wind tunnel test, pressure	1:1.7	Stand-alone (with cylinder at the top and guide plate)	Ground	15^o, 20^o, 25^o	180^o	-
Kopp et al. (2012)	Wind tunnel test, pressure	1:30	Array	Ground and horizontal roof	2^o, 20^o	0^o to 180^o and 10^o interval	130^o and 180^o (roof and ground), 0^o (roof)
Pratt and Kopp (2013)	Wind tunnel test, PIV, pressure	1:30	Array	Horizontal roof	2^o, 20^o	0^o and 180^o	-
Banks (2013)	Wind tunnel test, pressure	1:25 to 1:100	Array	Horizontal roof	0^o to 25^o	0^o to 180^o at 10^o interval	Cornering winds with corner vortices
Cao et al. (2013)	Wind tunnel test, pressure	1:50	Array	Horizontal roof	15^o, 30^o, 45^o	10^o interval (range not reported)	135^o and 225^o

Browne et al. (2013)	Wind tunnel test, pressure	1:25	Array	Horizontal roof	10^o	0^o to 360^o at 10^o interval	Cornering winds with corner vortices
Aly and Bitsuamlak (2014)	Wind tunnel test, pressure	1:15	Array	Flushed on gable roof	Roof tilt 14^o, 22.6^o	0^o to 35^o at 10^o interval, 45^o, 135^o, 225^o, 315^o	0^o, 10^o, 80^o, 120^o, 330^o
Stathopoulos et al. (2014)	Wind tunnel test, pressure	1:200	Stand-alone	Horizontal roof and ground	20^o, 30^o, 40^o, 45^o	0^o to 180^o at 15^o interval	135^o
Warsido et al. (2014)	Wind tunnel test, pressure	1:30	Array	Horizontal roof and ground	25^o	0^o to 180^o at 10^o interval	Varies with the location of a panel in an array
Aly and Bitsuamlak (2013)	Wind tunnel test, pressure, CFD, RANS, LES	1:50, 1:30, 1:20, 1:10, 1:5	Stand-alone	Ground	25^o, 40^o	0^o	-
Abiola-Ogedengbe (2013)	Wind tunnel test, pressure, PIV	1:10	Stand-alone	Ground	25^o, 40^o	0^o, 30^o, 150^o, 180^o	150^o, 180^o
Shademan et al. (2014a)	CFD, RANS	1:1	Stand-alone, array	Ground	45^o	0^o to 180^o at 30^o interval (stand-alone), 0^o (array)	0^o and 180^o
Shademan et al. (2014b)	CFD, DES	1:1	Stand-alone	Ground	45^o	0^o	-

1.2.2 Heat transfer from PV panels

1.2.2.1 Background

When fluid flows over a hot surface, it removes heat through convective heat transfer. If the fluid motion is induced by some external means (pump, blower, wind, vehicle motion, etc.), the process is generally called forced convection. Whereas, if the fluid motion arises due to buoyancy force field the process is usually called natural convection. The amount of heat taken away from the surface can be measured using Newton’s law of cooling, which relates the amount of heat convected away from a unit area to the temperature difference between the surface and the bulk fluid flowing over it and a parameter known as the convective heat transfer coefficient (CHTC) that characterizes the flow behaviour.

Newton’s law of cooling can also be applied in the case of flat plate PV systems. For a PV system, the exterior CHTC (h_C) of the system relates the heat flux from the PV panel (q_{PV}) to the difference between the surface temperature of the PV (T_{PV}) and a reference temperature (T_{ref}) which is generally the bulk temperature of the surrounding air:

$$h_C = \frac{q_{PV}}{T_{PV} - T_{ref}} \tag{1.6}$$

Wind induced CHTC for an external surface depends on the wind speed, wind direction, free stream turbulence intensity, integral length scale of turbulence, size of the surface and surface roughness as these factors influence the flow behavior, which in turn affect the amount of heat transfer and hence, the panel surface temperature (Palyvos, 2008;

Kondjoyan et al., 2002). Although analytical solutions for the CHTC exist for very few simplified geometries, for all other systems, it must be determined experimentally (Holman, 2002). The CHTC in non-dimensional form is expressed as Nusselt number (Nu), which quantifies the relative contribution of convection versus conduction. For forced convection, the Nusselt number is a function of Reynolds number (Re) and Prandtl number (Pr), whereas for natural convection, Nusselt number is a function of Rayleigh number (Ra). Several correlations are developed to estimate Nusselt number for different flow and system configurations. For uniform flow over a horizontal surface under forced convection, the Nusselt number is expressed as (Incropera et al., 2006):

$$\mathrm{Nu} = 0.664\ \mathrm{Re}_L^{0.5}\mathrm{Pr}^{1/3} \qquad \text{Laminar flow} \qquad (1.7)$$

$$\mathrm{Nu} = 0.037\ \mathrm{Re}_L^{0.8}\mathrm{Pr}^{1/3} \qquad \text{Turbulent flow} \qquad (1.8)$$

where

$$\text{Nusselt number, } \mathrm{Nu} = \frac{h_C L_P}{k_m} \qquad (1.9)$$

$$\text{Reynolds number, } \mathrm{Re}_L = \frac{\rho U_\infty L_P}{\mu} \qquad (1.10)$$

$$\text{Prandtl number, } \mathrm{Pr} = \frac{\mu c_p}{k_m} \qquad (1.11)$$

In the above equations, L_P is the length of the plate (m), k_m is the molecular thermal conductivity of air (W/m-K), ρ is the density of air (kg/m^3), U_∞ is the free stream velocity (m/s), μ is the dynamic viscosity of air (Pa.s) and c_p is the specific heat of air at constant pressure (J/kg-K). The underlying assumptions of Equations (1.7) and (1.8) are constant temperature at the plate surface, no incident turbulence, and fluid properties are constant throughout the flow. Also, additional conditions such as, for Equation (1.7), $0.6 \leq \mathrm{Pr} \leq 50$ and for Equation (1.8), $\mathrm{Pr} \approx 1$ have to be met.

The relative contribution of forced and natural convection in a given case is quantified in terms of the $\mathrm{Gr_L}/\mathrm{Re_L^2}$ ratio (Incropera et al., 2006). Here, $\mathrm{Gr_L}$ is the Grashof number (Eq. 1.12) and is a measure of the ratio of the buoyancy forces to the viscous forces in a fluid.

$$\text{Grashof number}, \mathrm{Gr_L} = \frac{\mathrm{g}\beta(\mathrm{T_{PV}} - \mathrm{T_{ref}})\mathrm{L_P}^3}{\nu^2} \qquad (1.12)$$

where, g is the gravitational acceleration (m/s^2), β is the thermal expansion coefficient (1/K) and ν is the kinematic viscosity (m^2/s). The ratio $\mathrm{Gr_L}/\mathrm{Re_L^2}$ is often known as Richardson number for thermal convection. When Richardson number ≈ 1, both forced and natural convection modes have almost equal contributions. If $\mathrm{Gr_L}/\mathrm{Re_L^2} \ll 1$, forced convection is dominant, while for $\mathrm{Gr_L}/\mathrm{Re_L^2} \gg 1$, natural convection is dominant (Incropera et al., 2006).

1.2.2.2 Previous studies

Both experimental and numerical studies have been conducted by several researchers to estimate convective heat transfer coefficient from PV panels or solar collectors mounted on the roofs of low rise buildings. Kind et al. (1983) conducted a wind tunnel study on an array of solar collectors mounted on the 60$^\mathrm{o}$ inclined roof of a 1:32 scale model house.

The flow in the boundary layer developed on the model collector surfaces was found to be laminar when examined by a cathode ray oscilloscope. No specific correlation was given and the results were shown graphically in the form of the Stanton number $\left(\mathrm{St_n} = \frac{\mathrm{h_C}}{\mathrm{c_p \rho U_\infty}} = \frac{\mathrm{Nu}}{\mathrm{Re_L.Pr}}\right)$ against Reynolds number (Re). Kind and Kitaljevich (1985) studied inclined flat plate solar collectors mounted on the horizontal roof of a building and observed that the separation of flow and vortices from the leading edge of the roof had an important impact on the heat transfer from the surface of the solar collector.

Shakerin (1987) also performed a wind tunnel study on a single solar collector flush mounted on the roof of a model house with different tilt angles. Two different correlations were given for inclination angles, either greater or less than 40^o, since a separation bubble was observed for the inclination angles less than 40^o. The estimation of CHTC for a large heated flat plate with an exposed heat transfer surface area of 1.81 m × 0.89 m attached to a 35^o pitched roof of a single storey building were performed by Sharples and Charlesworth (1998). The wind-induced CHTC was correlated against the wind speed and the wind direction was measured 1.5 m above the ridge line of the roof. Since the given correlation was in terms of local velocity, rather than as a non-dimensional parameter, it is difficult to use the correlation for other plates and building geometries. The authors also concluded that the results would strictly apply to the particular experimental conditions.

High resolution 3-D steady RANS simulations were performed by Karava et al. (2011) to evaluate convective heat transfer from the windward roof of a low-rise building with application to the Building Integrated Photovoltaic/Thermal (BIPV/T) systems. Correlations between Nu and Re were developed for 30^{o} roof slope and for different terrain roughness.

The aerodynamic flow behavior around buildings is different from that around a ground mounted stand-alone PV system and hence, can significantly alter the heat transfer rate. Ground mounted stand-alone PV system can be related to an isolated inclined plate and therefore heat transfer studies on the inclined flat plate are relevant to this configuration. Experiments have been carried out to investigate heat transfer from the upper surface of an inclined flat plate/rectangular body by several researchers (Sparrow and Tien, 1977; Test and Lessman, 1980; Test et al., 1981; Kind and Kitaljevich, 1985).

A wind tunnel study was carried out to investigate the CHTC on a plate inclined and yawed at different angles by Sparrow and Tien (1977). Four different inclination angles (25^{o}, 45^{o}, 65^{o} and 90^{o}) were studied with three different yaw angles (0^{o}, 22.5^{o} and 45^{o}). The results showed that the heat transfer was relatively insensitive to the inclination angles (CHTC values varies within 5%) and yaw angles (within 4%) for the range studied. The turbulence level used in the test section was 0.2%, which was very low compared to the natural environment, resulting in low CHTC values when compared with other studies. Another wind tunnel study was performed by Test and Lessman (1980) to predict the CHTC on the upper surface of a rectangular model, with an aspect ratio of 6, at different angles of attack (0^{o} to 50^{o}). Flow separation was observed for the inclination angles lower than 20^{o} while, no separation was observed for the inclination angles higher than 30^o and flow remained laminar. The free stream turbulence was, again, comparatively low (2.5%).

To overcome the limitations of the wind tunnel studies discussed above, a full scale experiment was performed to investigate heat transfer behavior on the upper surface of a rectangular body by Test et al. (1981). The inclination angle was 40^o, for which no separation was observed. Special side attachments to the plate were also built to make the flow two dimensional so that the results can be compared with the wind tunnel test results and thus not taking into consideration complex 3D effects. A correlation was given for the CHTC which was strictly valid for a 40^o inclination angle.

A list of heat transfer studies presented here is summarized in Table 1.2. A detailed analysis and an extensive list on the convective heat transfer coefficients for different types of structures can be found in Palyvos (2008) and Defraeye et al. (2011). Most of the studies on heat transfer for inclined plates were subjected to uniform incoming flow and very low free stream turbulence compared to the atmospheric boundary flow and hence, cannot be applied to evaluate convective heat transfer for ground mounted stand-alone solar panels.

Table 1.2: Convective heat transfer studies on inclined surfaces.

Authors	Geometry	Method	Location of the velocity (V) measurement	Relationship
Sparrow and Tien (1977)	Inclined plate	Wind tunnel test	Free stream	$St_n Pr^{2/3} = 0.931 Re^{-1/2}$
Test and Lessman (1980)	Inclined rectangular body	Wind tunnel test	Free stream	-
Test et al. (1981)	Inclined rectangular body	Full scale experiment	1 m above the plate	$h = 2.56V + 8.55$
Kind et al. (1983)	Plate mounted on an inclined roof	Wind tunnel test	14 cm above the tunnel floor	St_n= fn[Re] presented graphically
Kind and Kitaljevich (1985)	Inclined plate mounted on horizontal roof	Wind tunnel test	Height of the middle of the plate above the tunnel floor	St_n= fn[Re] presented graphically
Shakerin (1987)	Plate mounted on an inclined roof	Wind tunnel test	Average near model	$St_n Pr^{2/3} = 1.23Re^{-1/2}$ $\theta < 40$ deg $St_n Pr^{2/3} = 0.90Re^{-1/2}$ $\theta \geq 40$ deg
Sharples and Charlesworth (1998)	Plate mounted on an inclined roof	Full scale experiment	1.5 m above the ridge	$h = 2.2V + 11.9$ $(0.5<V<6.7)$ or $h = 9.1V^{0.57}$
Karava et al. (2011)	Inclined roof	CFD	Roof eave’s height	$Nu = 0.093Re^{0.77}Pr^{1/3}$ (open terrain)

1.3 Motivation and objectives

Despite the rapid growth of photovoltaic (PV) power stations over the last decade, there are not yet sufficient studies to investigate the effect of wind on the loading of the ground mounted solar PV panel. As a result, national building codes around the world, lack the provision for minimum design loads for ground mounted solar PV panels either in stand-alone or array configuration. It is also of paramount importance to study the aerodynamic flow mechanisms around the solar panel in detail since these flow features are generating the wind loads. Another effect of wind on the solar panel is the heat transfer from the panel surface. As pointed out by Skoplaki and Palyvos (2009), wind induced heat transfer can significantly affect the electrical efficiency of PV panels. Hence, correlations between heat transfer and wind flow around ground mounted solar panels need to be developed.

Therefore the specific objectives of this study are:

- To estimate wind loads on ground mounted solar panels in both stand-alone and array configuration.
- To develop the relation between convective heat transfer from the surfaces of ground mounted solar panels and wind speed.
- To analyze the wind flow structures around the solar panel in relation to both wind loads and heat transfer.

- To establish numerical modelling approaches for simulating wind effects (loading and heat transfer) on ground mounted solar panels in atmospheric boundary layer flows.

This research is pertained to better understand the effect of wind on aerodynamic loads and heat transfer for ground mounted solar panels. The accomplishment of the aforementioned goals of this research would facilitate the advancement in better planning and designing of ground mounted solar panel based utility scale PV power stations. In this regard, the research conducted in this thesis aims to:

- Determine the mean aerodynamic wind loads on ground mounted solar panels in both stand-alone and array configuration under varying wind directions using unsteady 3D Reynolds-Averaged Navier-Stokes (RANS) simulations.
- Experimentally determine the wind flow around a stand-alone ground mounted solar panel using wind tunnel tests with Particle Image Velocimetry (PIV). Also explore the wake behavior employing Hot Wire Anemometry (HWA). Establish an experimental data base for future numerical studies related to ground mounted PV panels.
- Develop a numerical modelling approach with an open source software package OpenFOAM (ESI Group) and validation of the modelling approach based on the above experimental results.

- Evaluate the convective heat transfer coefficients on the surfaces of a ground mounted stand-alone solar panel under varying wind speeds and directions.

1.4 Organization of the thesis

This thesis is written in the “integrated article” format as specified by the Faculty of Graduate Studies at Western University.

This thesis is organized into 6 chapters. Chapter 1 provides a general introduction presenting an in-depth literature review related to wind loading and heat transfer for solar panels. This chapter also depicts the motivations and objectives for the present study. Chapter 2 is based on a technical paper published in the Journal of Wind Engineering and Industrial Aerodynamics on wind effects on ground mounted stand-alone solar panel using CFD. In Chapter 3, the wind flow structure around a stand-alone ground mounted PV system is analyzed using PIV and HWA in the boundary layer wind tunnel. This chapter is a technical article prepared for the Journal of Fluids and Structures. Analysis of aerodynamic forces on an array of ground mounted solar panels under varying wind direction is illustrated in Chapter 4. Chapter 4 is also based on a technical paper prepared for the Journal of Wind Engineering and Industrial Aerodynamics. Chapter 5 presents the effect of wind speed and direction on the convection heat transfer from the surfaces of a stand-alone ground mounted PV system using CFD simulations. Chapter 5 is again a technical paper which will be submitted to the Journal of Solar Energy. Finally, the thesis ends with conclusions as well as the contributions of this work and recommendations for future studies.

References

Abiola-Ogedengbe, Ayodeji, 2013. Experimental investigation of wind effect on solar panels. University of Western Ontario - Electronic Thesis and Dissertation Repository. Paper 1177. http://ir.lib.uwo.ca/etd/1177.

Abbott, D., 2010. Keeping the energy debate clean: How do we supply the world's energy needs? Proceedings of the IEEE 98, 42-66.

Aly, A., Bitsuamlak, G., 2014. Wind induced pressures on solar panels mounted on residential homes. Journal of Architectural Engineering 20, 04013003.

Aly, A., Bitsuamlak, G., 2013. Aerodynamics of ground-mounted solar panels: Test model scale effects. Journal of Wind Engineering and Industrial Aerodynamics 123, 250-260.

ASCE 7-10, 2010. Minimum Design Loads for Buildings and Other Structures. ASCE 7-10, Virginia, USA: American Society of Civil Engineers.

AS/NZS 1170.2, 2011. Australian/New Zealand Standard Structural Design Actions, Part 2: 2011. Standards Australia International Ltd., Sydney, Australia.

Banks, D., 2013. The role of corner vortices in dictating peak wind loads on tilted flat solar panels mounted on large, flat roofs. Journal of Wind Engineering and Industrial Aerodynamics 123, 192-201.

Browne, M. T. L., Gibbons, M. P. M., Gamble, S., Galsworthy, J., 2013. Wind loading on tilted roof-top solar arrays: The parapet effect. Journal of Wind Engineering and Industrial Aerodynamics 123, 202-213.

Cao, J., Yoshida, A., Saha, P., Tamura, Y., 2013. Wind loading characteristics of solar arrays mounted on flat roofs. Journal of Wind Engineering and Industrial Aerodynamics 123, 214-225.

Chung, K. M., Chang, K. C., Chou, C. C., 2011. Wind loads on residential and large-scale solar collector models. Journal of Wind Engineering and Industrial Aerodynamics 99, 59-64.

Chung, K., Chang, K., Liu, Y., 2008. Reduction of wind uplift of a solar collector model. Journal of Wind Engineering and Industrial Aerodynamics 96, 1294-1306.

Defraeye, T., Blocken, B., Carmeliet, J., 2011. Convective heat transfer coefficients for exterior building surfaces: existing correlations and CFD modelling. Energy Conversion and Management 52, 512–522.

Fage, A., Johansen, F. C., 1927. On the flow of air behind an inclined flat plate of infinite span. Proceedings of the Royal Society of London. Series A, Containing Papers of a Mathematical and Physical Character 116, 170-197.

Holman, J. P., 2002. Heat Transfer. 9th edition, The McGraw-Hill Companies, Inc. New York.

Incropera, F. P., DeWitt, D. P., Bergman, T.L. and Lavine A. S., 2006. Fundamentals of Heat and Mass Transfer. 6th edition, John Wiley & Sons. New Jersey.

Karava, P., Jubayer, C. M., Savory, E., 2011. Numerical modelling of forced convective heat transfer from the inclined windward roof of an isolated low-rise building with application to photovoltaic/thermal systems. Applied Thermal Engineering 31, 1950-1963.

Kind, R. J., Kitaljevich, D., 1985. Wind induced heat losses from solar collector arrays on flat-roofed buildings. Journal of Solar Energy Engineering 107, 335-342.

Kind, R.J., Gladstone, D.H., Moizer, A.D., 1983. Convective heat losses from flat-plate solar collectors in turbulent winds. Transactions ASME, Journal Solar Energy Engineering 105, 80-85.

Kondjoyan, A., Peneau, F., Boisson, H-C., 2002. Effect of high free stream turbulence on heat transfer between plates and air flows: A review of existing experimental results. International Journal of Thermal Sciences 41, 1-16.

Kopp, G. A., Surry, D., Chen, K., 2002. Wind loads on a solar array. Wind and Structures 5, 393-406.

Kopp, G. A. and Banks, D., 2013. Use of the wind tunnel test method for obtaining design wind loads on roof-mounted solar arrays. Journal of Structural Engineering 139, 284-287.

Kopp, G. A., Farquhar, S., Morrison, M. J., 2012. Aerodynamics mechanisms for wind loads on tilted, roof-mounted, solar arrays. Journal of Wind Engineering and Industrial Aerodynamics 111, 40-52.

Menter, F. R., 1994. Two-equation eddy-viscosity turbulence models for engineering applications. American Institute of Aeronautics and Astronautics (AIAA) Journal 32, 1598-1605.

National Building Code of Canada, 2010. National Research Council of Canada, Ottawa, Canada.

Palyvos, J. A., 2008. A survey of wind convection coefficient correlations for building envelope energy systems modeling. Applied Thermal Engineering 28, 801-808.

Pratt, R. N., Kopp, G. A., 2013. Velocity measurements around low-profile, tilted, solar arrays mounted on large flat-roofs, for wall normal wind directions. Journal of Wind Engineering and Industrial Aerodynamics 123, 226-238.

Radu, A., Axinte, E., 1989. Wind forces on structures supporting solar collectors. Journal of Wind Engineering and Industrial Aerodynamics 32, 93-100.

Radu, A., Axinte, E., Theohari, C., 1986. Steady wind pressures on solar collectors on flat-roofed buildings Journal of Wind Engineering and Industrial Aerodynamics 23, 249-258.

REN 21, 2014. Renewables 2014 Global Status Report. REN 21 Secretariat, Paris, France.

SEAOC, 2012. Wind loads on low profile solar photovoltaic systems on flat roofs, Report SEAOC-PV2-2012.Structural Engineers Association of California.

Shademan, M., Barron, R. M., Balachandar, R., Hangan, H., 2014. Numerical simulation of wind loading on ground-mounted solar panels at different flow configurations. Canadian Journal of Civil Engineering 41, 728-738.

Shademan, M., Balachandar, R., Barron, R. M., 2014b. Detached eddy simulation of flow past an isolated inclined solar panel. Journal of Fluids and Structures 50, 217-230.

Shakerin, S., 1987. Wind-related heat transfer coefficient for flat-plate solar collectors. Transaction of ASME: Journal of Solar Energy Engineering 109, 108-110.

Sharples, S., Charlesworth, P.S., 1998. Full-scale measurements of wind induced convective heat transfer from a roof-mounted flat plate solar collector. Solar Energy 62, 69-77.

Shih, T. H., Liou, W. W., Shabbir, A., Yang, Z. And Zhu, J., 1995. A new k-ϵ eddy-viscosity model for high Reynolds number turbulent flows – model development and validation. Computers & Fluids 24, 227-238.

Skoplaki, E., Palyvos, J. A., 2009. On the temperature dependence of photovoltaic module electrical performance: A review of efficiency/power correlations. Solar Energy 83, 614-624.

Sparrow, E.M., Tien, K.K., 1977. Forced convection heat transfer at an inclined and yawed square plate - Applications to solar collectors. Journal of Heat Transfer 99, 507-512.

Stathopoulos, T., Zisis, I., Xypnitou, E., 2014. Local and overall wind pressure and force coefficients for solar panels. Journal of Wind Engineering and Industrial Aerodynamics 125, 195-206.

Test, F. L., Lessman, R. C., 1980. An experimental study of heat transfer during forced convection over a rectangular body. Transaction of ASME: Journal of Heat Transfer 102, 146-151.

Test, F. L., Lessman, R. C., Johary, A., 1981. Heat transfer during wind flow over rectangular bodies in the natural environment. Transactions of the ASME: Journal of Heat Transfer 103, 262-267.

Warsido, W. P., Bitsuamlak, G. T., Barata, J., 2014. Influence of spacing parameters on the wind loading of solar array. Journal of Fluids and Structures 48, 295-315.

Wood, G. S., Denoon, R. O., Kwok, K. C. S., 2001. Wind loads on industrial solar panel arrays and supporting roof structure. Wind and Structures 4, 481-494.

Chapter 2

Numerical simulation of wind effects on a stand-alone ground mounted Photovoltaic (PV) system

2.1 Introduction

Photovoltaic (PV) panels are widely spread technology to harness solar energy. The PV technology is gaining popularity as the process of generating electricity is non-intrusive, needs little maintenance and can be used at almost any scale, i.e., from wrist watches to supplying electricity to an entire city. The installed capacity of the utility scale PV power plants or the solar farms are growing faster than the roof-top PV panels and is expected to quadruple from 2012 to 2017 (EPIA Report, 2013). PV solar farms consist of arrays of ground mounted flat plate PV panels and supply power to the electricity grid. These solar farms are usually developed in an open terrain to get unobstructed sunshine, which in turn make the PV panels in the farm experience higher wind loads and potential damage.

Wind load on a structure depends greatly on the geometry of the structure and the upstream flow condition. Several studies have been performed to estimate wind loads on

PV panels and solar collectors. These aforementioned studies can be categorized into two major classes based on their mounting locations; roof mounted and ground mounted. Roof mounted solar panels have been studied extensively (Radu et al., 1986; Radu and Axinte, 1989; Wood et al., 2001; Kopp et al., 2002; Chung et al., 2008, 2011; Meroney and Neft, 2010; Kopp and Banks, 2013; Pratt and Kopp, 2013; Banks, 2013; Browne et al., 2013; Cao et al., 2013; Aly and Bitsuamlak, 2014; Stathopoulos et al., 2014; Warsido et al., 2014) whereas the number of published literatures on the ground mounted solar panels are very few (Bitsuamlak et al., 2010; Kopp et al., 2012; Abiola-Ogedengbe, 2013; Aly and Bitsuamlak, 2013; Stathopoulos et al., 2014; Warsido et al., 2014; Shademan et al., 2014). This is because the wind tunnel testing of stand-alone ground mounted solar panels is challenging. Boundary layer wind tunnels are usually designed for testing at scales of the order of 1:100 or smaller. Therefore, testing of ground mounted solar panels with enough resolution at larger scales (1:30 and less) brings up the problem of artificially simulating the lowest 10 meters of the atmospheric boundary layer (ABL), the surface layer. Both studies by Bitsuamlak et al. (2010) and Shademan et al. (2014) used Computational Fluid Dynamics (CFD) approach to estimate wind loads on the ground mounted solar panels. Bitsuamlak et al. (2010) investigated the aerodynamic features of a stand-alone PV system and it was found that the pressure coefficients on the panel were underestimated by CFD when compared with full-scale experimental results. Also, when arranged in tandem, sheltering effect from the upwind panels reduced wind loads on the adjacent panels. Shademan et al. (2014) performed steady Reynolds-Averaged Navier-Stokes (RANS) simulations to measure wind loading on the ground mounted solar panel both in stand-alone and array configurations. For the validation of the numerical model, a 2D inclined flat plate was performed and the mean pressure coefficients (C_P) on the plate were compared with Fage and Johansen (1927). Validation results showed that the Shear Stress Transport (SST) k-ω performed better than the Realizable k-ε turbulence model. For the stand-alone system, maximum aerodynamic force was found for 0^o and 180^o wind directions. Kopp et al. (2012) studied wind loading on the ground mounted array to illustrate the effect of the building for the roof mounted solar panel arrays. In this study wind tunnel pressure measurements were performed at the Boundary Layer Wind Tunnel II (BLWT II) at the University of Western Ontario. The primary focus of this study was roof mounted arrays and it was found that there was a substantial difference in aerodynamics loading between ground mounted and roof mounted solar panel arrays due to the interaction of the flow with the building itself. Abiola-Ogedengbe (2013) performed pressure tests on the 1:10 scale model of a ground mounted solar panel in the BLWT I at the Western University, Canada for different inclination angles (25^o and 40^o) under four different wind directions (0^o, 30^o, 150^o and 180^o). 150^o and 180^o wind directions were found to be critical in terms of maximum lift. Particle Image Velocimetry (PIV) was also performed on the same solar panel system by Abiola-Ogedengbe (2013). However, only the 0^o wind direction was considered in this PIV experiment. Aly and Bitsuamlak (2013) investigated the effect of geometric scales on the wind loading of stand-alone ground mounted solar panel using both wind tunnel and computational fluid dynamics (CFD) studies. Several cases between 1:50 and 1:5 geometric scales with 25^o and 40^o solar panel tilt angles were studied. It was observed that while the mean pressures were not significantly affected by model scales, the standard deviation and peak pressure coefficients varied. Stathopoulos et al. (2014) conducted wind tunnel experiments to estimate wind loads on the stand-alone solar panel on the flat and gable roofs as well as one case with the solar panel on the ground. For the ground mounted system, the maximum and minimum peak pressure coefficients were observed for 30^o and 135^o wind directions respectively. Warsido et al. (2014) studied the effect of row spacing for an array of solar panels mounted on the flat roof of a building and also on the ground using wind tunnel tests.

Building codes, such as ASCE 7-10 (2010) also do not provide a clear guideline to estimate wind loads on the ground mounted PV systems. The closest of the ground mounted solar panel structure that could be found in the ASCE 7-10 (2010) is the mono-slope free roof. Minimum design wind loads for only 0^o and 180^o wind directions are provided in the code. Although mono-slope free roofs are geometrically similar to the ground mounted stand-alone solar panels, to what extent the minimum design loads for the roofs could be applied for the solar panel clearly needs further investigation.

The present research is aimed at better understanding the effect of wind on the ground mounted stand-alone PV system by estimating the wind loads and by relating the loads to the wind flow field around the panel. CFD simulations are employed herein in order to investigate the flow field, surface pressures and overall aerodynamic loading of the ground-mounted solar panel. CFD has the advantage of simulating the wind-structure interaction in full scale as well as providing high spatial resolution at low cost. Also, the recent advancement in computational power encourages adopting CFD approach.

However, as RANS approaches in CFD use various models to represent the turbulence stress tensor, the accuracy of CFD is an important concern and careful application, validation and verification are needed.

2.2 Numerical model

In this study, 3D RANS simulations of wind flow over a ground mounted stand-alone PV system in full scale are performed using an unsteady solver with steady inlet conditions. The geometry of the stand-alone configuration is obtained from the specification provided by the manufacturer. The stand-alone PV system consist of 24 panels arranged in a 4 (row) × 6 (column) array. The small gaps within the panel are not considered here since the ratio between the gap sizes (each gap size 25 mm vertically and 19 mm laterally) and the largest dimension of the stand alone PV system (7.3 m in lateral direction) is low (less than 1.3%). To have a reliable solution with the gaps, mesh in the gaps needs to be very fine and to be consistent with the mesh in the gaps, the number of cells in the whole domain would be computationally prohibitive. Also, a recent study by Wu et al. (2010) showed that the influence of gaps (ratio between the gap size and the largest dimension of the PV panel up-to 8.9%) on wind loading of heliostat type solar devices is negligible. The overall dimension of the stand-alone system is 2.48 m (B) × 7.29 m (W) × 1.65 m (H) (Fig. 2.1). The inclination of the panel with the horizontal is 25^o. This inclination angle is chosen based on the optimum annual power output at places with latitudes roughly between 30^o and 45^o. Solar farms within this latitude (e.g., 97 MW Sarnia solar farm in Ontario, Canada; 30 MW Cimarron Solar Facility, New Mexico,

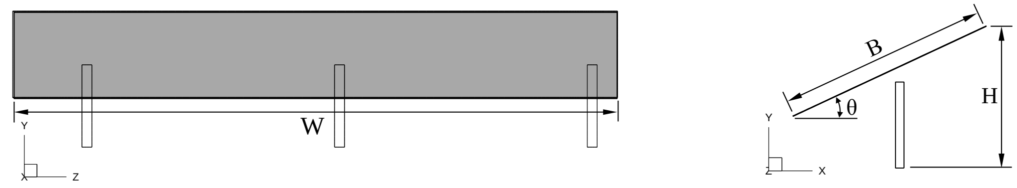

(a) (b)

Figure 2.1: Computational model of the stand-alone PV system (a) front view (b) side view.

USA; 21 MW Blythe Solar Project, California, USA) have a mounting tilt angle of 25°. CFD simulations have been performed for five different wind directions (α°) (Fig. 2.2) ranging from 0° to 180° at 45° intervals. However, results for 90° wind direction are not reported here since for this wind direction mean pressure coefficient (C_p) values on the surfaces of the panel is almost uniform and drag, lift and moment coefficients are almost zero. This is due the very low thickness of panel acting as a very thin vertical flat plate which barely affects the incoming flow. The computational domain (Fig. 2.3) and grid (Fig. 2.4) are created according to the COST guidelines (Franke et al., 2007) using grid generating software Pointwise (Pointwise, Inc.). The overall size of the computational domain is 21.4H (length) × 6H (height) × 24.2H (width) with an upstream fetch of 5H,

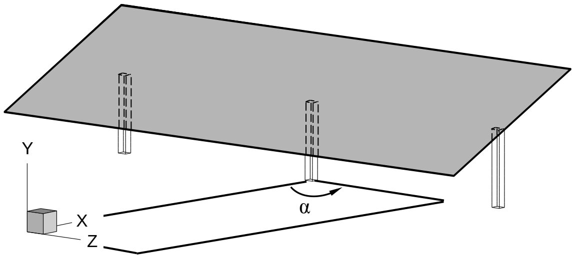

Figure 2.2: Wind direction α°.

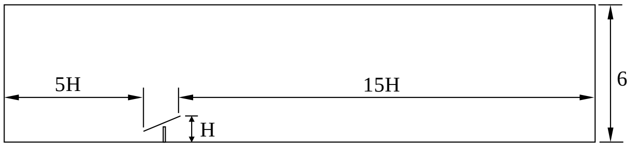

Figure 2.3: Computational domain.

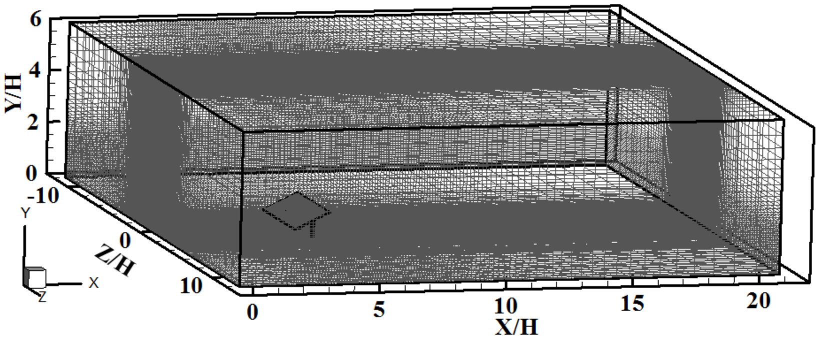

(a)

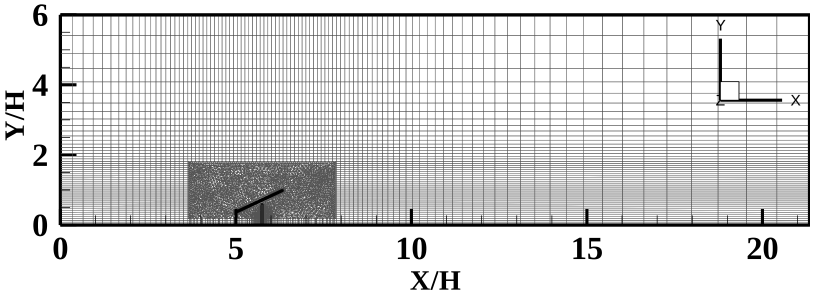

(b)

Figure 2.4: (a) 3D isometric and (b) 2D sectional view of the computational grid.

downstream length of 15H, height above the panel of 5H and clearances of 9.9H from the side walls of the domain (Fig. 2.3, 2.4). For different wind directions, computational domains and grids are modified accordingly. The total number of cells in the domain is about 1.7 million and is chosen based on grid sensitivity study among three systematically and substantially refined grids having 852,522 (G1); 1,696,984 (G2) and

2,608,659 (G3) cells. The grid sensitivity is performed based on the surface averaged mean pressure coefficient (C_P) on both windward and leeward surfaces of the solar panel for 0^o wind direction. The refinement ratio between G1 and G2 is about 1.5 and between G2 and G3 is about 1.2. The difference in surface averaged mean C_p on the windward and leeward surfaces of the solar panel for 0^o wind direction is within 4.2% between G1 and G2 and within 1.1% between G2 and G3. The chosen grid G2 has minimum grid size of 0.003H (X), 0.002H (Y), 0.006H (Z) and maximum grid size of 0.88H in all X, Y and Z direction (see Fig. 2.4 for the orientation of X, Y and Z axis).

At the domain inlet, velocity and turbulence intensity (TI) profiles are obtained from Engineering Sciences Data Unit (ESDU 82026, 83045) for wind speed of 26 m/s at 10 m height and with aerodynamics roughness length of 0.03 m which represents open terrain. The wind speed is chosen based on the maximum mean hourly wind speed data recorded at London, Ontario airport. This translates in a Reynolds number of 2.13×10^6 based on the wind speed at the panel's lower edge height and the chord length of the panel (B).

The turbulent kinetic energy profile, calculated from the ESDU velocity and turbulent intensity, is matched with Yang's profile (Yang et al., 2009 a, b) to obtain the equilibrium Atmospheric Boundary Layer (ABL). Equilibrium ABL, which is one of the pre-requisite for an accurate ABL simulation, means the streamwise gradients of the flow parameters (e.g., velocity, turbulent kinetic energy (k), turbulence dissipation rate (ε) and specific turbulence dissipation rate (ω)) should be zero in an empty domain. The bottom of the domain is modeled as no-slip rough wall with roughness height (k_s) and roughness constant (C_s). In this study k_s value of 0.031m and C_s value of 9.477 are used which are in accordance with the $k_s = Ey_0/C_s$ relationship (Blocken et al., 2007), where E is an integration constant (≈ 9.793) and y_0 is the aerodynamic roughness length (0.03 m for open terrain). Also, k_s is chosen based on the first cell center distance (y_P = 0.032 m) from the ground wall and follows $y_p > k_s$. This is again essential to obtain an equilibrium ABL flow. The sides of the domain are modeled as symmetry. Fixed values of velocity and turbulence properties from the top of the inlet profile are imposed at the top of the entire domain. Panel and support structures surfaces are treated as no-slip smooth walls. At the outlet of the domain, a zero gradient boundary condition is imposed.

Simulations are performed using the SST k-ω turbulence model. The SST k-ω model, developed by Menter (1994), models flows with adverse pressure gradients and separation more accurately than the standard k-ω model by Wilcox (1998). The model consists of a blending of the equations, such that the SST k-ω model retains the robustness and accuracy associated with the standard k-ω model near the wall in the viscous sub-layer and logarithmic part of the boundary layer, while retaining the free stream independence and the more accurate prediction of free stream layers obtained by the high Re version of the k-ε model (see Appendix A for the governing equations). Also, the SST k-ω turbulence model has successfully been employed in ABL flow simulation by several researchers (Yang et al., 2009 b; Karava et al., 2011; Yu, 2012) (see Appendix B for a comparison between Realizable k-ε and SST k-ω turbulence models). The SST k-ω turbulence model constants are modified based on Menter (1994), Yang et al. (2008) and Yang et al. (2009 a, b) according to the incoming flow conditions (Appendix C). The turbulence model constants used in this study are reported in Table 2.1. Simulation of wind flow inside an empty domain, to check horizontal homogeneity of the flow, is performed. Figure 2.5 shows that the inlet and incident velocity and turbulence intensity profiles match very closely with streamwise gradients of 4% for velocity and 5% for turbulence intensity. In Figure 2.5, velocity and distance are normalized by the velocity at the top of the domain (U_R) and the height of the domain (y_R) respectively.

Table 2.1: SST k-ω turbulence model constants employed in the present study.

α_{k1}	α_{k2}	$\alpha_{\omega1}$	$\alpha_{\omega2}$	β_1	β_2	β^*	γ_1	γ_2	a_1	c_1
0.85034	1.0	0.5	0.85616	0.032	0.0368	0.04	0.38	0.44	0.31	10.0

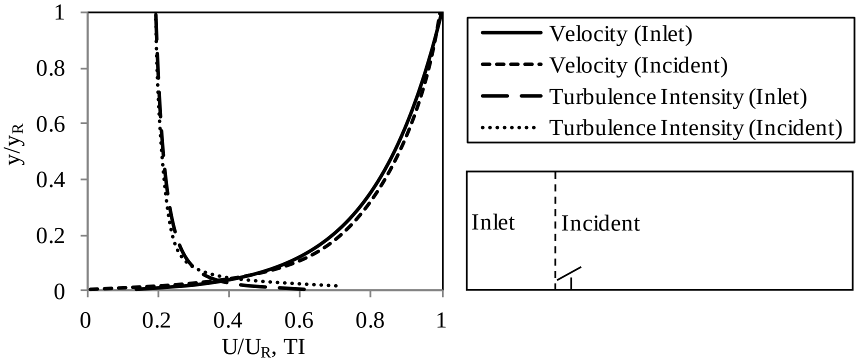

Figure 2.5: Inlet and incident velocity and turbulence intensity profiles.

Simulations are performed using open source CFD toolbox OpenFOAM 2.1.0 (ESI Group). In this study pisoFoam solver, which is a transient solver for incompressible flows that uses PISO (Pressure Implicit with Splitting of Operators) algorithm (Issa, 1986), is employed. In OpenFOAM, for the incompressible Reynolds-Averaged Simulations, wall functions are implemented through the boundary conditions specified for the kinematic turbulent viscosity. At the no-slip smooth solar panel surfaces "nutkWallFunction" is employed. This wall function uses logarithmic law of the wall to model kinematic turbulent viscosity and calculates dimensionless wall distance based on turbulent kinetic energy. On the other hand "nutURoughWallFunction", in which the law of the wall is modified for roughness based on the roughness parameters (k_s, C_s), is implemented at the bottom of the domain. Dimensionless wall distance y^* ($y^* = C_\mu^{1/4} k_P^{1/2} y_P / \nu$, where C_μ is a turbulence model constant ($= \beta^*$ for SST k-ω), k_p is the turbulent kinetic energy at the first cell center from the wall (m^2/s^2), y_P is the first cell center height from the wall (m), ν is the kinematic viscosity (m^2/s)) on the upper and lower surfaces of the solar panel for 0^o, 45^o, 135^o and 180^o wind directions is within 30 to 300 except at the edges. Convergence criteria of 10^{-6} are employed for all variables. Linear interpolation scheme, Gauss limited linear divergence scheme and cellMD limited Gauss linear gradient scheme are used for discretization. Time step size of 10^{-5} s is employed. Time step for the simulation is chosen to have a Courant number less than 1. Courant number reflects the number of cells the flow travels in a single time step and is defined as, $Cr = v\Delta t/\Delta l$ where v is the local mean wind speed (m/s), Δt is the time step (s) and Δl is the grid cell size (m). Simulations are run for a total of 20 s of flow time and average of last 15 s is taken to analyze results. During the simulation the flow reaches steady state after around 5 s of flow time based on the panel surface pressures. Hence, averaging of last 15 s of flow time should provide enough data to compute the results. Simulations are performed over the SHARCNET (Shared Hierarchical Academic Research Computing Network, www.sharcnet.ca) cluster using 128 processors. Each simulation takes approximately 300 hours of elapsed real time to converge on this cluster.

2.3 Results and discussion

This section starts with discussing the surface pressure distributions and then followed by the aerodynamic loading on the solar panel. The wind flow field around the solar panel is then addressed in relation to the surface pressures and aerodynamic loading of the panel.

2.3.1 Surface pressures

Distributions of mean C_p on the upper and lower surfaces of the PV system for various wind directions are shown in Figure 2.6 and demonstrate the three dimensional effect of the flow. For 0^o and 180^o wind directions, symmetry in the mean C_p distributions about the mid-line along the breadth of the panel on both upper and lower surfaces is observed. For the windward surfaces (upper surface for 0^o and lower surface for 180^o), C_p values are higher at the middle of a spanwise line and decrease towards edges. This is expected as the flow accelerates at the edges and creates a low pressure region on the panel surface. For 45^o and 135^o wind directions, at the windward surface, i.e., the upper surface for the 45^o wind direction and the lower surface for the 135^o wind direction, mean C_p values decrease diagonally on the surfaces. Mean C_p distributions on the panel surfaces in the flow separated region for 45^o and 135^o wind directions, i.e., lower surface for 45^o and upper surface for 135^o wind directions, demonstrate the possible existence of corner vortices on those surfaces. Almost similar patterns of mean C_p distributions can be observed for both of these leeward surfaces. However, suction pressure (negative mean pressure) increases at the upper surface for the 135^o wind direction compared to the lower surface for the 45^o wind direction. For all wind directions, localized maximum net pressures are observed close to the leading edge of the panel with a decrease towards the trailing edge of the panel. This means that the localized wind loads are maximum close to the leading edge of the PV panel for all the wind directions studied here.

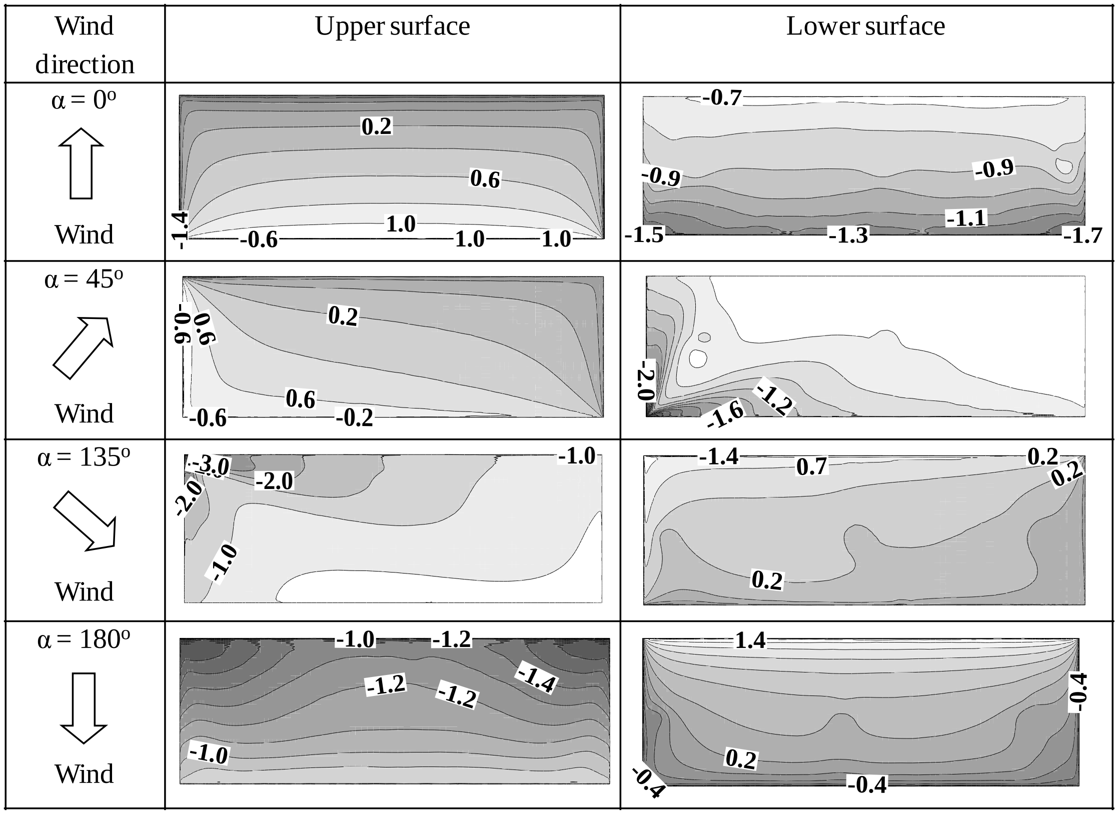

Figure 2.6: Mean C_p contours on the panel surfaces.

Mean C_p values along the mid-line of the stand-alone PV system on the upper and lower surfaces of the panel for 0^o and 180^o wind directions are compared with the experimental results by Abiola-Ogedengbe (2013) (Fig. 2.7). Full scale dimensions of the panel in both the experimental study and the present study are the same. However, the CFD model of the present study does not have all the structural support elements at the back of the panel

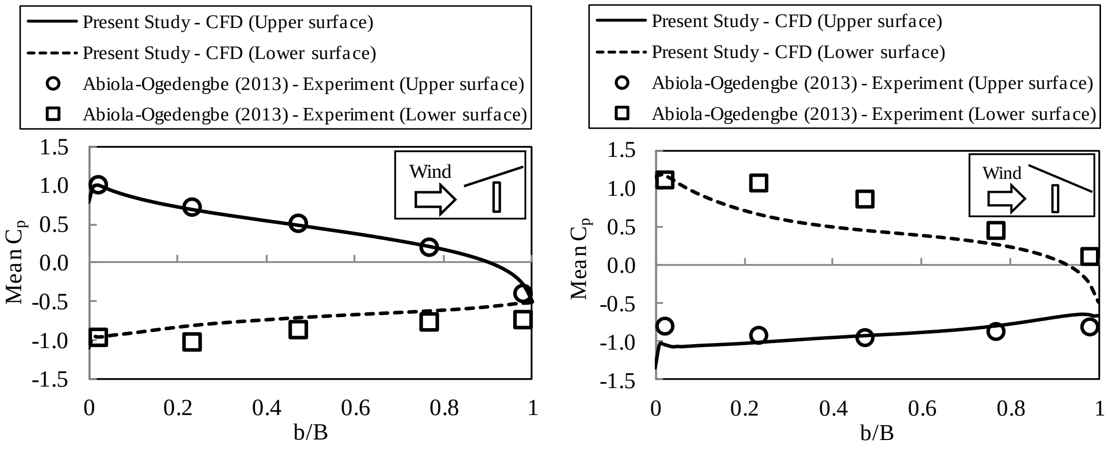

(a) (b)

Figure 2.7: Mean C_p profiles along the mid-line of the panel surface for wind directions of (a) 0^o and (b) 180^o. Here, b is the distance from the leading edge along the breadth of the panel.

as in the experimental model. To make the comparison meaningful, reference pressure and wind speed to calculate C_p are taken at the same location as the experiment (0.82 m from the ground at the full scale). A good match of mean C_p between CFD and experiment is obtained on the upper surface of the panel for both 0^o and 180^o wind directions. For the lower surfaces, the match is not as good due to all the structural elements present at the lower surface of the experimental model. Although there is a scaling difference between CFD (full scale) and experiment (1:10 scale), a reasonable agreement of mean C_p values is found. A recent study by Aly and Bitsuamlak (2013) showed that, within the geometric scale of 1:10 to 1:50, mean wind loads on the solar panels are independent of the scale.

2.3.2 Aerodynamic loading

Time histories of drag (CD) and lift (CL) coefficients are shown in Figure 2.8. CD is calculated using CD = CNcos(90-θ), where CN is the net area weighted average pressure coefficient from the upper and lower surface of the panel and θ is shown in Figure 2.1 (b) which is 25^o in this study. Similarly, CL is calculated using CL = CNsin(90-θ). Sign conventions used in Figure 2.8 are as follows; drag acting against the flow is positive and upward lift is positive. Figure 2.8 demonstrates that after about 3s of flow time the solution become steady for all four wind directions. Figure 2.8 also illustrates that the maximum upward lift is observed for the 180^o wind direction whereas 0^o wind direction causes the maximum negative lift. Almost comparable drag is found for 0^o and 180^o wind directions (14% difference) and also for 45^o and 135^o wind directions (17% difference). However, 0^o and 180^o wind directions show a slightly higher drag than 45^o and 135^o wind directions. Mean drag, lift and overturning moment coefficients are reported in Figure 2.9. Two different overturning moment coefficients, about X axis (CMx) and Z axis (CMz), are evaluated here. Overturning moment coefficients (CM) are calculated using $CM = M/(0.5\rho U_{ref}^2 A_{ref} L)$, here M is the net moments from the upper and lower surfaces of the panel (N-m), U_{ref} is the reference velocity measured at the lower edge height (0.6 m) of the panel (m/s), A_{ref} is the surface area of the panel (m^2) and L is the length scale of the panel which is the breadth of the panel (B) for CMx and width of the panel (W) for CMz (m). Centre of the inclined solar panel surface is taken as the reference point for the moment calculation. Figure 2.9 also shows the coefficient of net pressure, CN on the solar panel surface. Some interesting observations can be made from Figure 2.9.

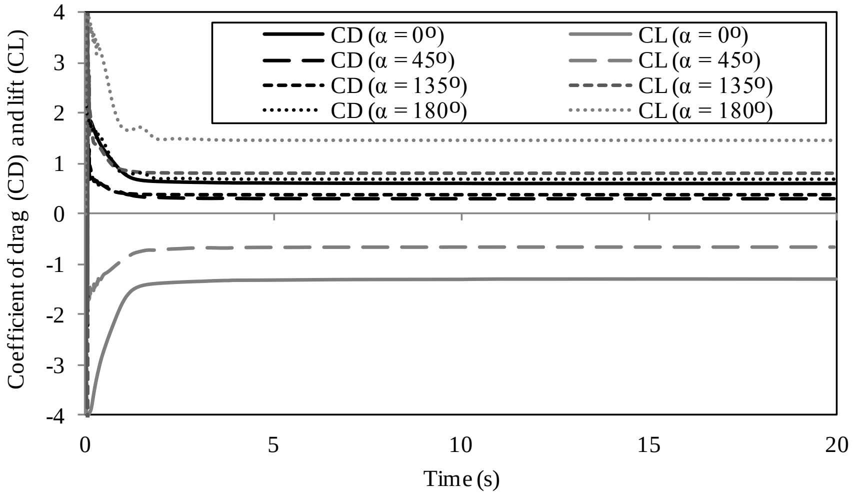

Figure 2.8: Time history of drag (CD) and lift coefficient (CL) averaged over the entire PV panel.

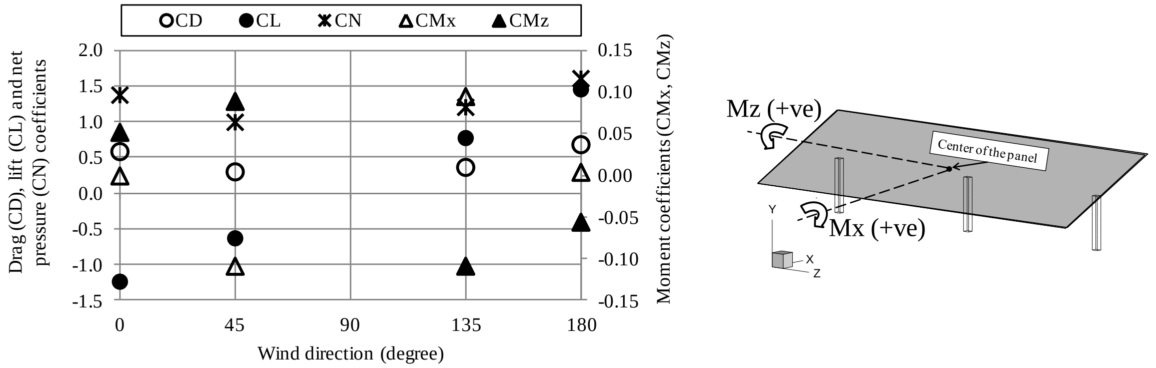

Figure 2.9: Mean drag, lift, net pressure and moment coefficients for different wind directions and the direction of positive momentum.

Although higher values of drag and lift are found for 0^o and 180^o wind directions, higher overturning moment is found for 45^o and 135^o wind directions. So, in terms of net pressure acting on the solar panel, 180^o wind direction is the most critical case among all four wind direction cases studied here. On the other hand, in terms of overturning of the panel, 45^o and 135^o are the critical cases than 0^o and 180^o wind directions. Mean drag and lift coefficients for 0^o and 180^o wind directions are compared with the minimum design load for monoslope free roofs by building code ASCE 7-10 (2010) (Fig. 2.10). In the code, minimum design loads for two load cases, load case A and B, are provided. Comparisons with both load cases are shown in Figure 2.10 as according to ASCE 7-10 (2010) "Application of both load cases is required to envelop the combinations of maximum normal forces and moments that are appropriate for the particular roof shape and blockage configuration." The design pressure can be obtained by multiplying the prescribed mean pressure coefficient with the dynamic pressure corresponding to the design wind speed and the gust factor ($p = qG_fC_N$, here p is the design pressure (Pa), q is the dynamic pressure (Pa), G_f is the gust factor and C_N is the net mean pressure coefficient). Under the assumption of quasi steady theory, mean pressure coefficients can be used to calculate the design pressure. From Figure 2.10 it can be seen that the mean drag and lift coefficients obtained in this study are approximately within 20% of load

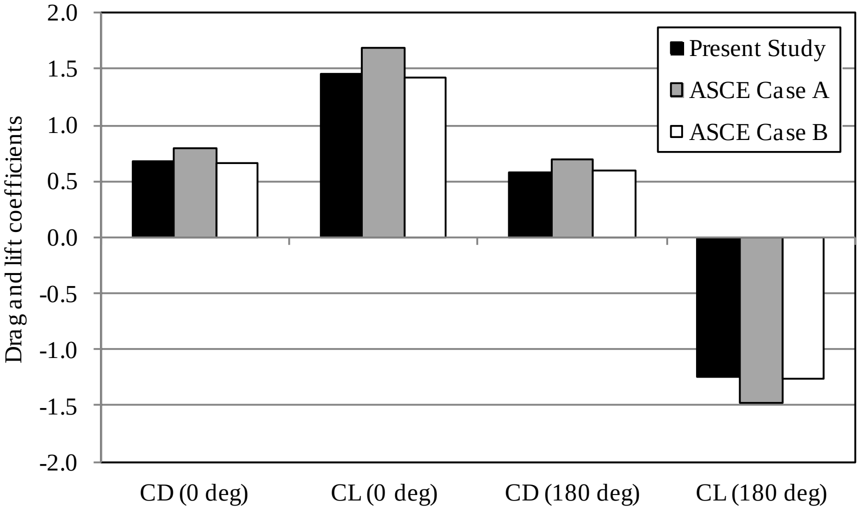

Figure 2.10: Comparison of mean drag and lift coefficients with ASCE 7-10 building code.

case A and 2% of load case B. Figure 2.10 also illustrates the fact that even though the code is for monoslope free roofs, it can be used for ground mounted stand-alone solar panels when the criteria for panel dimensions (ratio of the panel mid-point height and the horizontal projection of the panel between 0.25 to 1 and inclination angle $\leq 45^o$) and wind directions (0^o and 180^o) are met (ASCE 7-10, 2010). However, further investigations are needed to confirm this finding.

2.3.3 Wind flow field

To analyze the wind flow field around the solar panel, streamlines of mean velocity at the plane through the middle support leg and parallel to the side edges on the panel are superimposed on the mean C_p profiles for all wind directions (Fig. 2.11). In Figure 2.11, the distances are normalized by the lower edge height of the panel from the bottom surface of the domain ($y_{L.E.}$). The incoming flow remains attached on the windward surface, whereas it separates at the leading edge towards the leeward surface for all four wind directions. This resulted in positive pressures on the most of the windward surface and negative pressures on the leeward surfaces (Fig. 2.11). Also, the stagnation point is close to the leading edge on the windward surfaces for all directions and thus the maximum mean C_p is observed in those areas. From the leading edge towards the trailing edge on the windward surface for all wind directions, mean C_p decreases as the flow accelerates. For 0^o wind direction, two vortices both rotating counter clockwise are observed at the leeward side of the panel (Fig. 2.11 a). The mounting stand is the reason of two separate vortices in Figure 2.11 (a), otherwise a single standing vortex rotating counter clockwise is observed between two mounting stands. Also, from the mean C_p

profile in Figure 2.11 (a), it is observed that the vortex close to the leading edge results in higher negative pressure compared to the trailing edge vortex. For 180° wind direction, flow separates at the leading edge towards the leeward side of the panel and forms a big separation bubble rotating clockwise (Fig. 2.11 d). This large separation bubble covers almost the entire leeward side of the solar panel and thus creates a uniform pressure distribution which is also evident from Figure 2.6. Close to the trailing edge a small

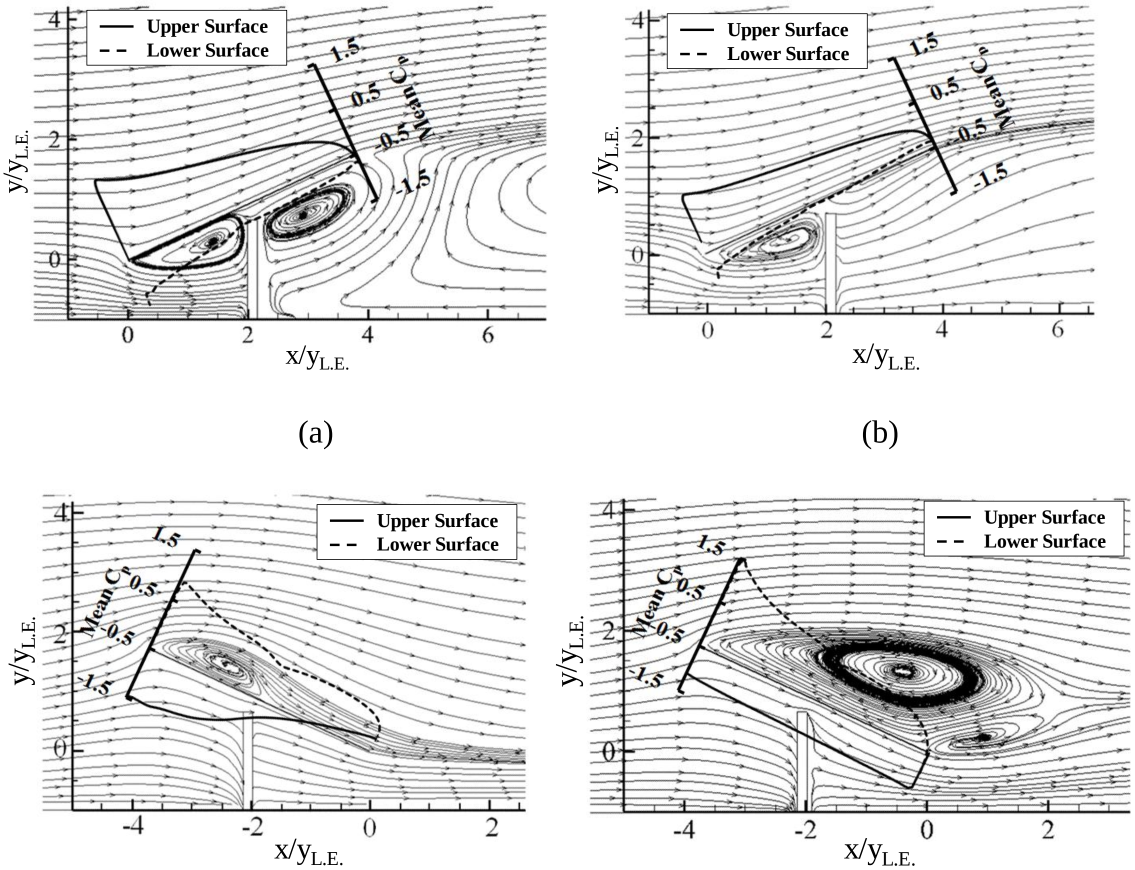

(a) (b)

(c) (d)

Figure 2.11: Streamlines on the plane parallel to the side edges of the panel through the middle support leg with the mean C_p profiles for the wind directions of (a) 0° (b) 45° (c) 135° and (d) 180°.

counter clockwise rotating vortex is also observed due to the rolling up of the shear layer from the trailing edge (Fig. 2.11 d). For 45° and 135° wind directions, vortices close to the leading edge on the leeward surface of the panel shown in Figure 2.11 (b, c) are actually the cross-section of the corner vortices and are more evident in the 3D plots of the panel presented in Figure 2.12. In Figure 2.12, the streamlines required to show the existence of the corner vortices are only plotted, both for 45° and 135° wind directions. The corner vortices are responsible for the higher negative mean C_p close to the leading edge (Fig. 2.11 b,c) and also the cone shaped mean C_p distribution on the leeward side (Fig. 2.6) for these two wind directions. The corner vortices are also responsible for higher momentum coefficients for 45° and 135° wind directions than 0° and 180° (Fig. 2.9). Snapshots of spanwise vorticity (ω_z) contours along the plane through the middle support leg and parallel to the side edges of the panel at 20 s of flow time are shown in Figure 2.13. In this figure contours of ω_z close to the panel are presented. However, after examining the vorticity contours in the whole domain for all four wind directions, shedding of vortices are not detected. Similar observation is reported by Breuer et al. (2003) when flow around an inclined plate was studied using RANS modelling approach.

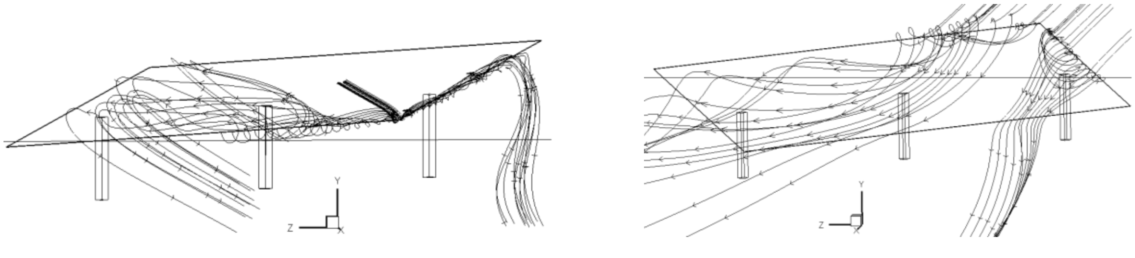

(a) (b)

Figure 2.12: Corner vortices on the leeward side of the panel for (a) 45° and (b) 135° wind directions.

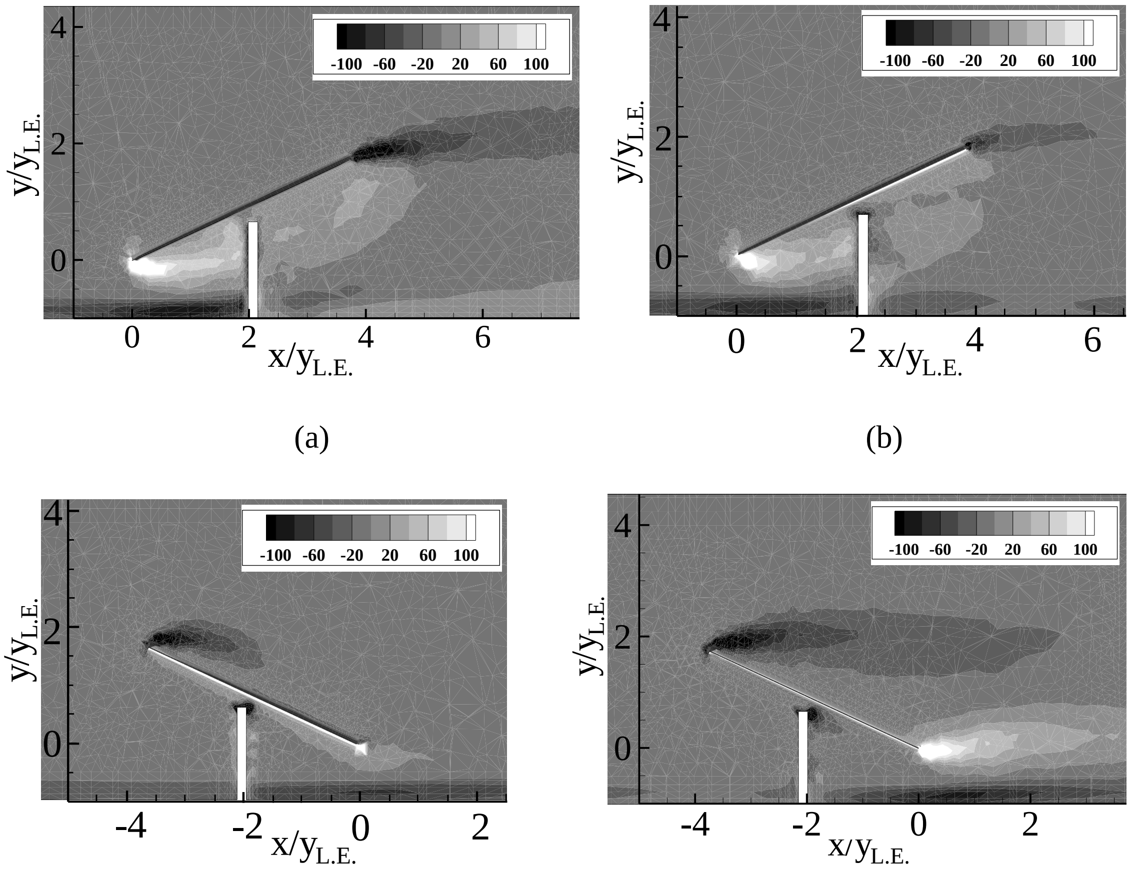

(a) (b)

(c) (d)

Figure 2.13: Contours of spanwise vorticity (ω_z) on the plane parallel to the side edges of the panel through the middle support leg for different wind directions (a) 0^o, (b) 45^o, (c) 135^o and (d) 180^o.

It was reported that RANS modelling approach were not able to capture shedding of vortices whereas Large Eddy Simulation (LES) and Detached Eddy Simulation (DES) were able to reproduce asymmetric vortex shedding. Therefore, LES and DES studies are encouraged as future work for the stand-alone PV system presented here. However, to perform LES or DES on this PV system, full scale simulations may not be feasible due to high Reynolds number ($>10^6$). According to Spalart et al. (1997), for Reynolds number of about 10^7, a computational grid consisting of a minimum of 10^{11} cells has to be used. In the study by Breuer el al. (2003) on the flow around an inclined plate, for the Reynolds number of 2×10^4 based on chord length, the number of cells that provided reasonable results were 2×10^6 for DES and 9×10^6 for LES.

In order to better understand the vorticity structure and to investigate the wake structure behind the panel, isosurfaces of spanwise vorticity at the final time step (20 s) around the PV panel for all four wind directions are shown in Figure 2.14. As expected, the wake is symmetric for 0^o and 180^o but not for 45^o and 135^o wind directions. Symmetry and asymmetry in the wake produced symmetric and asymmetric pressure distributions at the leeward surfaces of the solar panel (Fig. 2.6) for the normal (0^o and 180^o) and oblique (45^o and 135^o) wind directions respectively. It can be seen from Figure 2.14 that, for 0^o and 180^o wind directions tip vortices do not interact with the leading edge vortices. However, for the 45^o and 135^o wind directions, the tip vortices merge with the corner vortices as the flow evolves. Also, for 0^o and 45^o wind directions the tip vortices are attracted to each other whereas it is the opposite for 135^o and 180^o wind directions. Overall, the behaviour of the tip vortices and thus the wake structures vary substantially with wind directions.

$\alpha = 0^o$ ($\omega_z = 2$)	$\alpha = 45^o$ ($\omega_z = 1$)	$\alpha = 135^o$ ($\omega_z = -8$)	$\alpha = 180^o$ ($\omega_z = -10$)

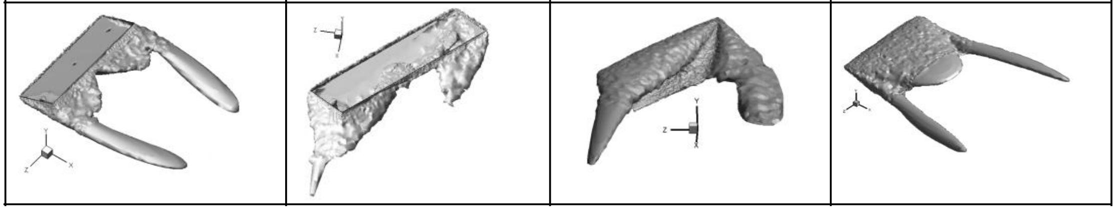

Figure 2.14: Isosurface of spanwise vorticity at the final time step (20 s) for all four wind directions.

2.4 Conclusions

The present study was undertaken to investigate the effect of wind on the ground mounted stand-alone photovoltaic (PV) system under varying wind direction using Reynolds-Averaged Navier-Stokes (RANS) numerical approach using an unsteady solver with steady inlet conditions. Mean pressure coefficient (C_p) distributions on the surfaces of the solar panel indicate that the maximum wind load occurs close to the leading edge for all four different wind directions. For 0^o and 180^o wind directions, symmetry in both mean C_p distributions as well as the wake structures, about the streamwise mid-line of the panel, is observed. However, for 45^o and 135^o wind directions these properties become asymmetric and thus result in increased overturning moments than for the 0^o and 180^o wind directions. Critical wind directions according to this study are: 0^o and 180^o for maximum drag, 180^o for maximum uplift and 45^o and 135^o are for maximum over turning moments. Investigation of the wind flow field around the solar panel did not show any presence of vortex shedding which is due to the shortcomings of the RANS modelling approach. However, corner vortices were found on the leeward surfaces for the 45^o and 135^o wind directions. Mean drag and lift coefficients of the panel showed a reasonable agreement when compared with minimum design loads for monoslope free roofs by ASCE 7-10 (2010). This suggests that the minimum design loads for monoslope free roofs may be used with care for the solar panel cases where the dimension of the panel and wind directions fall within the criteria set by the code. Scaling difference did not have an important effect on the mean C_p when numerical results (full scale) were compared with experimental results by Abiola-Ogedengbe (2013) (1:10 scale). However, effect of scaling on the wind flow field needs to be investigated in the future. Although RANS modelling approach was not able to capture vortex shedding, wind loading (drag, lift and overturning moments) on the panel and other flow structures (corner vortices, separation of shear layer, tip and leading edge vortices) were well predicted and can be used where computationally less demanding numerical approaches are necessary.

References

Abiola-Ogedengbe, Ayodeji, 2013. Experimental investigation of wind effect on solar panels. University of Western Ontario - Electronic Thesis and Dissertation Repository. Paper 1177. http://ir.lib.uwo.ca/etd/1177.

Aly, A., Bitsuamlak, G., 2014. Wind induced pressures on solar panels mounted on residential homes. Journal of Architectural Engineering 20, 04013003.

Aly, A., Bitsuamlak, G., 2013. Aerodynamics of ground-mounted solar panels: Test model scale effects. Journal of Wind Engineering and Industrial Aerodynamics 123, 250-260.

ASCE 7-10, 2010. Minimum Design Loads for Buildings and Other Structures. ASCE 7-10, Virginia, USA: American Society of Civil Engineers.

Banks, D., 2013. The role of corner vortices in dictating peak wind loads on tilted flat solar panels mounted on large, flat roofs. Journal of Wind Engineering and Industrial Aerodynamics 123, 192-201.

Bitsuamlak, G. T., Dagnew, A. K., Erwin, J., 2010. Evaluation of wind loads on solar panel modules using CFD. The Fifth International Symposium on Computational Wind Engineering, Chapel Hill, North Carolina, USA, May 23-27.

Blocken, B., Stathopoulos, T., Carmeliet, J., 2007. CFD simulation of the atmospheric boundary layer: wall function problems. Atmospheric Environment 41, 238-252.

Breuer, M., Jovicic, N., Mazaev, K., 2003. Comparison of DES, RANS and LES for separated flow around a flat plate at high incidence. International Journal for Numerical Methods in Fluids 41, 357-388.

Browne, M. T. L., Gibbons, M. P. M., Gamble, S., Galsworthy, J., 2013. Wind loading on tilted roof-top solar arrays: The parapet effect. Journal of Wind Engineering and Industrial Aerodynamics 123, 202-213.

Cao, J., Yoshida, A., Saha, P., Tamura, Y., 2013. Wind loading characteristics of solar arrays mounted on flat roofs. Journal of Wind Engineering and Industrial Aerodynamics 123, 214-225.

Chung, K. M., Chang, K. C., Chou, C. C., 2011. Wind loads on residential and large-scale solar collector models. Journal of Wind Engineering and Industrial Aerodynamics 99, 59-64.

Chung, K., Chang, K., Liu, Y., 2008. Reduction of wind uplift of a solar collector model. Journal of Wind Engineering and Industrial Aerodynamics 96, 1294-1306.

ESDU, 1982. Strong winds in the atmospheric boundary layer. Part 1: Mean hourly wind speeds. Engineering Science Data Unit Number 82026.

ESDU, 1983. Strong winds in the atmospheric boundary layer. Part 2: Discreet gust speeds. Engineering Science Data Unit Number 83045.

EPIA Report, 2013. European Photovoltaic Industry Association - Global Market Outlook for Photovoltaics 2013-2017.

Fage, A., Johansen, F. C., 1927. On the flow of air behind an inclined flat plate of infinite span. Proceedings of the Royal Society of London. Series A, Containing Papers of a Mathematical and Physical Character 116, 170-197.

Franke, J., Hellsten, A., Schlunzen, H., Carissimo, B., 2007. Best practice guideline for the CFD simulation of flows in the urban environment. COST Action 732; Quality assurance and improvement of microscale meteorological models.

Issa, R. I., 1986. Solution of implicitly discretized fluid flow equations by operator splitting. Journal of Computational Physics 62, 40-65.

Karava, P., Jubayer, C.M., Savory, E., 2011. Numerical modelling of forced convective heat transfer from the inclined windward roof of an isolated low-rise building with application to photovoltaic/thermal systems. Applied Thermal Engineering 31, 1950-1963.

Kopp, G. A., Banks, D., 2013. Use of wind tunnel test method for obtaining design wind loads on roof-mounted solar arrays. Journal of Structural Engineering 139, doi: 10.1061/(ASCE)ST.1943-541X.0000654.

Kopp, G. A., Farquhar, S., Morrison, M. J., 2012. Aerodynamics mechanisms for wind loads on tilted, roof-mounted, solar arrays. Journal of Wind Engineering and Industrial Aerodynamics 111, 40-52.

Kopp, G. A., Surry, D., Chen, K., 2002. Wind loads on a solar array. Wind and Structures 5, 393-406.

Menter, F. R., 1994. Two-equation eddy-viscosity turbulence models for engineering applications. American Institute of Aeronautics and Astronautics (AIAA) Journal 32, 1598-1605.

Meroney, R. N., Neft, D. E., 2010. Wind effects on roof-mounted solar photovoltaic arrays: CFD and wind-tunnel evaluation. The Fifth International Symposium on Computational Wind Engineering, Chapel Hill, North Carolina, USA.

Pratt, R. N., and Kopp, G. A., 2013. Velocity measurements around low-profile, tilted, solar arrays mounted on large flat-roofs, for wall normal wind directions. Journal of Wind Engineering and Industrial Aerodynamics 123, 226-238.

Radu, A., Axinte, E., 1989. Wind forces on structures supporting solar collectors. Journal of Wind Engineering and Industrial Aerodynamics 32, 93-100.

Radu, A., Axinte, E., Theohari, C., 1986. Steady wind pressures on solar collectors on flat-roofed buildings Journal of Wind Engineering and Industrial Aerodynamics 23, 249-258.

Shademan, M., Barron, R. M., Balachandar, R., Hangan, H., 2014. Numerical simulation of wind loading on ground-mounted solar panels at different flow configurations. Canadian Journal of Civil Engineering 41, 728-738.

Spalart, P. R., Jou, W-H., Strelets, M., Allmaras, S. R., 1997. Comments on the feasibility of LES for wings, and on a hybrid RANS/LES approach, First AFOSR International Conference on DNS/LES, Ruston, LA, 4–8 August. In Advances in DNS=LES, Liu C, Liu Z (eds). Greyden Press: Columbus, OH, 1997.

Stathopoulos, T., Zisis, I., Xypnitou, E., 2014. Local and overall wind pressure and force coefficients for solar panels. Journal of Wind Engineering and Industrial Aerodynamics 125, 195-206.

Warsido, W. P., Bitsuamlak, G. T., Barata, J., 2014. Influence of spacing parameters on the wind loading of solar array. Journal of Fluids and Structures 48, 295-315.

Wilcox, D. C., 1998. Turbulence modelling for CFD. DCW Industries, Inc., La Canada, California.

Wood, G. S., Denoon, R. O., Kwok, K. C. S., 2001. Wind loads on industrial solar panel arrays and supporting roof structure. Wind and Structures 4, 481-494.

Wu, Z., Gong, B., Wang, Z., Li, Z., Zang, C., 2010. An experimental and numerical study of the gap effect on wind load on heliostat. Renewable Energy 35, 797-806.

Yang, W., Quan, Y., Jin, X., Tamura, Y., Gu, M., 2008. Influences of equilibrium atmosphere boundary layer and turbulence parameter on wind loads of low-rise buildings. Journal of Wind Engineering and Industrial Aerodynamics 96, 2080-2092.

Yang, Y., Gu, M., Chen, S., Jin, X., 2009 a. New inflow boundary conditions for modelling the neutral equilibrium atmospheric boundary layer in computational wind engineering. Journal of Wind Engineering and Industrial Aerodynamics 97, 88-95.

Yang, Y., Gu, M., Jin, X., 2009 b. New inflow boundary conditions for modelling the neutral equilibrium atmospheric boundary layer in SST k-ω model. The Seventh Asia Pacific Conference on Wind Engineering, Taipei, Taiwan, November 8-12.

Yu, Y, 2012. Numerical simulation of wind load on roof mounted solar panels. Electronic Theses and Dissertations, Paper 218, University of Windsor, Canada.

Chapter 3

Experimental analysis of wind flow around a ground mounted stand-alone solar panel

3.1 Introduction

Over the last decade, solar photovoltaic (PV) panels have gained a lot of interests and become the fastest growing in terms of installed capacity among all the renewable energy sources. According to REN 21 (2014), “Almost half of all PV capacity in operation was added in the past two years, and 98% has been installed since the beginning of 2004.” Solar PV panels can be installed either on the roof or on the ground. Roof mounted PV panel, either flush mounted on a pitched roof or mounted at an angle on a flat roof, has always been very popular among home and small industry owners since it does not require any additional space and usually takes lower installation time and cost than the ground mounted system. However, there are some critical issues associated with roof mounted PV systems, such as the complex flow generated by the building which is responsible for complex loading patterns as well as loads on the roof due to the system’s weight. Wind loads on roof mounted PV systems have been studied extensively by various researchers (Radu et al., 1986; Radu and Axinte, 1989; Wood et al., 2001; Kopp et al., 2002; Chung et al., 2008; 2011; Meroney and Neft, 2010; Kopp et al., 2012; Kopp and Banks, 2013; Pratt and Kopp, 2013; Banks, 2013; Browne et al., 2013; Cao et al., 2013; Aly and Bitsuamlak, 2014; Stathopoulos et al., 2014; Warsido et al., 2014). Ground mounted solar panels have several advantages over roof mounted systems, such as, being not dependent on roof pitch and orientation, no space limitation, prone to more air circulation around the panel which keeps the panel cooler, easier maintenance and cleaning. All these advantages resulted in a growing trend in the installed PV capacity using ground mounted systems, especially at the utility scale. Utility scale solar plant employs arrays of ground mounted PV panels in an open field. Published literatures on the ground mounted solar panels, either stand-alone or array configuration, have dealt with wind loading on the panel and effect of different geometric parameters (scaling, wind direction, array spacing and ground clearance) on the loading (Bitsuamlak et al., 2010; Abiola-Ogedengbe, 2013; Aly and Bitsuamlak, 2013; Shademan et al., 2014 a,b; Jubayer and Hangan, 2014). Although wind loads on the solar panel are directly correlated with the wind flow field surrounding the panel, very few studies have focused on the wind flow field around the solar panel using experimental technique. Pratt and Kopp (2013) investigated the aerodynamic mechanisms associated with peak loads using synchronized time resolved particle image Velocimetry (PIV) and pressure measurements on the same roof mounted solar arrays used by Kopp et al. (2012). For the 20^o solar panel tilt angle, large vertical gusts were responsible for the peak uplift for 180^o wind direction, whereas for 0^o wind direction, the peak uplifts were associated with the streamwise gusts.

Abiola-Ogedengbe (2013) performed PIV measurements on a ground mounted solar panel and measured wind profiles only for 0^o incoming wind direction and also only at the windward side of the panel. Here, 0^o wind direction represents the incoming wind flow being normal to the solar panel span with the upper surface facing the wind, commonly also known as “the Southern wind”. Using Detached Eddy Simulation (DES) technique, Shademan et al. (2014b) analyzed the effect of ground clearance on the wake structure of a ground mounted stand-alone solar panel with tilt angle of 45^o. It was found that the Strouhal number increased with the increase in ground clearance. Also, irregular vortex shedding was observed for the smallest ground clearance.

The current study has been undertaken to investigate the aerodynamic mechanisms of the flow around a ground mounted solar panel subjected to the atmospheric boundary layer (ABL) flow under varying wind directions (0^o, 45^o, 135^o and 180^o) using particle image velocimetry (PIV) technique. Hot wire anemometry (HWA) is also used in the wake of the solar panel to detect the shedding of vortices. Another purpose of the present study is to provide a benchmark for validating numerical models for flows around ground mounted solar panels.

3.2 Experimental details

3.2.1 Wind tunnel and the solar panel model

The experiment was performed at the Boundary Layer Wind Tunnel I (BLWT I) at Western University, Canada. The tunnel is an open circuit type and has the cross-section of 2.4 m (width) × 2.15 m (height) at the test section with a length of 33 m. The wind tunnel is equipped with pneumatic controlled roughness elements as well as spires and trips to generate the required boundary layer profiles. The full scale stand-alone solar panel has the dimension of 2.48 m (B) × 7.29 m (W) × 1.65 m (H) with 25^o inclination (Fig. 3.1). Also, the distance between two side by side support legs is 3 m. A 1:10 geometric scale model of the solar panel was used for this experiment to obtain results with higher resolution. Although using such a large model is not conventional for the boundary layer wind tunnel, different researchers have used large models for small structures (Kopp et al., 2005; Suaris and Irwin, 2010; Visscher and Kopp, 2007; Aly and Bitsuamlak, 2013; Warsido et al., 2014). One of the solutions mentioned in Warsido et al. (2014) to test large scale models, is to match the lowest portion (4H from the tunnel floor) of the ABL at this large scale. The model was painted with matte black spray paint to reduce Laser reflection. The maximum blockage (for 0^o and 180^o wind direction) was found to be 1.63%.

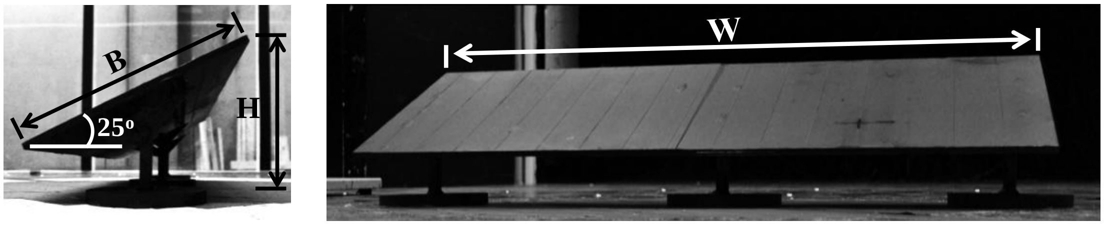

Figure 3.1: Experimental model of the solar panel.

3.2.2 Instrumentation and measurements

3.2.2.1 Particle Image Velocimetry

A Laser from Litron Lasers (Model: Nano L 50-100 PIV), which is a water cooled Nd:YAG (Class 4) compact dual head Laser, with output energy of 200 mJ at 532 nm wavelength for each Laser, was used. The repetition rate was set at 80 Hz (maximum repetition rate: 100 Hz) for each Laser head to avoid damage to the Laser and the power supply as the voltage measured in the wind tunnel lab was around 205V. The diameter of the Laser beam was 4 mm. A mirror and a cylindrical lens were used to change the direction of the Laser beam and to create a Laser sheet from the beam respectively. The camera used in this study had 4 Megapixel image resolutions with 2052 × 2048 pixel and was based on CMOS image sensors (Flare 4M180MCL, IO Industries). The camera was connected to a digital video recorder (Core DVR Express, IO Industries) and was controlled by a DVR software package CoreView (IO Industries). A digital pulse delay generator, Model 555 (Berkeley Nucleonics Corporation), was used to generate timing signals for the Laser and also to synchronize the camera exposures with individual Laser pulses. During the experiment, the flow was seeded with olive oil particles. The particles were generated using two Laskin nozzle type particle generators. These generators use compressed air to create a uniform mixture of air and olive oil droplets. Flexible plastic tubes were used to carry the particles in the tunnel.

In this study, a total of four incoming wind directions (0^o, 45^o, 135^o and 180^o, see Fig. 3.2 for the wind direction convention) were considered. Figure 3.3 shows a schematic of the

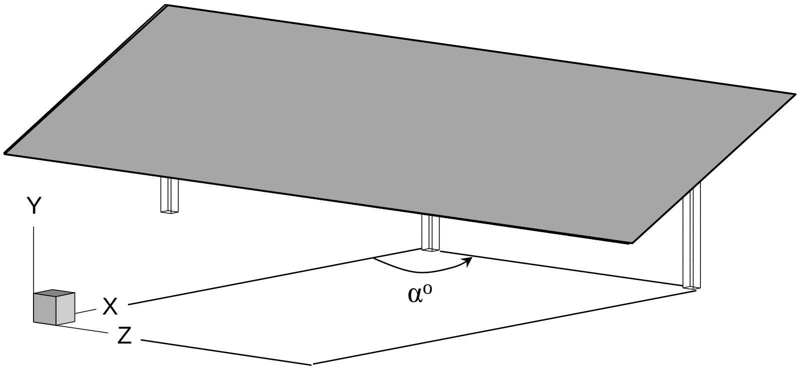

Figure 3.2: Wind direction (α^o).

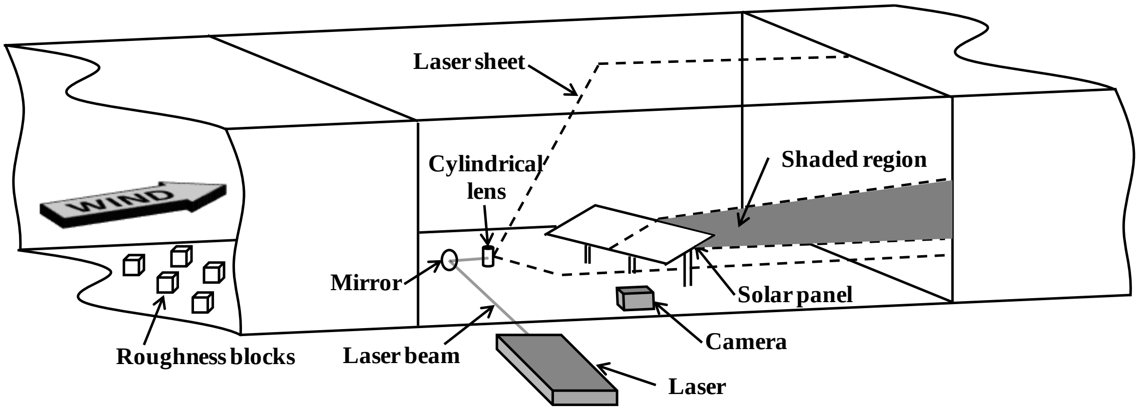

Figure 3.3: Schematic of the experimental setup (not to scale).

experimental setup in the wind tunnel for the 0^o wind direction case. Measurements were performed at two different planes for 0^o and 180^o wind directions (Fig. 3.4 a), one between two consecutive support legs of the panel (Plane 1) and the other close (at a distance of approx. W/100) to the middle support leg (Plane 2) in order to investigate the effects of the support leg. Measurements right at the middle support leg were avoided since the leg would create a shadow at the back. On the other hand, for the 45^o and 135^o wind directions, measurements were taken at a plane through the panel center and parallel to the side walls of the wind tunnel (Plane 3) (Fig. 3.4 b). In each plane, measurements

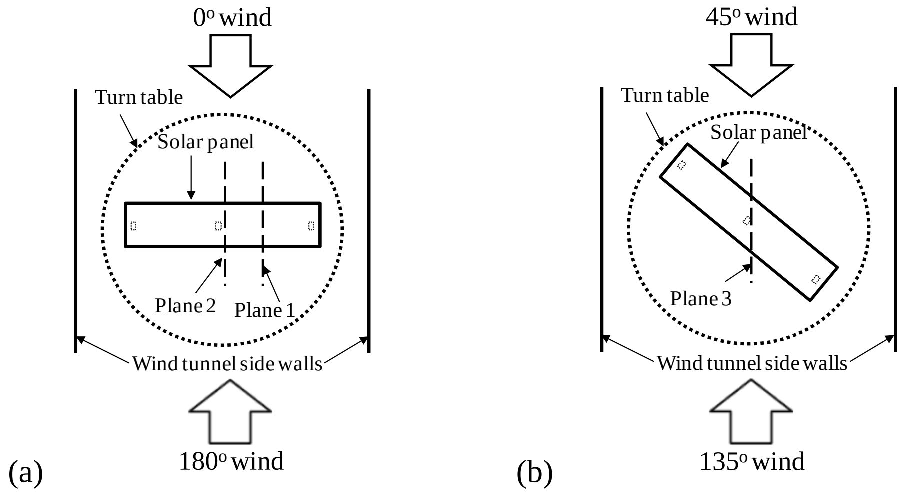

Figure 3.4: Schematics of the measurement planes in a plan-view (not to scale) for (a) 0° and 180° and (b) 45° and 135° wind directions.

were taken at 3 to 4 frames of size 18 cm × 18 cm each in order to capture the wind flow field around the solar panel. For the windward frames (black dashed lines, Fig. 3.5), the Laser was shot from upstream of the solar panel, whereas for the leeward frames (grey dash dotted lines, Fig. 3.5), the Laser was moved back and shot from a downstream location. Two olive oil seeders were used to seed the wind tunnel. The seeders were place outside the tunnel with flexible plastic tube (25 mm diameter) running into the tunnel carrying the olive oil smoke. Both tube outlets were placed upstream of the solar panel with one being closer than the other. However, the distances of the tube outlets were varied from one field of view to another to obtain uniform seeding in an image. Also, a small PVC pipe (length of around 300 mm and diameter of 19 mm) with several holes (similar to a flute) was attached to the each tube outlet to obtain a uniform distribution of the olive oil particles. The tubes were laid flat on the tunnel floor near the roughness block set closest to the model panel. Since the diameters of the tubes (25 mm and 19 mm) were much less than the heights of the roughness blocks (127 mm), the effect of this tube on the flow was assumed to be negligible. During the experiment, images were captured at a rate of 56 fps for 1 minute for each frame, which resulted in about 1680 image pairs. The time interval between two consecutive images was 180 μs. Uncertainty analysis of the PIV experiment was performed based on Cowen and Monismith (1997) and the error was found to be 2.4% of the mean wind speed at height H ($\overline{U_H}$) (Appendix D).

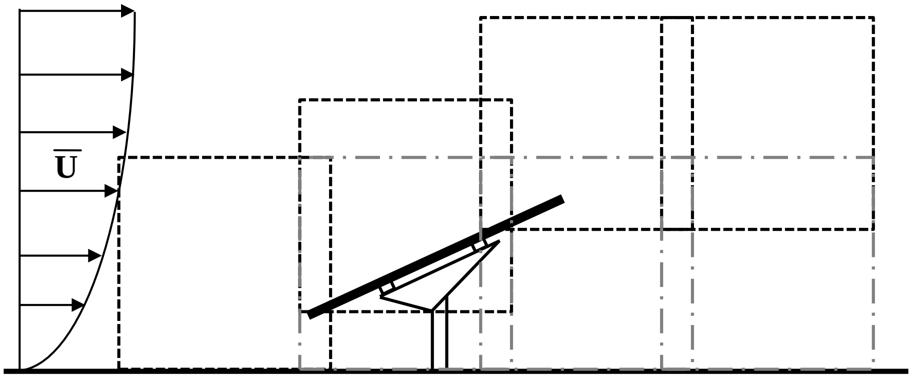

Figure 3.5: Location of measurement frames on a plane (for 0^o wind direction). Dashed line (black) represents when the laser was upstream and dash-dotted (grey) when the laser was downstream of the solar panel.

To obtain the raw velocity from an image pair, commercial image processing software heurisko® (AEON Verlag & Studio GmbH & Co. KG) was employed. It uses FFT cross correlation method to get the displacement of a particle in an interrogation window. The size of the interrogation windows were 32 × 32 pixels with 50% overlap. A sample instantaneous image is shown in Figure 3.6 (a). To get rid of the vectors in the shaded region, within the solid body and also the regions with high Laser reflection, a binary image was created for masking (Fig. 3.6 b). The vectors in the white areas in Fig. 3.6 b were assigned as NaN (not-a-number), whereas, in the black region, spurious vectors were identified with statistical median and global outliners filters (Siddiqui et al., 2001) and were replaced by the local median vector. The corrected vectors with the binary image masking are shown in Figure 3.6 c. Finally, a MATLAB (The MathWorks, Inc.) script was used for converting pixel displacements to velocities (m/s) and also for calculating the flow statistics. Patching of the frames was done using a global co-ordinate system where the origin was on the tunnel floor at the horizontal location of the lower edge of the panel. During patching, averaging was performed between two frames in the overlapped region (Hashemi Tari, 2012).

(a) (b) (c)

Figure 3.6: Image processing steps (a) raw image (b) masking image and (c) corrected vectors (only every 5th vectors are shown here).

3.2.2.2 Hot Wire Anemometry

A cross (X) sensor hot-wire probe (55P61) from Dantec Dynamics was used for vortex shedding detection for the 0° and 180° wind direction cases. A constant temperature anemometer (CTA) system, also from Dantec Dynamics, was employed with a multichannel (4 channels) system (54N82) with bandwidths of ~ 10kHz at 50 m/s.

How Wire Anemometry (HWA) was employed to obtain wind profiles in the empty wind tunnel and also to detect vortex shedding in the wake of the solar panel. PIV was not employed to detect the vortex shedding as the PIV sampling frequency of 28Hz (Nyquist frequency of 14Hz) might not be enough to detect vortex shedding in the flow. For the wind tunnel profiles, measurements were performed at the turn table center at various heights from Y/H = 0.2 to 6.0 (see Fig. 3.2 for the co-ordinate system) with higher spatial resolution close to the tunnel floor. Measurements for vortex shedding were performed for the 0^o and 180^o wind directions only. For the vortex shedding measurement, the X-wire probe was placed in Plane 1 (Fig. 3.4 a) at X/H = 3.8 from the lower edge. The probe was moved vertically using the BLWT traverse system to 12 different heights from Y/H = 0.2 to 3.0 to obtain the most distinguishable peak in the power spectrum analysis. Samples were taken at 1 kHz for 30s for both tunnel profiles and vortex shedding measurements. For an inclined flat plate with tilt angle of 25^o in a low turbulent uniform flow, Strouhal number, St ($St = fh/\overline{U_H}$, here f is the frequency (Hz), h is the vertical projection of the inclined surface of the panel (m), $\overline{U_H}$ is the mean streamwise wind velocity at height H (m/s)) of around 0.2 is reported by Fage and Johansen (1927) and Chen and Fang (1996). Based on St of 0.2, sampling frequency was about 100 times the vortex shedding frequency and the sample time was long enough to capture about 300 vortex shedding cycles (Borchers et al., 1996; Miau et al., 1997; Mills et al., 2002). The uncertainty of a velocity sample for the HWA system used in this study is about 5% with a confidence interval of 95% based on Wheeler and Ganji (2003) and the Dantec User Guide (9040U6163) (Appendix E).

3.2.3 Boundary layer simulation

The target profiles for this study were the ESDU ABL profiles (ESDU 1974, 1982, 1983) for open terrain roughness (aerodynamic roughness length, y_0 of 0.03 m). Before going into the wind tunnel for the measurement, previously acquired wind profiles in the BLWT I for different roughness from the BLWT database, were compared with the target ESDU profiles to best match the wind profiles at 1:10 geometric scale. The chosen profile from the BLWT database was then employed during the experiment. However, to ensure that the expected profile was simulated correctly, measurements were performed inside the empty wind tunnel using HWA. Figure 3.7 shows the final velocity and turbulence intensity profiles measured using HWA along with the target ESDU profiles. In Figure 3.7, the heights are normalized with H and the wind velocities are normalized with the mean streamwise velocity at height H, $\overline{U_H}$. The agreement of the normalized mean velocity and turbulence intensity profiles between empty wind tunnel measurement and ESDU is satisfactory. Wind spectra of streamwise and vertical velocity components measured at height H from the tunnel floor along with the target ESDU spectra are shown in Figure 3.8. As can be seen from Figure 3.8, the measured spectra are shifted, towards high frequency for streamwise velocity and lower frequency for vertical velocity, compared to the ESDU spectra. From Figure 3.8 (a), it can be said that the large scale or low frequency turbulence were not simulated properly. These large scales turbulence are found to be at least an order of magnitude larger compared to the solar panel breadth (B).

Similar observation was reported by Aly and Bitsuamlak (2013) when large scale (1:10 and 1:5) ABL flows were simulated in the wind tunnel. In this experiment, Reynolds number based on the wind speed at height H, breadth of the panel (B) and the air properties at 20°C, was 8.3×10^4.

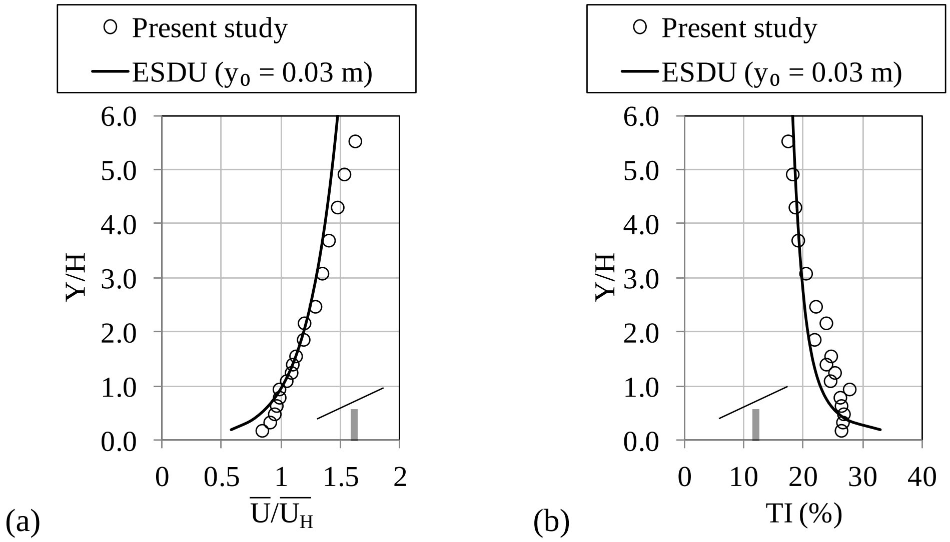

Figure 3.7: (a) Mean velocity and (b) Turbulence Intensity (TI) profiles in the wind tunnel.

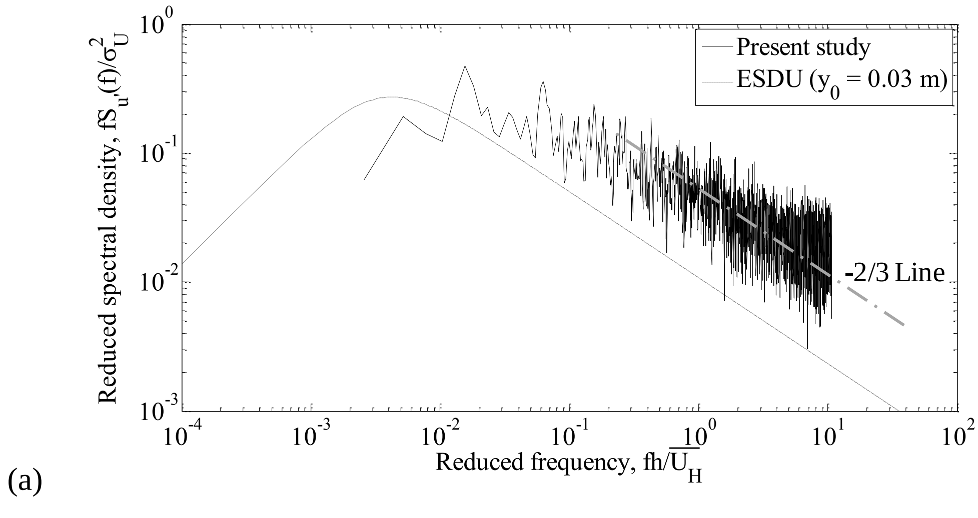

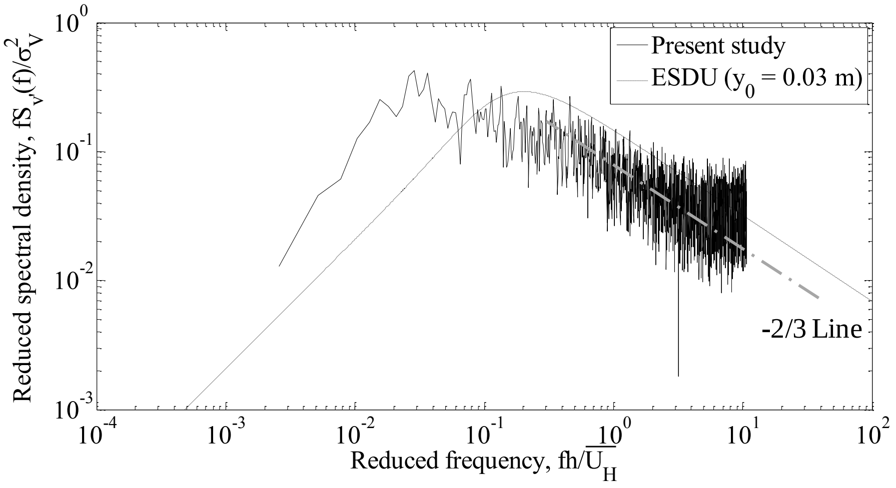

(b)

Figure 3.8: Spectra of the (a) streamwise and (b) vertical velocity fluctuations at the solar panel height, H.

3.3 Results and discussion

The mean velocity contours and streamlines are first analyzed to describe the overall mean flow structures around the solar panel. Profiles of mean streamwise and vertical velocity components around the solar panel are also reported. Turbulent characteristics of the flow are evaluated by plotting the Reynolds normal and shear stress profiles. At the end of this section, characteristics of the vortex shedding in the wake of the solar panel are discussed.

3.3.1 Mean velocity field

Normalized mean velocity magnitude contours along with streamlines around the solar panel for all wind directions are shown in Figure 3.9. Distances are normalized by the panel height, H and wind speeds are normalized by the mean wind speed at height H in the undisturbed flow ($\overline{U_H}$). For 0^o wind direction at both Plane 1 (Fig. 3.9 a) and Plane 2 (Fig. 3.9 b), the wind flow remains attached on the upper surface of the panel and accelerates towards the trailing edge of the panel. A separation bubble is formed on the leeward side of the panel. In Plane 1 (Fig. 3.9 a), one big separation bubble is observed whereas in Plane 2, the support leg breaks the bubble into two vortices, both rotating counter clockwise. Qualitatively, for 0^o wind direction, the mean wind speeds on the upper surface of the solar panel between Plane 1 and 2 are very similar, however on the leeward side, a decrease in mean velocity is observed in Plane 2 downstream of the support leg. This is due to the support leg being very close to the measurement Plane 1 and thus affecting the flow downstream of the support leg. For 180^o wind direction, the flow separates at the leading edge and forms a separation bubble rotating clockwise on the upper surface of the panel in both Plane 1 and 2 (Fig. 3.9 c,d). However, in Plane 2 (Fig. 3.9 d), a small counter clockwise rotating vortex from the trailing edge of the panel is seen which is not evident in Plane 1 (Fig. 3.9 c). The counter clockwise rotating vortex from the trailing edge in Plane 2 could be due to the higher disturbances in the flow underneath the panel created by the support leg or higher suction in the separation bubble from the leading edge compared to Plane 1 that triggered the vortex from the trailing edge. For the oblique wind directions (45^o and 135^o), flow fields on the windward and leeward sides of the panel are shown separately for better visualization of the results (Figure 3.9 e-h). Due to the higher Laser reflection from the tilted orientation of the solar panel, more data is lost in the oblique wind direction cases (45^o and 135^o) compared to the straight wind directions (0^o and 180^o). For 45^o wind direction, attached flow is observed on the windward surface of the solar panel (Fig. 3.9 e) followed by flow separation at the leading edge towards the leeward surface of the panel without any vortex formation being seen (Fig. 3.9 f). On the other hand, for 135^o wind direction, the flow separates and reattaches on the upper surface of the panel (Fig. 3.9 g). Although for the same solar panel model, existence of corner vortices is reported based on a CFD study performed by Jubayer and Hangan (2014), comments could not be made on the existence of corner vortices on the leeward surface of the panel for oblique wind directions from Figures 3.9 f and 3.9 g for the current study. Centers of vortices on the leeward side of the solar panel for 0^o and 180^o wind direction as well as sizes of vortices are reported in Table 3.1. Centers of vortices are presented using the same co-ordinate system employed in Figure 3.9 and sizes of vortices are presented in terms of distance normal to the panel surface (d) normalized with H. For both 0^o and 180^o wind directions, a larger separation bubble is observed in Plane 2 compared to Plane 1. The mean velocity profiles around the solar panel for all four wind directions (0^o, 45^o, 135^o and 180^o) from all three measurement planes are shown in Figure 3.10. Mean streamwise ($\overline{U}$) and vertical ($\overline{V}$) velocity components normalized with $\overline{U_H}$ are plotted along 13 vertical lines among which 9 profiles are at B′/8 distance intervals from the leading edge to the trailing edge of the solar panel and 2 profiles are at B′/4 distance interval on each upstream and downstream side of the solar panel. Here, B′ is the panel breadth in the respective measurement plane for each wind direction. For 0^o and 180^o wind directions, profiles from Plane 1 and 2 are plotted in the same figure for comparison (Fig. 3.10 a-d).

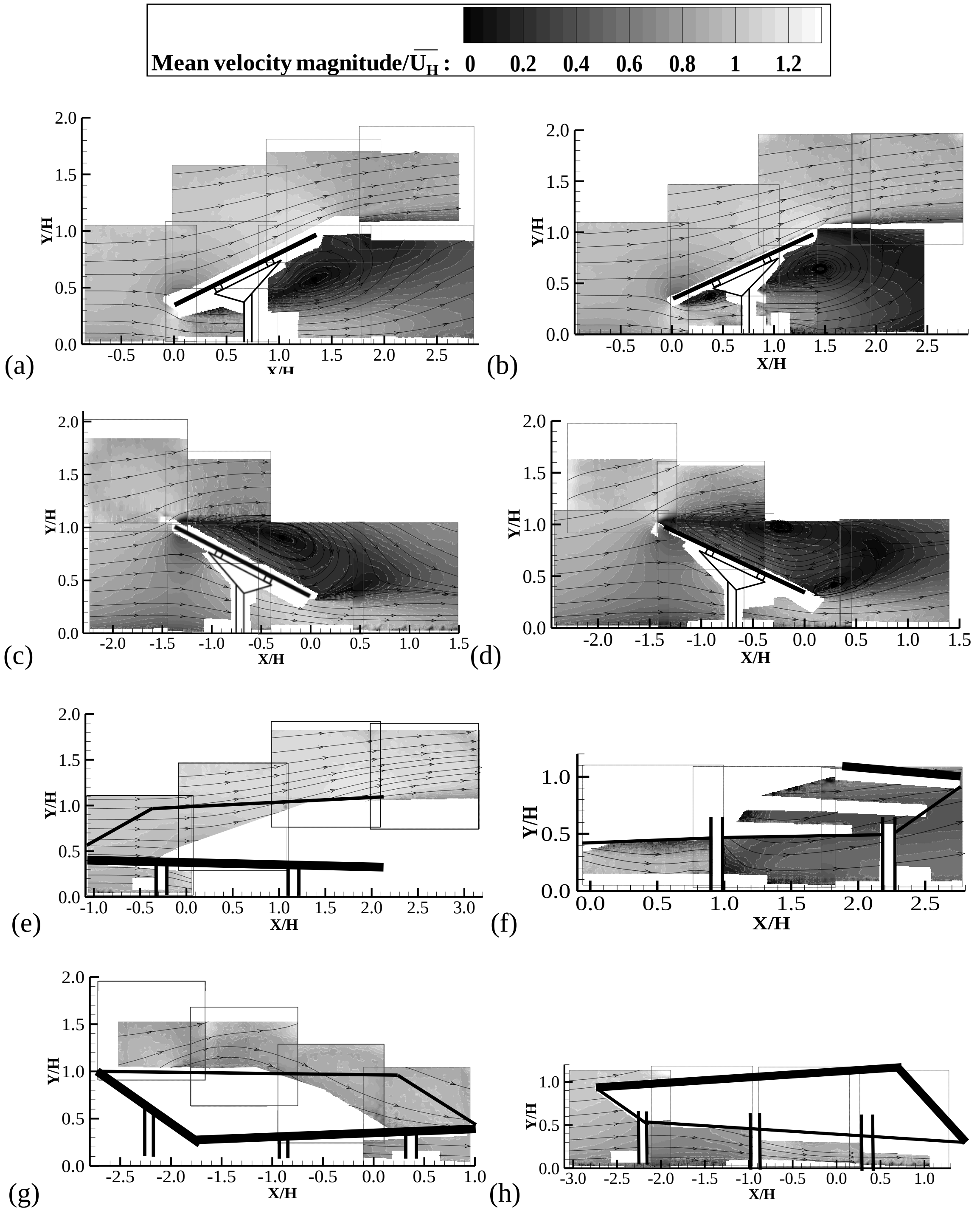

Figure 3.9: Normalized mean velocity contours with superimposed streamlines for (a) α = 0^o, Plane 1, (b) α = 0^o, Plane 2, (c) α = 180^o, Plane 1, (d) α = 180^o, Plane 2, (e) α = 45^o, Plane 3, windward, (f) α = 45^o, Plane 3, leeward, (g) α = 135^o, Plane 3, leeward, (h) α = 135^o, Plane 3, windward.

Table 3.1: Location of the center of vortices and thickness of vortices.

	Wind direction					
	0°			180°		
	Plane 1	Plane 2		Plane 1	Plane 2	
		Big vortex	Small Vortex		Big vortex	Small Vortex
Center, (X/H, Y/H)	(1.35, 0.57)	(1.45, 0.65)	(0.38, 0.38)	(-0.28, 0.90)	(-0.25, 0.98)	(0.27, 0.42)
Size, d/H	0.58	0.63	0.24	0.63	0.68	0.36

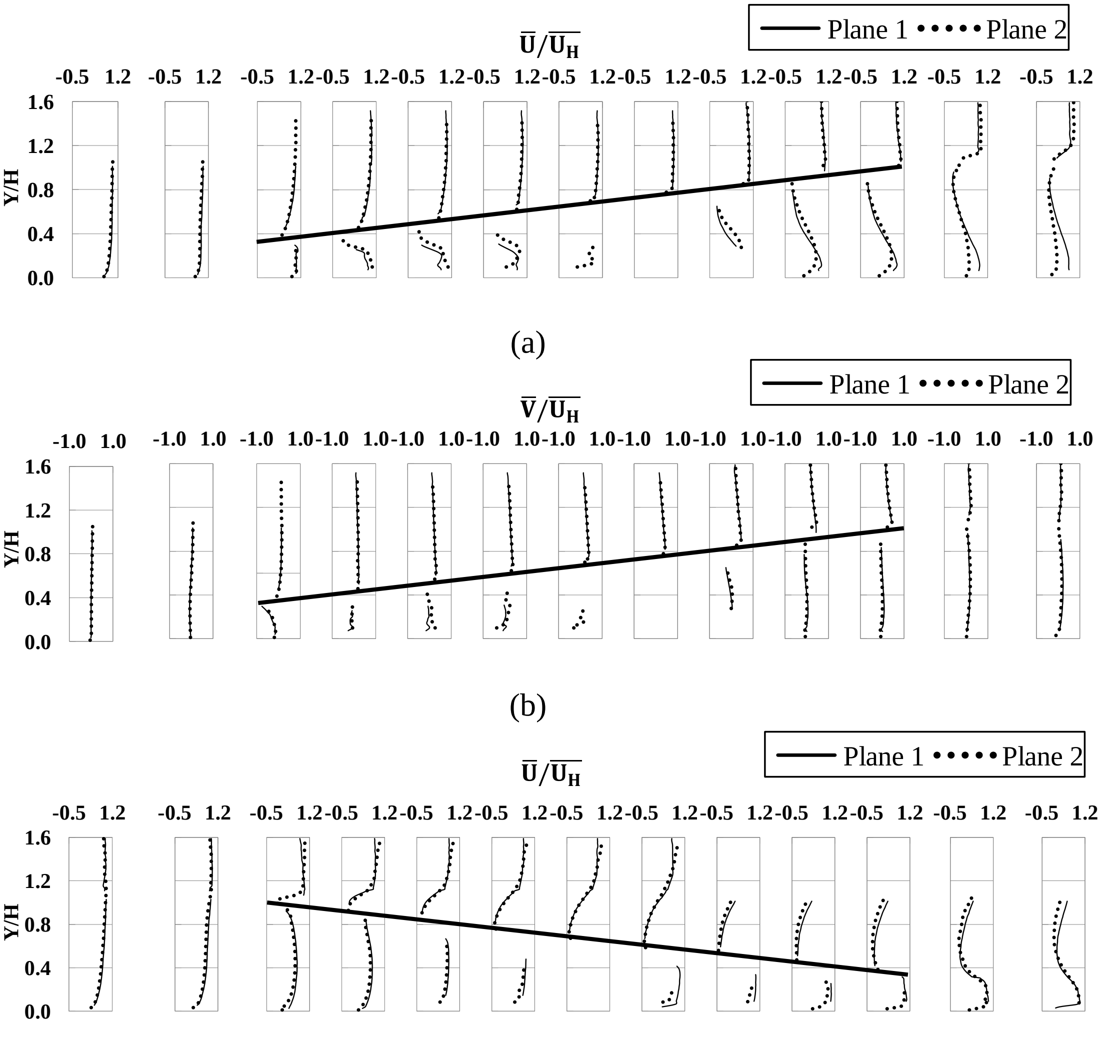

(a)

(b)

(c)

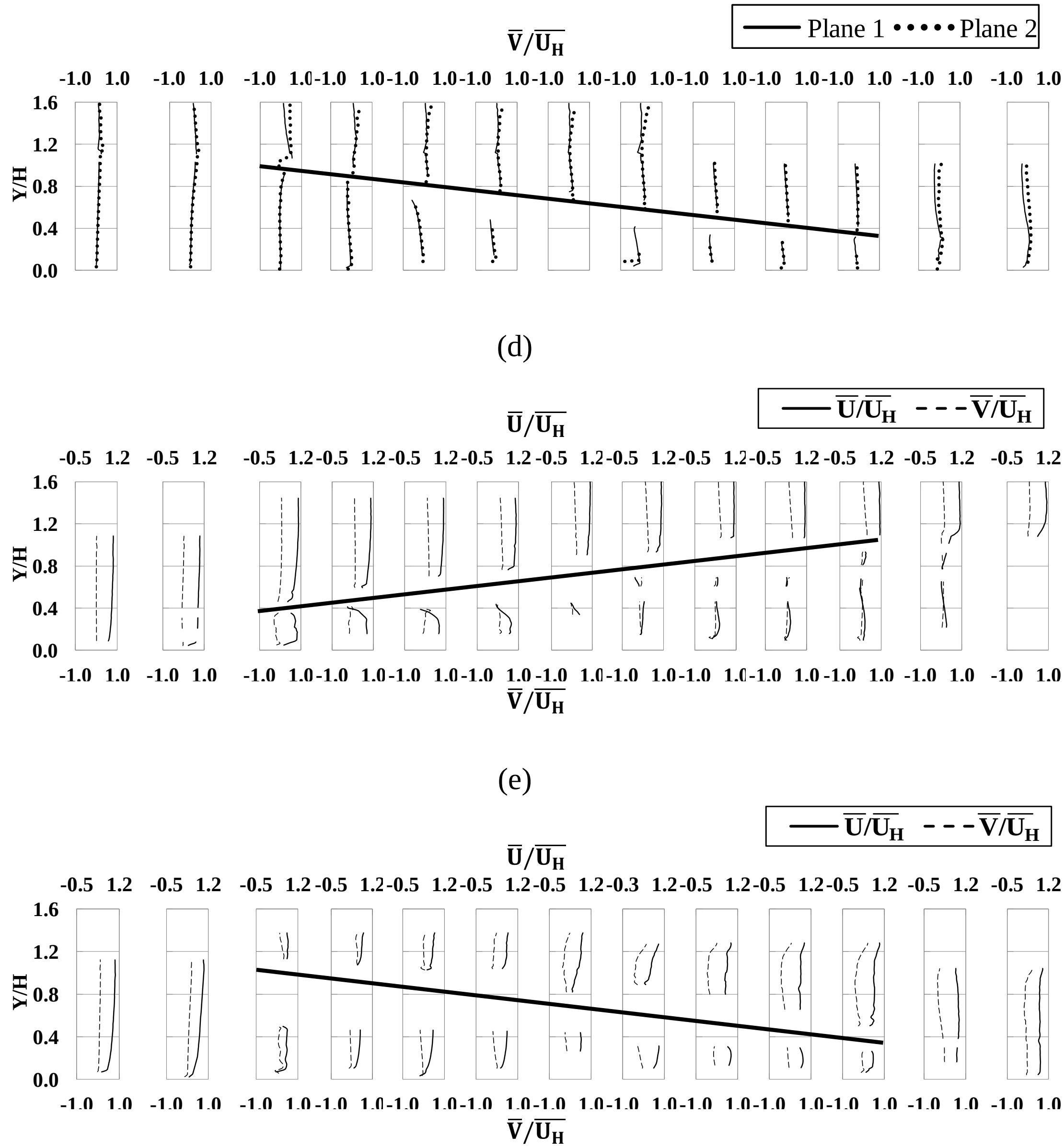

(d)

(e)

(f)

Figure 3.10: Normalized velocity profiles for (a) α = 0°, streamwise, (b) α = 0°, vertical, (c) α = 180°, streamwise, (d) α = 180°, vertical, (e) α = 45°, streamwise and vertical, (f) α = 135°, streamwise and vertical velocity components.

For 0^{o} wind direction, streamwise velocities from Plane 1 and 2 are in close agreement except in the wake and underneath the panel downstream of the support leg (Fig. 3.10 a). In the wake, the streamwise velocity in the wake is lower in Plane 2 compared to Plane 1. With the exception at the locations in the vicinity of the support leg, the vertical velocity components match well between Plane 1 and 2. On the other hand for 180^{o} wind direction, the fact that the measurement plane is in close proximity to the support leg has an effect on both streamwise and vertical velocity components on the leeward side of the panel and also in the wake of the panel (Fig. 3.10 c,d). For 0^{o} wind direction, the maximum mean wind speed (~ $1.1\overline{U_H}$) is observed right above the trailing edge and underneath the leading edge of the panel. For 180^{o} wind direction, the maximum wind speed is found underneath the trailing edge. Since for the oblique wind directions (45^{o} and 135^{o}) the measurements are performed at a single plane (Plane 3), both streamwise and vertical velocity components are plotted in the same figure (Fig. 3.10 e,f). Among all four wind directions studied herein, the maximum wind speed is found for the 45^{o} wind direction right above the trailing edge. For 135^{o} wind direction, the streamwise velocity profile in the wake is almost uniform, compared to the other three wind directions. This might be an indication that the flow recovery is faster for 135^{o} compared to the other three wind directions. Due to the lack of data close to the surface of the solar panel, vortices on the leeward side of the panel at the oblique wind directions have not been identified.

3.3.2 Reynolds normal and shear stresses

To investigate the turbulent characteristics of the flow, vertical profiles of Reynolds normal ($\overline{u'u'}$, $\overline{v'v'}$) and shear stress components ($\overline{u'v'}$) normalized with $\overline{U_H}^2$ are presented in Figure 3.11. Locations of the profiles are same as in the previous section. For 0^o and 180^o wind direction, results only from Plane 1 are plotted as Plane 1 and 2 show similar distributions. For 0^o wind direction, a gradual increase in the stresses are observed on the upper surface of the solar panel from the leading edge to the trailing edge and then into the wake. Underneath the panel close to the trailing edge, higher velocity fluctuations are observed (Fig. 3.11 a). For 180^o wind direction, turbulence is significantly higher on the leeward side of the panel than the windward side (Fig. 3.11 b). Except close to the leading edge, a pattern is observed in the shear stress profiles on the leeward side of the panel: shear stresses are around zero close to the panel surface, decrease to a minimum value while moving upwards and then increase again. This pattern is usually found in a shear layer bounding a closed reversed flow region (i.e., the separation bubble) (Ruderich and Fernholz, 1986). Turbulence level for the 45^o wind direction is similar to the 0^o wind direction case, with gradual increase of the stresses from the leading edge to the trailing edge on the windward surface of the panel and significantly higher turbulence underneath the panel close to the leading edge than on the upper surface (Fig. 3.11 c). For 135^o wind direction, turbulence is very low on the windward side of the panel (Fig. 3.11 d). However, on the leeward side, Reynolds normal and shear stress components are as high as in 180^o wind direction case. Overall, the highest levels of turbulence are observed on the leeward side for the 135^o and 180^o wind direction cases.

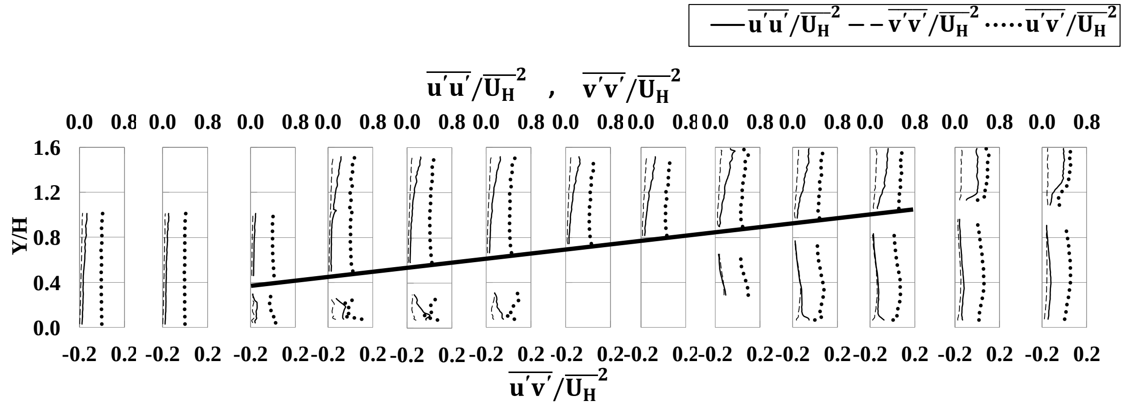
$\overline{u'u'}/\overline{U_H}^2$
$\overline{v'v'}/\overline{U_H}^2$
$\overline{u'v'}/\overline{U_H}^2$
$\overline{u'u'}/\overline{U_H}^2$, $\overline{v'v'}/\overline{U_H}^2$
0.0
0.8
1.6
1.2
Y/H
0.8
0.4
0.0
-0.2
0.2
$\overline{u'v'}/\overline{U_H}^2$

(a)

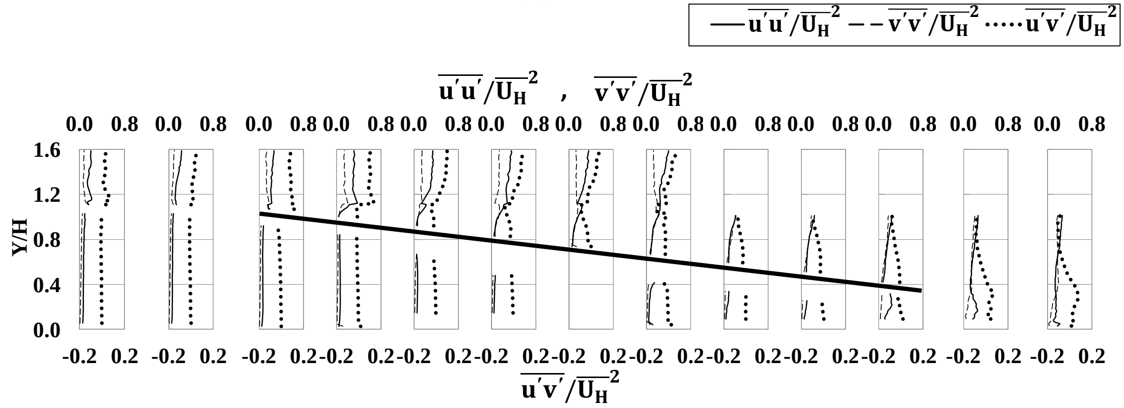
$\overline{u'u'}/\overline{U_H}^2$
$\overline{v'v'}/\overline{U_H}^2$
$\overline{u'v'}/\overline{U_H}^2$
$\overline{u'u'}/\overline{U_H}^2$, $\overline{v'v'}/\overline{U_H}^2$
0.0
0.8
1.6
1.2
Y/H
0.8
0.4
0.0
-0.2
0.2
$\overline{u'v'}/\overline{U_H}^2$

(b)

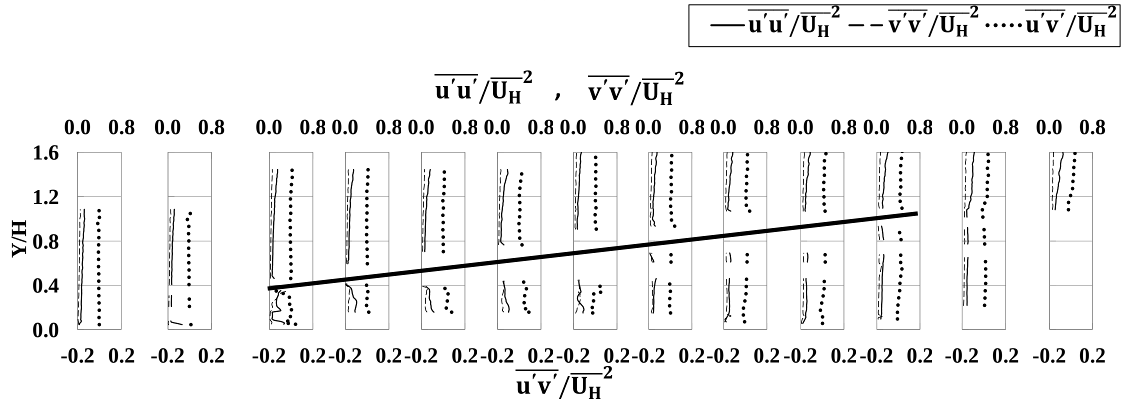
$\overline{u'u'}/\overline{U_H}^2$
$\overline{v'v'}/\overline{U_H}^2$
$\overline{u'v'}/\overline{U_H}^2$
$\overline{u'u'}/\overline{U_H}^2$, $\overline{v'v'}/\overline{U_H}^2$
0.0
0.8
1.6
1.2
Y/H
0.8
0.4
0.0
-0.2
0.2
$\overline{u'v'}/\overline{U_H}^2$

(c)

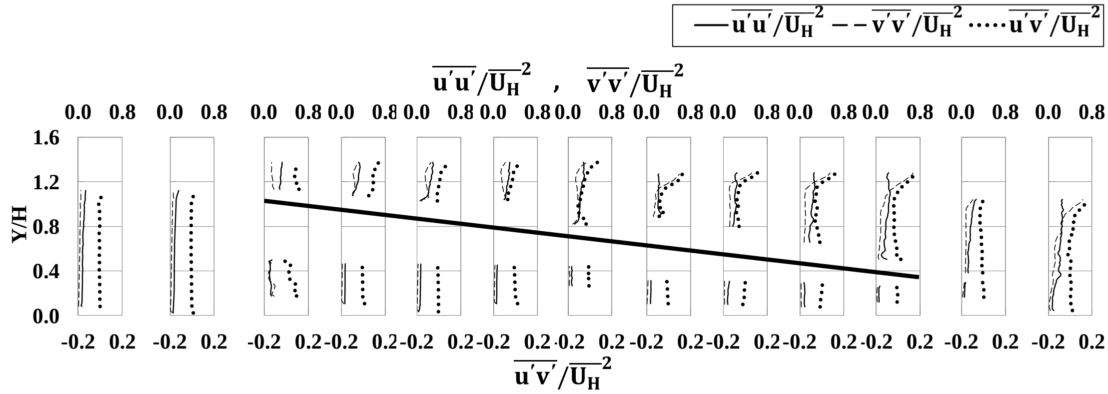

(d)

Figure 3.11: Reynolds normal and shear stress components for (a) α = 0^o, (b) α = 180^o, (c) α = 45^o and (d) α = 135^o.

3.3.3 Vortex shedding characteristics

To detect the shedding of vortices, power spectral densities of both the streamwise and vertical velocity fluctuations at locations described in 3.2.2.2 are analyzed. Vertical velocity fluctuations have shown a vague peak in the wind spectra only at Y/H = 1.14 and only for the 180^o wind direction (Fig. 3.12). From Figure 3.12, an approximate Strouhal number St = 0.2 can be inferred. For an inclined flat plate with tilt angle of 25^o in a low turbulent uniform flow, St of around 0.2 was reported by Fage and Johansen (1927) and Chen and Fang (1996). However, the vortex shedding observed herein is weak and is only detected only at the aforementioned location based on the spectra of the vertical velocity fluctuation. Gradient of the streamwise velocity component in the vertical direction (du/dy), normalized by $\overline{U_H}$/H is plotted to detect the location of the shear layer generated from the top edge of the solar panel. As can be seen from Figure 3.13, the

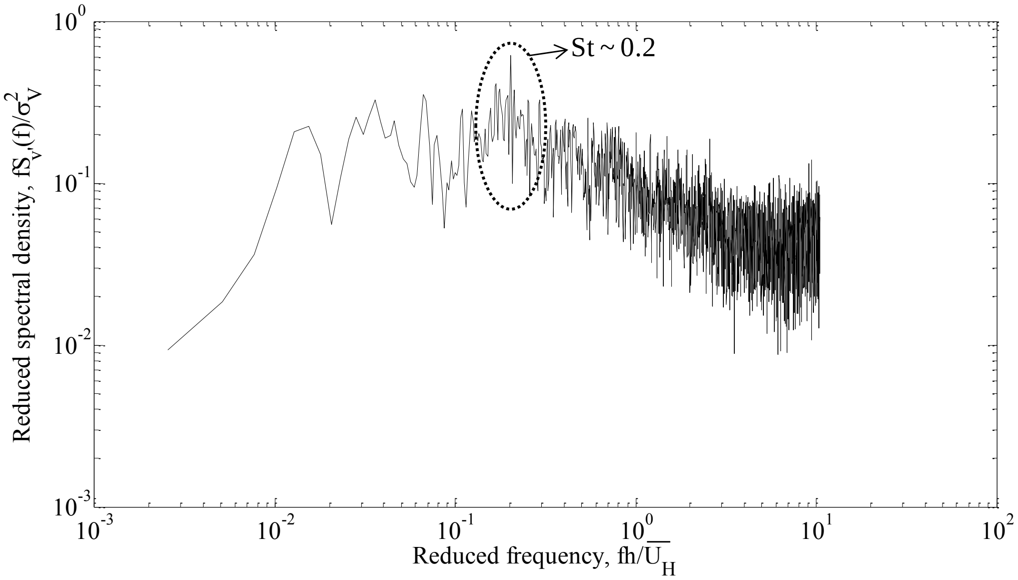

Figure 3.12: Spectra of the vertical velocity fluctuation at Y/H = 1.14.

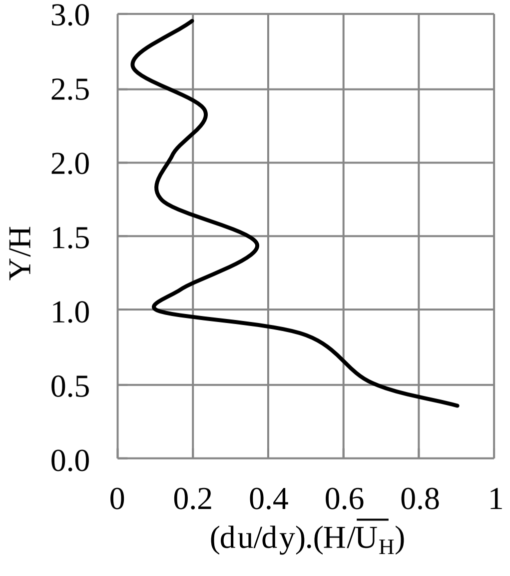

Figure 3.13: Streamwise velocity gradient at X/H = 3.8 at Plane 1.

position Y/H=1.14, at which the shedding of vortices is detected, is located close to the shear layer (Y/H ~ 1.5) from the top edge of solar panel. On the other hand, shedding of vortices could not be detected from the lower edge of the solar panel at 180° wind direction as well as from both upper and lower edges for 0° wind direction. It has been reported by Straatman and Martinuzzi (2002) and Shademan et al. (2014b) that the vortex shedding frequency reduces as the distance between a bluff body and a wall decreases. For the ground clearance used in this study (0.36H), dynamic loading due to the vortex shedding should not be an issue for 0° wind direction, whereas for 180° wind direction, unsteady forces due to the shedding of vortices from the top edge of the solar panel could be observed.

3.4 Conclusions

The present study has examined the wind flow field around a ground mounted stand-alone solar panel under two straight (0° and 180°) and two oblique (45° and 135°) wind directions using Particle Image Velocimetry (PIV) and Hot Wire Anemometry (HWA) techniques. The following conclusions can be drawn from this study:

- For the straight wind direction cases (0° and 180°) in a plane (Plane 1) between the panel's support legs, the flow separates at the leading edge and forms a large vortex on the leeward surface of the solar panel. In contrast, at the measurement plane close to the support leg (Plane 2), two separate vortices are observed.
- A full characterization of both streamwise and vertical velocity profiles on both surfaces is obtained for the four wind directions investigated.

- For the oblique wind direction (45^o and 135^o) cases, flow separation is detected from the leading edge but due to lack PIV data near the surface, the entire vortex extent on the leeward surface is not captured.
- For all wind directions, turbulence levels on leeward surfaces of the solar panel as well as in the wake are significantly higher than the windward surfaces. 135^o and 180^o wind direction cases have shown the highest level of velocity fluctuations on the leeward side of the panel.
- Weak vortex shedding is detected only for 180^o wind direction with a Strouhal number of approx. 0.2. The location, at which the vortex shedding is detected, is close to the shear layer generated by the leading edge of the solar panel. Shedding of vortices is not found for the 0^o wind direction case for this distance (gap) between the panel and the ground

The normalized mean velocity contours along with streamlines, mean streamwise and vertical velocity profiles around the solar panel as well as normal and shear stress profiles reported here can be used to validate other numerical and experimental studies on the ground mounted stand-alone panels both qualitatively and quantitatively.

References

Abiola-Ogedengbe, Ayodeji, 2013. Experimental investigation of wind effect on solar panels. University of Western Ontario - Electronic Thesis and Dissertation Repository**.** Paper 1177. http://ir.lib.uwo.ca/etd/1177.

Aly, A., Bitsuamlak, G., 2014. Wind induced pressures on solar panels mounted on residential homes. Journal of Architectural Engineering 20, 04013003.

Aly, A., Bitsuamlak, G., 2013. Aerodynamics of ground-mounted solar panels: Test model scale effects. Journal of Wind Engineering and Industrial Aerodynamics 123, 250-260.

Banks, D., 2013. The role of corner vortices in dictating peak wind loads on tilted flat solar panels mounted on large, flat roofs. Journal of Wind Engineering and Industrial Aerodynamics 123, 192-201.

Bitsuamlak, G. T., Dagnew, A. K., Erwin, J., 2010. Evaluation of wind loads on solar panel modules using CFD. The Fifth International Symposium on Computational Wind Engineering, Chapel Hill, North Carolina, USA, May 23-27.

Borchers, W., Domick, G., Kroner, D., Rautmann, R., Saupe, D., 1996. Visualization methods in high performance computing and flow simulation. 1st edition, VSP BV and TEV Ltd.

Browne, M. T. L., Gibbons, M. P. M., Gamble, S., Galsworthy, J., 2013. Wind loading on tilted roof-top solar arrays: The parapet effect. Journal of Wind Engineering and Industrial Aerodynamics 123, 202-213.

Cao, J., Yoshida, A., Saha, P., Tamura, Y., 2013. Wind loading characteristics of solar arrays mounted on flat roofs. Journal of Wind Engineering and Industrial Aerodynamics 123, 214-225.

Chen, J. M., Fang, Y-C., 1996. Strouhal number of inclined flat plates. Journal of Wind Engineering and Industrial Aerodynamics 61, 99-112.

Chung, K. M., Chang, K. C., Chou, C. C., 2011. Wind loads on residential and large-scale solar collector models. Journal of Wind Engineering and Industrial Aerodynamics 99, 59-64.

Chung, K., Chang, K., Liu, Y., 2008. Reduction of wind uplift of a solar collector model. Journal of Wind Engineering and Industrial Aerodynamics 96, 1294-1306.

ESDU, 1974. Characteristics of atmospheric turbulence near the ground, Data Unit Number 74031.

ESDU, 1982. Strong winds in the atmospheric boundary layer. Part 1: Mean hourly wind speeds. Engineering Science Data Unit Number 82026.

ESDU, 1983. Strong winds in the atmospheric boundary layer. Part 2: Discreet gust speeds. Engineering Science Data Unit Number 83045.

Fage, A., Johansen, F. C., 1927. On the flow of air behind an inclined flat plate of infinite span. Proceedings of the Royal Society of London. Series A, Containing Papers of a Mathematical and Physical Character 116, 170-197.

Hashemi Tari, Pooyan, 2012. Near-Wake Flow Dynamics of a Horizontal Axis Wind Turbine University of Western Ontario - Electronic Thesis and Dissertation Repository**.** Paper 1033.http://ir.lib.uwo.ca/etd/1033

Jubayer, C. M., Hangan, H., 2014. Numerical simulation of wind effects on a stand-alone ground mounted photovoltaic (PV) system. Journal of Wind Engineering and Industrial Aerodynamics 134, 56-64.

Kopp, G. A., Banks, D., 2013. Use of wind tunnel test method for obtaining design wind loads on roof-mounted solar arrays. Journal of Structural Engineering 139,284-287.

Kopp, G. A., Farquhar, S., Morrison, M. J., 2012. Aerodynamics mechanisms for wind loads on tilted, roof-mounted, solar arrays. Journal of Wind Engineering and Industrial Aerodynamics 111, 40-52.

Kopp, G.A., Surry, D., Mans, C., 2005. Wind effects of parapets on low buildings: part1. Basic aerodynamics and local loads. Journal of Wind Engineering and Industrial Aerodynamics 93, 817–841.

Kopp, G. A., Surry, D., Chen, K., 2002. Wind loads on a solar array. Wind and Structures 5, 393-406.

Meroney, R. N., Neft, D. E., 2010. Wind effects on roof-mounted solar photovoltaic arrays: CFD and wind-tunnel evaluation. The Fifth International Symposium on Computational Wind Engineering, Chapel Hill, North Carolina, USA.

Miau, J. J., Seu, T. S., Liu, T .W., Chou, J. H., 1997. On vortex shedding behind circular disk. Experiments in Fluids 23, 225-233.

Mills, R., Sheridan, J., Hourigan, K., 2002. Response of base suction and vortex shedding from rectangular prisms to transverse forcing. Journal of Fluid Mechanics 461, 25-49.

Pratt, R. N., and Kopp, G. A., 2013. Velocity measurements around low-profile, tilted, solar arrays mounted on large flat-roofs, for wall normal wind directions. Journal of Wind Engineering and Industrial Aerodynamics 123, 226-238.

Radu, A., Axinte, E., 1989. Wind forces on structures supporting solar collectors. Journal of Wind Engineering and Industrial Aerodynamics 32, 93-100.

Radu, A., Axinte, E., Theohari, C., 1986. Steady wind pressures on solar collectors on flat-roofed buildings Journal of Wind Engineering and Industrial Aerodynamics 23, 249-258.

REN 21, 2014. Renewables 2014 Global Status Report. REN 21 Secretariat, Paris, France.

Ruderich, R., Fernholz, H. H., 1986. An experimental investigation of a turbulent shear flow with separation, reverse flow, and reattachment. Journal of Fluid Mechanics 163, 283-322.

Shademan, M., Barron, R. M., Balachandar, R., Hangan, H., 2014a. Numerical simulation of wind loading on ground-mounted solar panels at different flow configurations. Canadian Journal of Civil Engineering 41, 728-738.

Shademan, M., Balachandar, R., Barron, R. M., 2014b. Detached eddy simulation of flow past an isolated inclined solar panel. Journal of Fluids and Structures 50, 217-230.

Siddiqui, M. H. K., Loewen, M. R., Richardson, C., Asher W. E., Jessup, A. T., 2001. Simultaneous particle image velocimetry and infrared imagery of microscale breaking waves. Physics of Fluids 13, 1891–1903.

Stathopoulos, T., Zisis, I., Xypnitou, E., 2014. Local and overall wind pressure and force coefficients for solar panels. Journal of Wind Engineering and Industrial Aerodynamics 125, 195-206.

Straatman, A. G., Martinuzzi, R. J., 2002. A comparison of second-moment closure models in the prediction of vortex shedding from a square cylinder near a wall. Transactions of the ASME: Journal of Fluids Engineering 124, 728-736.

Suaris, W., Irwin, P., 2010. Effect of roof-edge parapets on mitigating extreme roof suctions. Journal of Wind Engineering and Industrial Aerodynamics 98, 483–491.

Tieleman, H. W., 2003. Wind tunnel simulation of wind loading on low-rise structures: a review. Journal of Wind Engineering and Industrial Aerodynamics 91, 1627-1649.

Visscher, B. T., Kopp, G. A., 2007. Trajectories of roof sheathing panels under high winds. Journal of Wind Engineering and Industrial Aerodynamics 95, 697–716.

Warsido, W. P., Bitsuamlak, G. T., Barata, J., 2014. Influence of spacing parameters on the wind loading of solar array. Journal of Fluids and Structures 48, 295-315.

Wheeler, A. J., Ganji, A. R., 2003. Introduction to engineering experimentation. 2nd edition. Pearson Education Inc., New Jersey, USA.

Wood, G. S., Denoon, R. O., Kwok, K. C. S., 2001. Wind loads on industrial solar panel arrays and supporting roof structure. Wind and Structures 4, 481-494.

Chapter 4

Effect of wind on an array of ground mounted solar panels

4.1 Introduction

Utility scale photovoltaic (PV) power stations or solar farms are emerging as a significant contributor to the electricity generation. As of 2014, at least 53 solar farms with capacity more than 50MW are operating in 13 countries (REN 21, 2014), whereas before 2009, only one solar farm had installed capacity of more than 50MW (Olmedilla PV Park, Spain, 60MW). Typically, solar farms are sited in a large open field and employ arrays of ground mounted solar PV panels designed to supply electricity to the commercial power grid. Optimizing PV panel support structures to withstand aerodynamic forces is one of the challenges experienced by the solar panel manufacturer and installer. Both experimental (Radu et al., 1986; Radu and Axinte, 1989; Wood et al., 2001; Kopp et al., 2002; Chung et al., 2008, 2011; Kopp et al., 2012; Aly and Bitsuamlak, 2013; Kopp and Banks, 2013; Pratt and Kopp, 2013; Banks, 2013; Browne et al., 2013; Cao et al., 2013; Aly and Bitsuamlak, 2014; Stathopoulos et al., 2014; Warsido et al., 2014) and numerical studies (Bitsuamlak et al., 2010; Meroney and Neft, 2010; Shademan et al., 2014; Jubayer and Hangan, 2014) have been performed to investigate wind loads on solar panels. As the focus of this study is on solar farms, only studies on arrays of ground mounted solar panels are discussed here.

In the study by Bitsuamlak et al. (2010), one case of arrayed ground mounted solar panel case was studied using numerical simulations. Three stand-alone systems were arranged in tandem for the arrayed configuration and only one wind direction (180^{o}) was considered. It was found that the sheltering effect from the upwind panel reduced wind loading on the downstream panels significantly. However, the Large Eddy Simulation (LES) modelling approach used was rather challenging for the domain size employing a grid size limited to 1.68×10^{6} cells for a Reynolds number of 2.5×10^{6}. According to Spalart et al. (1997), for Reynolds numbers of the order of 10^{7}, a computational grid consisting of a minimum of 10^{11} cells has to be used to fully resolve the surface layer and obtain a fully developed aerodynamic solution for LES. A wind tunnel study on a ground mounted solar panel array was performed by Kopp et al. (2012) to investigate the effect of buildings on roof mounted arrays since roof mounted arrays were the principal focus of this study. For the ground mounted array, 0^{o} and 180^{o} wind directions for a 20^{o} panel inclination were tested. A total of 12 rows of panels were arranged in tandem to form the array. For both wind directions (0^{o} and 180^{o}), wind load was maximum for the first windward row then it became minimum at around the third or fourth row, followed by load increasing on further downstream rows. Shademan et al. (2014) investigated the effect of row spacing for a ground mounted solar panel array for 45^{o} inclination angle and for only 0^o wind direction. Steady Reynolds-Averaged Navier-Stokes (RANS) approach was used with Shear Stress Transport (SST) k-ω turbulence model. It was observed that the row spacing did not have an effect on wind loading of the first windward row of panels. However, for the rest of the rows, drag increased and lift decreased with the increase of row spacing. North American building standards (ASCE 7-10, 2010 and National Building Code of Canada, 2010) do not cover any information regarding minimum design wind load for solar panel arrays, either ground mounted or roof mounted. However, Australia (AS/NZS 1170.2, 2011) and California (SEOAC, 2012) have some standards for roof mounted solar panels but not for ground mounted installation. Clearly, published literatures and building standards lack information for designing wind loads on ground mounted solar panels in an array configuration as in solar farms.

The present study is performed to investigate not only the wind load but also the underlying aerodynamic mechanism responsible for wind loads on a ground mounted solar panel array. Four wind directions (0^o, 45^o, 135^o and 180^o) are considered here. Computational Fluid Dynamics (CFD) approach with 3D Reynolds-Averaged Navier-Stokes (RANS) simulation is undertaken to satisfy the objective of this study. CFD methodology used here is similar to the study by Jubayer and Hangan (2014) in which the wind loading on a stand-alone ground mounted solar panel has been estimated. However, configurations of a stand-alone system and an array of panels are completely different, and the setup of the numerical model is modified accordingly. In this study, the critical wind directions are clearly identified based on drag, lift and overturning moment acting on the individual row of panels in the array. Also, the surface pressure distributions are analyzed in relation to the wind flow field around the solar panel. This current study extends the work of Jubayer and Hangan (2014) from a stand-alone system to arrays of ground mounted solar panel with application to utility scale PV power stations.

4.2 Methodology

Details of the numerical modelling setup are discussed here. This section includes the geometrical specification of the solar panel array, dimension of the computational domain and mesh, boundary conditions and different types of numerical schemes used.

4.2.1 Solar panel model details

The dimension of the individual solar panel module used for the solar panel array is 1.2 m (length) × 0.6 m (width) × 0.007 m (thickness). The stand-alone system has 24 aforementioned individual solar panel modules arranged in 4 (row) × 6 (column) with 25^o inclination. The generic array configuration for solar farms used in the present study has 5 rows of panels with each row having 3 stand-alone systems side by side. A distance of 3.05 m between two consecutive support legs is maintained for the array configuration with the end legs having a distance of 0.24 m from the side edge of the array. The dimension of one array is 2.47 m (B) × 21.92 m (W) × 1.65 m (H) (Fig. 4.1). The clearance between two consecutive rows is 1.04H.

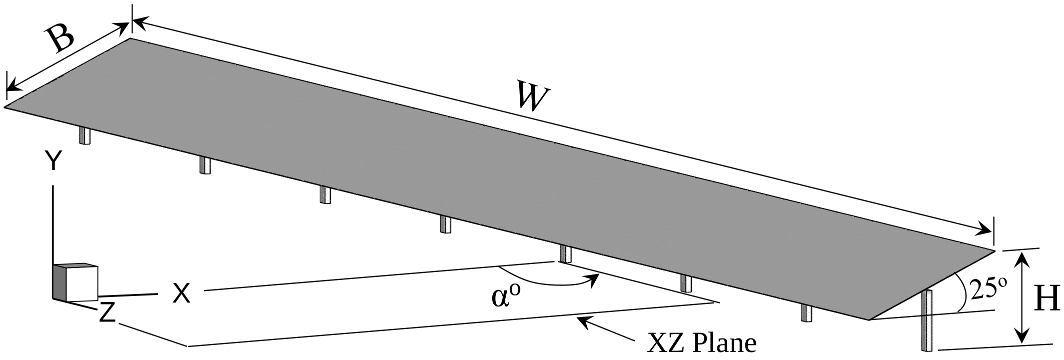

Figure 4.1: Computational model of a single array with wind direction (α°) shown in the XZ plane.

4.2.2 Computational grid

The COST guideline for CFD simulation in the urban environment developed by Franke et al. (2007) is followed to create the computational domain and mesh. The dimension of the domain is 30.2H (X) × 6.0H (Y) × 48.4H (Z) for 0° and 180° wind directions, and 36.3H (X) × 6.0H (Y) × 52.0H (Z) for 45° and 135° wind directions (see Figure 4.1 for wind direction, α°). For all four domains corresponding to the four wind directions, clearances between the solar panel array and the computational domain boundary are as follow: from inlet 5H, from outlet 14.3H, from top of the domain 5H, from sides of the domain 17.6H. A hybrid mesh with a combination of prismatic, hexahedral and tetrahedral types of cells is created to reduce the number of tetrahedral cells in the domain (Franke et al., 2007). Arrangements of these cells are: prismatic cells on the surface of the panel, tetrahedral cells in an interior rectangular block containing the solar panel arrays and hexahedral cells else-where in the domain. Three different grids with 1,492,982 (G1), 2,209,925 (G2) and 2,780,048 (G3) cells are created for 0° wind direction to check grid sensitivity. A refinement ratio of about 1.3, which is within the suggested limit (between 1.2 and 1.5) proposed by Franke et al. (2007), is used from the coarsest grid to the finest grid. However, simulation with the coarsest grid (G1) was taking unusually longer time for each time step compared to the other two finer grids (G2 and G3) and hence was not continued. Grid sensitivity analysis is performed based on the surface average pressure coefficients. Between G2 and G3, the surface average pressure coefficients match within 2% difference on an average for all five rows of panels. Grid convergence index (GCI) proposed by Roache (1994) is also calculated based on the surface average pressure coefficients. Second order discretization schemes are used in this study. For the fine grid (G3) solution, GCI [fine grid] is 8.43%. Now, for the contrary situation when GCI is calculated based on the coarse grid (G2) (Equation 14 in Roache, 1994), GCI [coarse grid] is 13.13%. Grid convergence index is an estimator of grid uncertainty and is derived from the theory of the generalized Richardson Extrapolation. Given the GCI values as well as the percent difference in the surface average pressure coefficient values between G2 and G3, G2 is chosen as the final grid for simulation considering the available computational resources. For the other wind directions, distances between grid points are kept similar to G2 on all edges of the computational domain. However, due to tetrahedral elements and different orientations of the panel, total number of cells is different between the straight wind (0^o and 180^o) and the oblique wind (45^o and 135^o) cases. Number of cells, in each of the computational domains for 0^o and 180^o wind directions, is 2.2 million each, whereas for 45^o and 135^o wind directions, it is 2.1 million cells. Figure 4.2 shows the 2D sectional and 3D isometric view of the generated mesh for 0^{o} wind direction.

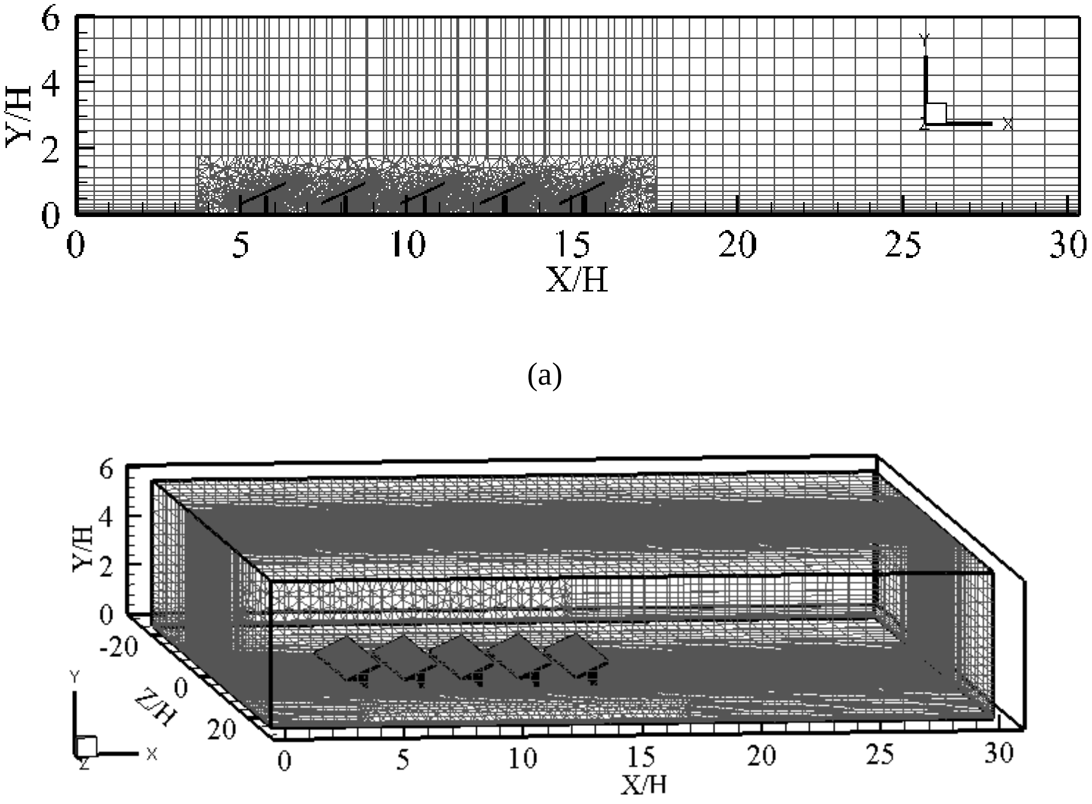

(a)

(b)

Figure 4.2: Computational domain and mesh for 0^{o} wind direction (a) sectional view (b) isometric view.

4.2.3 Numerical model details

Three dimensional RANS simulations are carried out using a transient solver in the open source CFD software package OpenFOAM® 2.1.0 (ESI Group) (Weller, 2005). The transient solver pisoFoam, which applies PISO (Pressure Implicit with Splitting of Operators) algorithm (Issa, 1986) to solve the Navier-Stokes equations, is used. The SST k-ω turbulence model (Menter, 1994) is employed in this study. Shademan et al. (2014) showed that the SST k-ω performed better than Realizable k-ε turbulence model for flow around an inclined plate. Previous studies also employed SST k-ω for Atmospheric Boundary Layer flows (Yang et al., 2009; Karava et al., 2011, 2012; Jubayer and Hangan, 2014). Boundary conditions and wall-functions are similar to the study by Jubayer and Hangan (2014) with ESDU (1982, 1983) velocity and turbulence intensity (TI) profiles for open terrain roughness ($y_0 = 0.03$ m) at the inlet, fixed uniform zero gauge pressure at the outlet, slip walls at sides of the domain, fixed values of velocity and turbulence properties from the top of the inlet boundary throughout the top of the domain, no slip rough wall at the bottom of the domain and no slip smooth walls at the surface of the solar panel (Fig. 4.3). The Reynolds number based on the incident wind speed at H and the length scale B is 2.96×10^6.

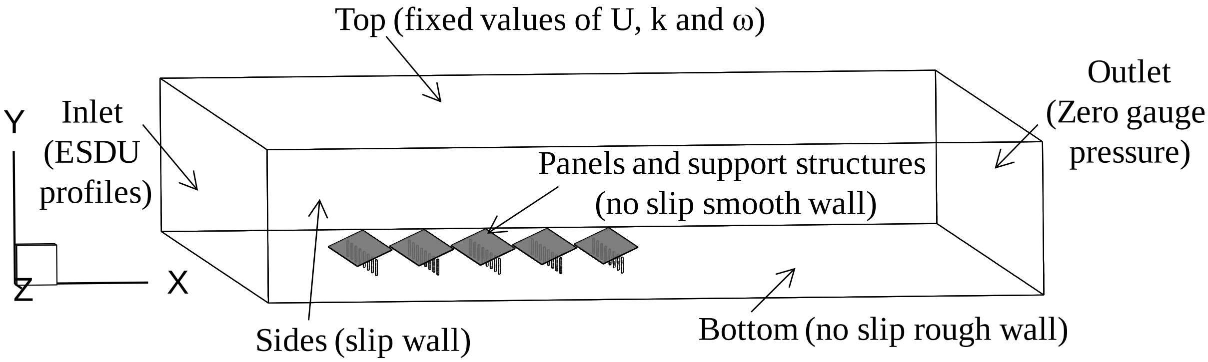

Figure 4.3: Boundary conditions.

A second order numerical scheme is chosen for the discretization of gradient, divergence and Laplacian terms in the equations being solved. Linear interpolation scheme is chosen for the interpolations of values from cell center to face center. Variable time steps are used with the maximum non-dimensional time step size, Δt^* (= $\Delta t\overline{U_H}/B$, Δt is the time step (s), $\overline{U_H}$ is the mean wind speed at panel height (H) in the undisturbed flow (m/s) and B is the breadth of the panel (m)) of $7.2\text{x}10^{-4}$. Time step sizes are dictated by the Courant number = $v\Delta t/\Delta l$, which is kept below 1; where v is the local mean wind speed (m/s), Δt is the time step (s) and Δl the dimension of the grid cell in the flow direction (m)). For each wind direction, simulation is run for a non-dimensional time, t^* (= $t\overline{U_H}/B$, here t is the flow time (s)) of 144 and data for the initial t^* = 36 is skipped in the data analysis to avoid the initial numerical instability. Omitting data up-to t^*= 36 is decided based on time histories of drag and lift coefficients for each wind direction. Before running simulations with the solar panel array inside the domain, simulations are performed inside an empty domain to ensure that the equilibrium ABL flow (Blocken et al., 2007) is achieved. To obtain the equilibrium ABL flow, similar steps as in Jubayer and Hangan (2014), which involved treating of roughness at the bottom of the domain, boundary conditions and turbulence model constants, are followed. Inlet and incident velocity and turbulence intensity profiles inside the empty domain are shown in Figure 4.4. Heights are normalized with the panel height (H) and velocities are normalized with wind speed at height H ($\overline{U_H}$). Between the lower edge (0.36H) and the upper edge height (H) of the panel, inlet and incident profiles match with each other within 3% difference for both mean wind speed and turbulence intensity. It should be noted that at the top of the domain gradient of wind speed is not zero as the atmospheric boundary layer is much thicker than the domain height.

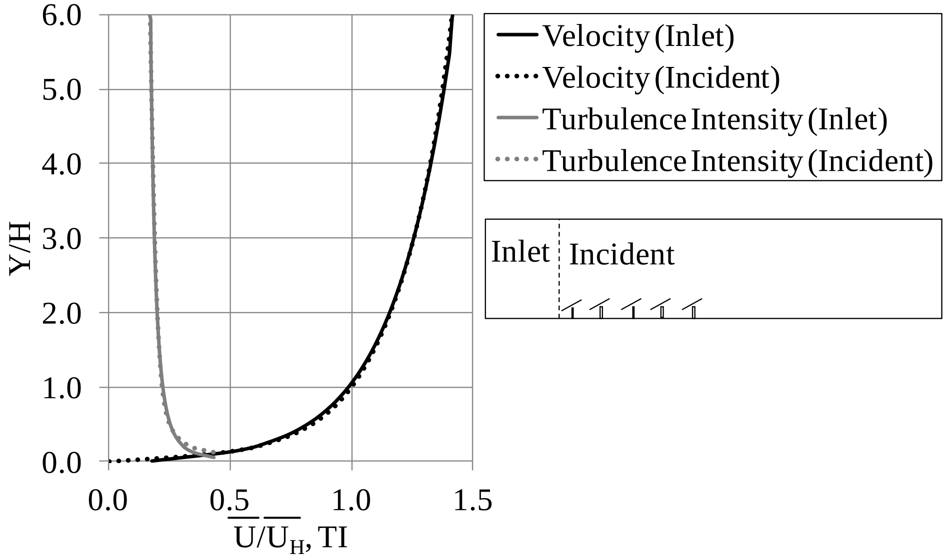

Figure 4.4: Inlet and incident velocity and turbulence intensity profiles.

4.3 Numerical model validation

The numerical modelling approach used in this study is validated for a stand-alone PV system rather than the array due to availability of experimental results. Surface pressures on the panel as well as the wind flow-field around the panel are compared with experiments performed in the Boundary Layer Wind Tunnel I (BLWT I) at Western University. Although a stand-alone system is employed, the setup of the corresponding numerical simulation is similar to the array configuration described in Section 4.2.3. Geometry of the stand-alone system employed in CFD is identical to the system in Jubayer and Hangan (2014). Validation of the numerical model for surface pressure can also be found in Jubayer and Hangan (2014). Here, validation of the flow field around the solar panel is reported. Mean velocity profiles around the stand-alone solar panel are compared with a Particle Image Velocimetry (PIV) experiment. The same 1:10 scale pressure model of the stand-alone solar panel reported in Jubayer and Hangan (2014) is used in the PIV experiment with the pressure tubes removed and painted black. Reynolds numbers for the CFD and PIV, based on wind speed at height H, are 3.0×10^6 and 8.3×10^4 respectively. According to Tieleman (2003), Reynolds number equality can be relaxed for sharp edged body as long as the Reynolds number does not fall below 5×10^4. Comparison between CFD and experiment is shown for all four wind direction cases (0^o, 45^o, 135^o and 180^o). In the PIV experiment, measurements are taken at the plane between two support legs parallel to the side walls of the wind tunnel for 0^o and 180^o wind directions. For 45^o and 135^o wind directions, measurements are performed in a vertical plane through the panel center parallel to the side walls of the wind tunnel. Figure 4.5 shows the mean streamwise and vertical velocity components obtained from CFD and PIV at the measurement planes. Profiles are plotted at distance interval of B′/8 from the leading edge of the panel towards the trailing edge. Here, B′ is the panel breadth in the respective measurement plane for each wind direction. In Figure 4.5, distances and velocities are normalized with H and $\overline{U_H}$ respectively. For 0^o and 45^o wind directions, both mean streamwise and vertical velocity components match well between PIV and CFD (Fig. 4.5 a-d). However, for 135^o and 180^o wind directions, mean streamwise velocity components are over-predicted by CFD than PIV close to the leading edge on the leeward side of the panel (Fig. 4.5 e,g). Several factors, such as the Reynolds number difference and the higher thickness of the panel in experiment than the specified geometric scale of 1:10 to get enough rigidity to withstand the wind, may have created a larger separation bubble in PIV compared to CFD and thus the lower wind speed in PIV on the leeward side of the panel for 135^o and 180^o wind directions.

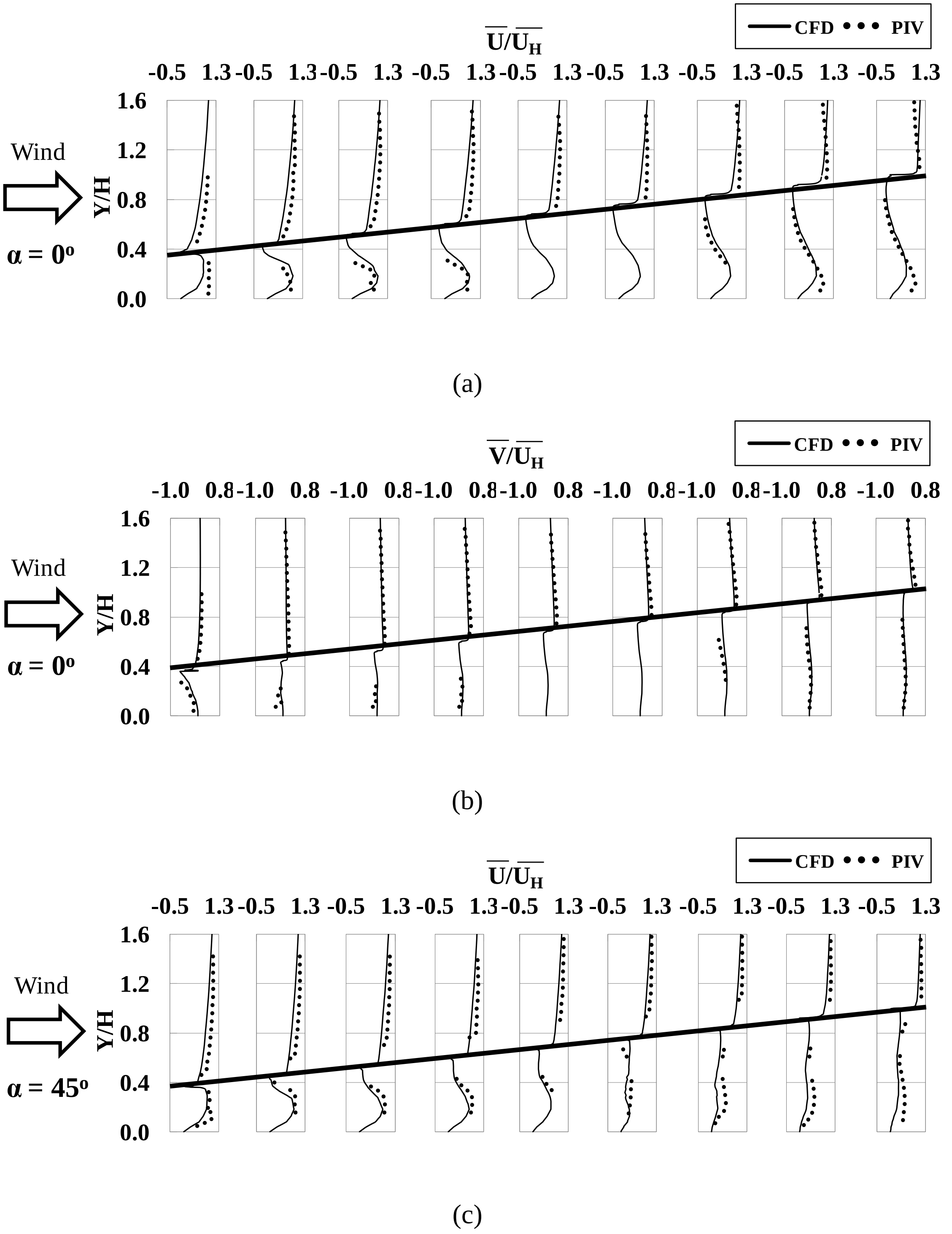

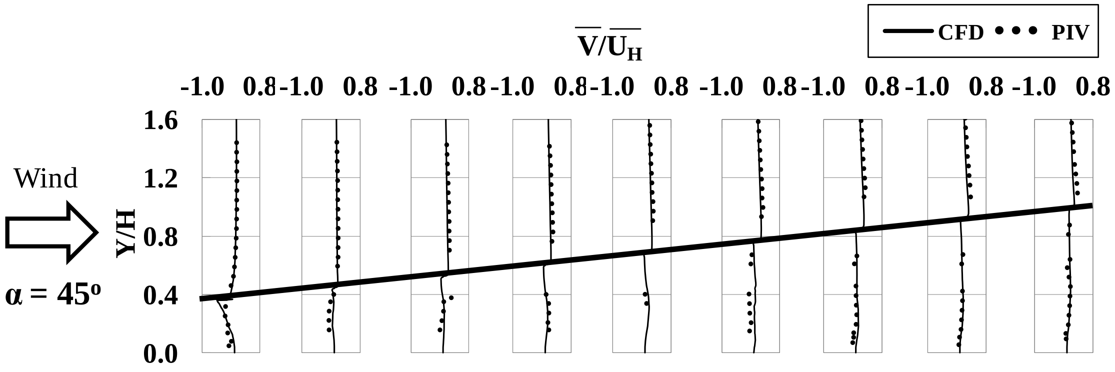
CFD
PIV
$\overline{V}/\overline{U_H}$
-1.0 0.8 -1.0 0.8 -1.0 0.8 -1.0 0.8 -1.0 0.8 -1.0 0.8 -1.0 0.8 -1.0 0.8 -1.0 0.8
Y/H
1.6
1.2
0.8
0.4
0.0
Wind
α = 45°

(d)

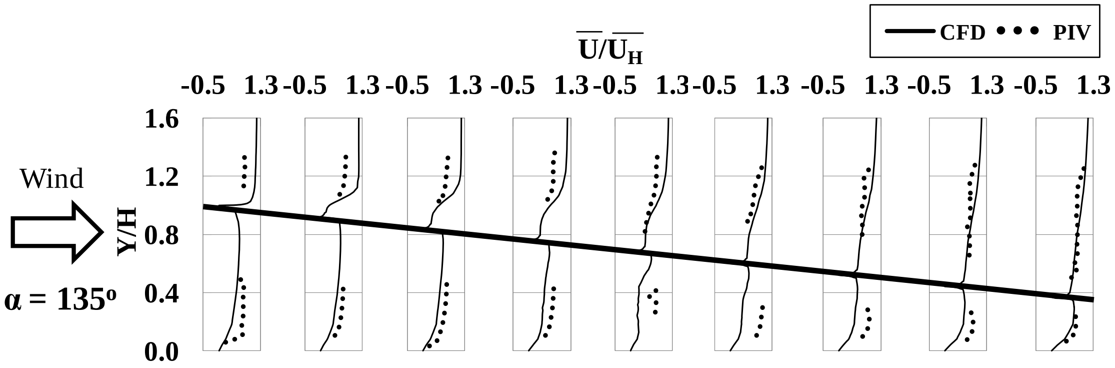
CFD
PIV
$\overline{U}/\overline{U_H}$
-0.5 1.3 -0.5 1.3 -0.5 1.3 -0.5 1.3 -0.5 1.3 -0.5 1.3 -0.5 1.3 -0.5 1.3 -0.5 1.3
Y/H
1.6
1.2
0.8
0.4
0.0
Wind
α = 135°

(e)

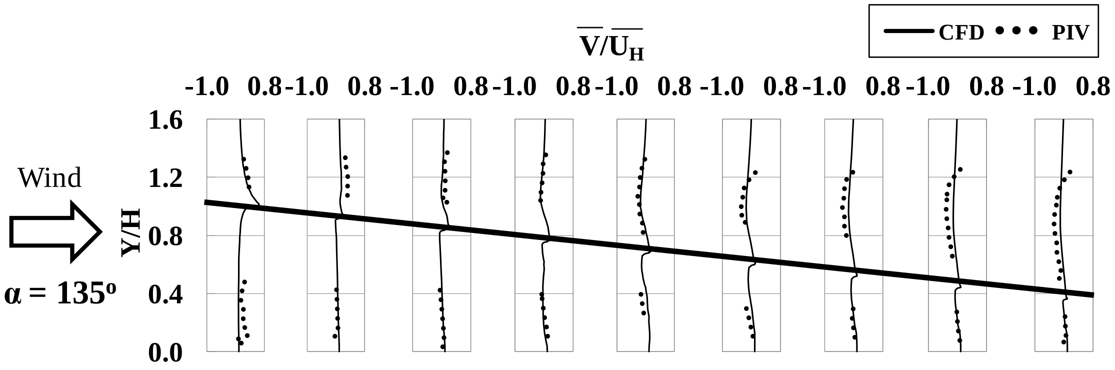
CFD
PIV
$\overline{V}/\overline{U_H}$
-1.0 0.8 -1.0 0.8 -1.0 0.8 -1.0 0.8 -1.0 0.8 -1.0 0.8 -1.0 0.8 -1.0 0.8 -1.0 0.8
Y/H
1.6
1.2
0.8
0.4
0.0
Wind
α = 135°

(f)

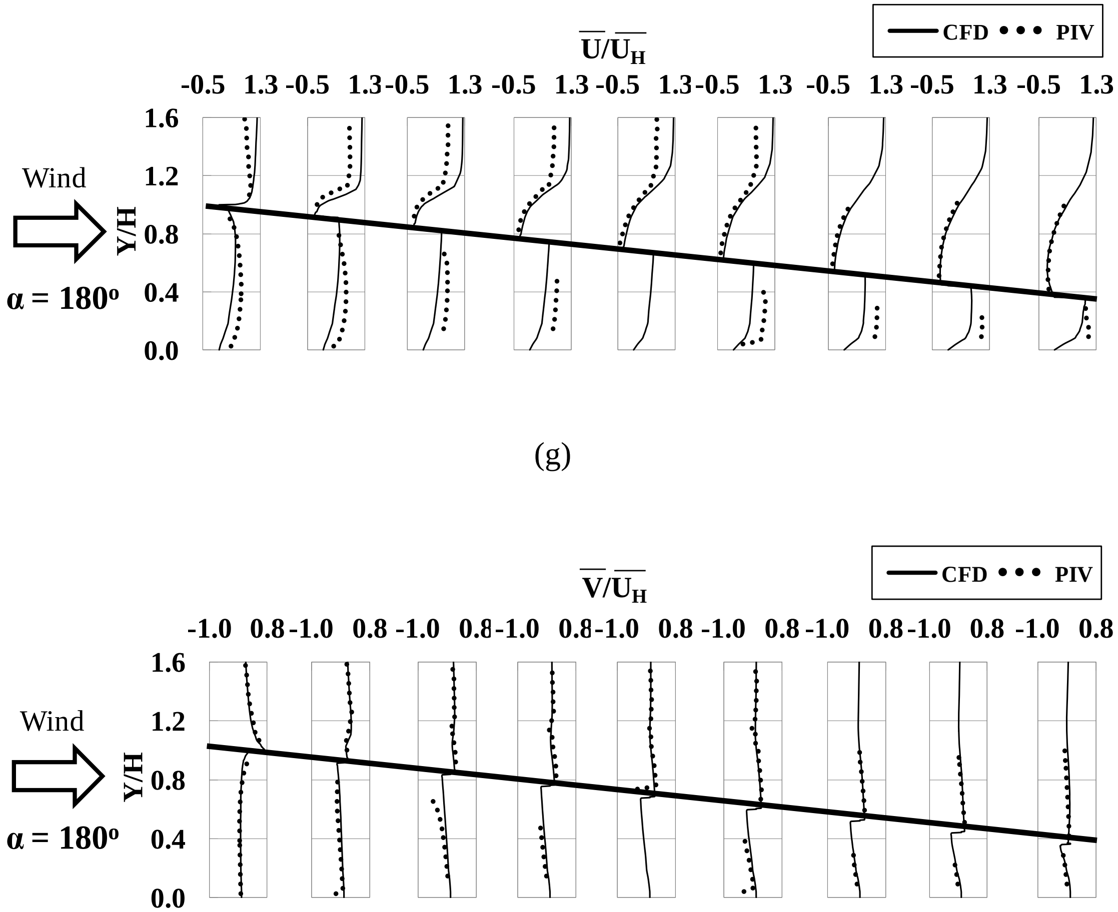

(g)

(h)

Figure 4.5: Comparison of the normalized mean streamwise ($\overline{U}$) and vertical ($\overline{V}$) velocity profiles on the surfaces of the solar panel between CFD and PIV for (a) α = 0^o, $\overline{U}$, (b) α = 0^o, $\overline{V}$, (c) α = 45^o, $\overline{U}$, (d) α = 45^o, $\overline{V}$, (e) α = 135^o, $\overline{U}$, (f) α = 135^o, $\overline{V}$, (g) α = 180^o, $\overline{U}$ and (h) α = 180^o, $\overline{V}$.

In contrast, mean vertical velocity components obtained from CFD and PIV for 135^o and 180^o wind directions agree well (Fig. 4.5 f,h). Overall, the agreement between the CFD study with the unsteady RANS simulation using SST k-ω turbulence model and the PIV measurements performed in this study is reasonable in terms of mean streamwise and vertical velocity components.

4.4 Results and discussion

The principal objective of the present study is to analyze the aerodynamic loading of the panel as a function of the position of the panel in the array as well as the associated wind flow field around the solar panel array. The section starts with discussing the wind flow field surrounding the array of panel and followed by the surface pressure distribution on the array of panels. Finally the aerodynamic loading on the panel, calculated from the surface pressure, is addressed.

4.4.1 Wind flow field characteristics

Normalized mean velocity contours with streamlines in vertical planes through the center of the solar panels surface and parallel to the side edge of the panels are shown in Figure 4.6. For all figures presented in the entire Section 4.4, Row 1 is always the leading row irrespective of the wind direction. For 0^o wind direction (Fig. 4.6 a) at Row 1, flow is attached on the upper surface of the row of panels while on the lower surface, it separates at the leading edge forming a separation-reattachment bubble. Rows 2 to 5 are completely in the wake of the first row of panels. Interestingly, separation bubbles are observed on the upper surface for Rows 3 to 5 and the size of these bubbles increases downstream. Due to the sheltering effect from Row 1 on Rows 2 to 5 for the 0^o wind direction case, very low wind speeds around these rows (2 to 5) are observed. For 45^o wind direction (Fig. 4.6 b), a very small vortex is observed close to the leading edge on the lower surface for all rows. This small vortex may be associated to the formation the corner vortices at this oblique wind direction. On the other hand, flow impingement occurs on the upper surfaces around the middle of the panels for Rows 3 to 5. From the velocity magnitude contour for 0^{o} and 45^{o} wind direction, it can be seen that Rows 2 to 5 at 45^{o} wind direction experience higher wind speeds than for the 0^{o} wind direction. For 135^{o} wind direction (Fig. 4.6 c), flow impingement can be seen on lower surfaces and close to the leading edges for all rows. On the upper surface of Row 1, a large vortex rotating clockwise is generated from the leading edge and a relatively smaller vortex rotating counter-clockwise is generated from the trailing edge of the panel (Fig. 4.6 c). From Row 1 towards Row 5, both these vortices decrease in size. The same observation can be made for the upper surfaces for 180^{o} wind direction (Fig. 4.6 d) as for the 135^{o} wind direction. Also, similar to 0^{o} wind direction, Rows 2 to 5 are completely in the wake of Row 1 for 180^{o} wind direction. Out of all these four wind directions, the maximum wind velocity magnitude is observed around Rows 2 to 5 for 135^{o} wind direction. All these observed flow characteristics are directly correlated with the surface pressure distribution on surfaces of the solar panel and will be described in the next section.

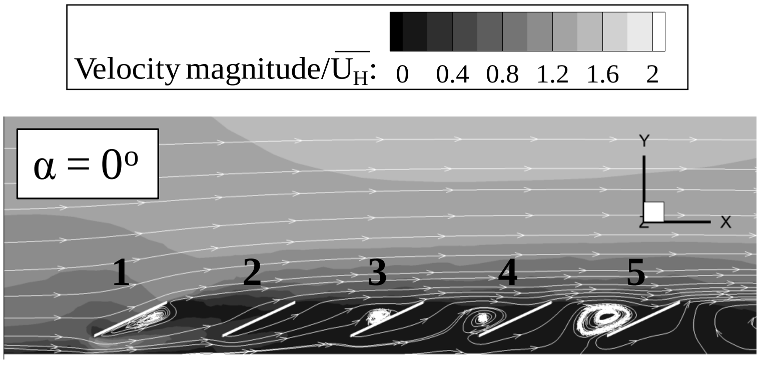

(a)

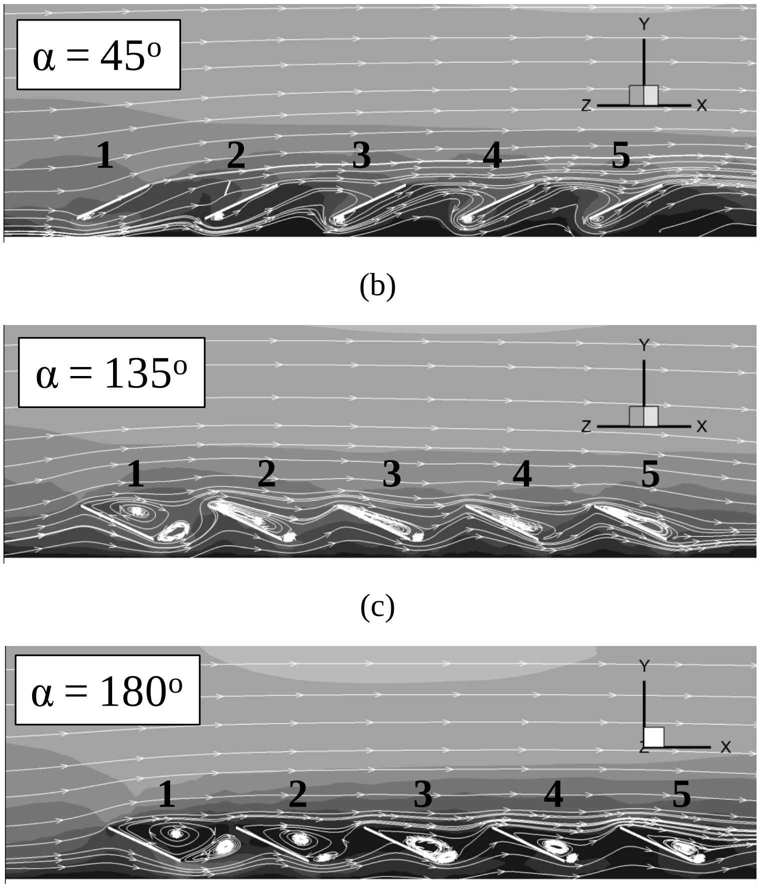

(b)

(c)

(d)

Figure 4.6: Normalized mean velocity magnitude contours with streamlines at the plane through the center of the panel and parallel to the side edge of the panel for (a) 0^o, (b) 45^o, (c) 135^o and (d) 180^o wind directions.

4.4.2 Surface pressure distribution

Surface pressure distributions in terms of mean C_p on the upper and lower surfaces for every row of panels are provided in Figure 4.7 for all four wind directions. For the calculation of C_p presented in Figure 4.7, reference velocity and pressure are measured at panel height H in the undisturbed flow. Please note that C_p value ranges in the contour plots are different from one wind direction to the other and also between upper and lower surfaces. For 0^o wind direction, Row 1 experience higher wind loads, due to higher C_p on the upper surface and lower C_p on the lower surface, than other four rows (Fig. 4.7 a). Especially, surface area close to the leading edge for Row 1 sees the maximum wind load since the incoming flow impinges in the region close to the leading edge on the upper surface (Fig. 4.6 a). For Rows 2 to 5, major portions of the surface area on upper and lower surfaces have negative C_ps and as these rows (Rows 2 to 5) are in the wake of Row 1 (Fig. 4.6 a), they show much lower net mean C_p than Row 1. Also, higher net mean C_p values are observed at regions close to both corners of the leading edge for Rows 2 to 5. For 45^o wind direction, the critical region, in terms of maximum net mean C_p, is the region close to the leading shorter edge for all rows (Fig. 4.7 b). Conical shape C_p distributions on the leeward surface at the leading edge corner of each row suggest the presence of corner vortices (Fig. 4.7 b), a hint of which can be found in Figure 4.6 b. Overall, similar C_p distribution is found on both upper and lower surfaces of Rows 2 to 5 which is due to the similar flow distribution around these rows for wind direction of 45^o (Fig. 4.6 b). Comparable to the 45^o wind direction case, lower C_p values in a conical shape distribution are observed on the leeward side of the panel for 135^o wind direction for all five rows (Fig. 4.7 c). These negative C_p values at the leading edge corner on the leeward side and positive C_p values at same corners on the windward side of the panel will result in maximum uplift at the leading edge corner region. For all wind directions, the entire Row 1 shows higher wind loads than the other rows. This is because the flow impinges and remains attached on the windward surfaces in Row 1 for all wind directions

(Fig. 4.6 a-d), creating the maximum positive pressure on the windward side and thus resulting in higher net pressure combining windward and leeward surfaces for Row 1.

Surface averaged net mean pressure coefficients for each row are compared with the wind tunnel study by Kopp et al. (2012) (Fig. 4.8). Since the study by Kopp et al. (2012) considered only 0^o and 180^o wind directions, comparison is shown for these two wind directions. Net mean pressure coefficients are calculated using area weighted average C_p values from both upper and lower surfaces of the solar panel. In Figure 4.8, net mean C_p is positive when acting upwards normal to the panel surface and negative when acting downwards. In the study by Kopp et al. (2012) a total of 12 rows were used and the reference point for mean C_p calculation was taken at the panel height, H. The same reference pressure and wind speed are used in the present study and only the five leading rows from the Figure 4.8 shows that for both wind directions, the present net mean C_p values from the present study follow similar trend as the experiments. For both 0^o and 180^o wind directions, the maximum load is observed for Row 1. The load then decreases to the minimum load at Row 3, and starts to increase towards Rows 4 and 5. However, there is an offset in magnitudes between the present study and the wind tunnel study. Several factors, such as the differences in the solar panel tilt angle (20^o in experiments; 25^o in present study), W:B aspect ratio of each row (20:1 in experiments, 2012; 8.8:1 in the present study) and resolution of measurement locations on the panel surfaces (36 taps on the upper surface and 12 taps on the lower for each row in the wind tunnel study; 1000 grid points on each surface for each row in the present study) may have influenced this offset.

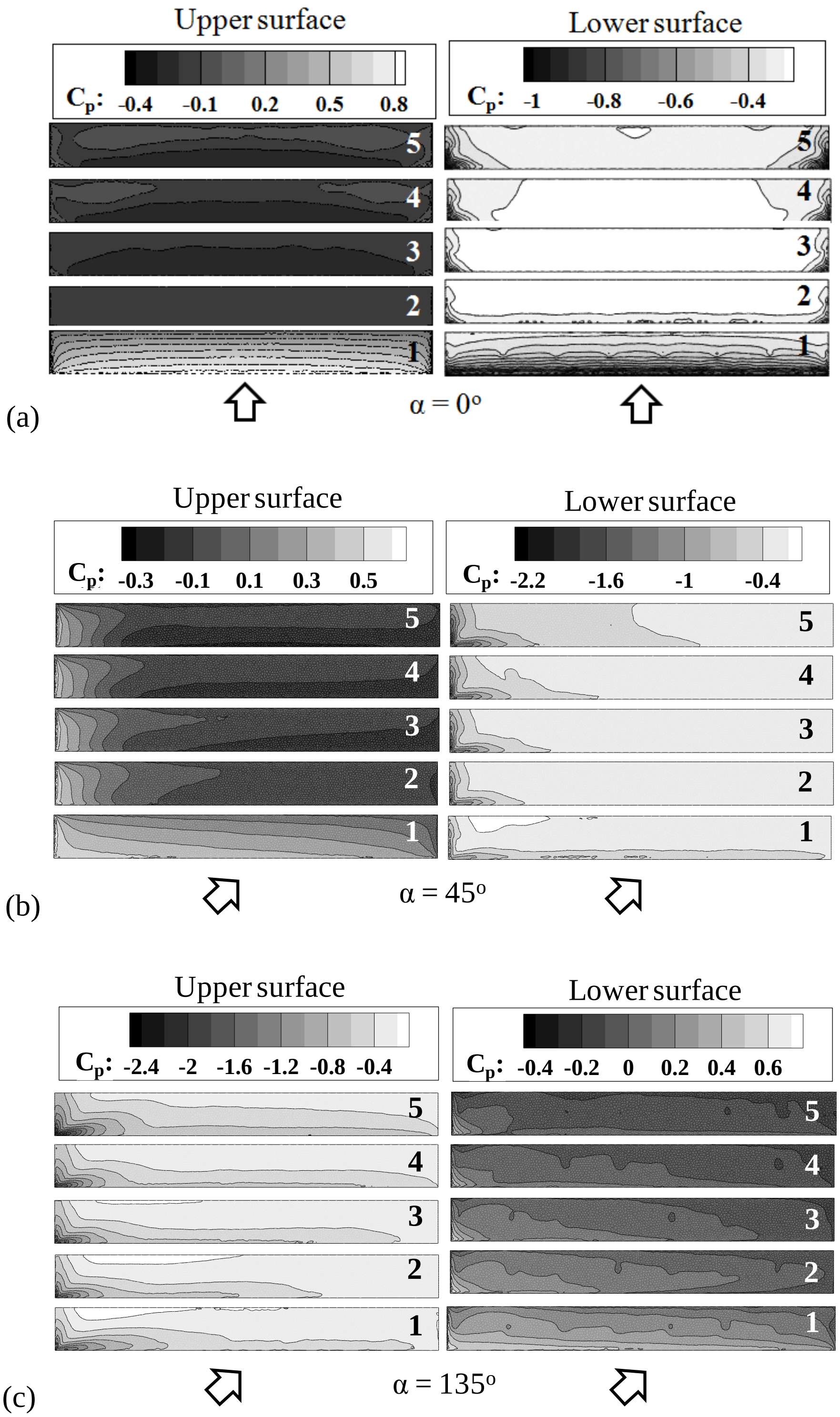
Upper surface
Lower surface
C_p: -0.4 -0.1 0.2 0.5 0.8
C_p: -1 -0.8 -0.6 -0.4
5
4
3
2
1
(a)
α = 0°
Upper surface
Lower surface
C_p: -0.3 -0.1 0.1 0.3 0.5
C_p: -2.2 -1.6 -1 -0.4
5
4
3
2
1
(b)
α = 45°
Upper surface
Lower surface
C_p: -2.4 -2 -1.6 -1.2 -0.8 -0.4
C_p: -0.4 -0.2 0 0.2 0.4 0.6
5
4
3
2
1
(c)
α = 135°

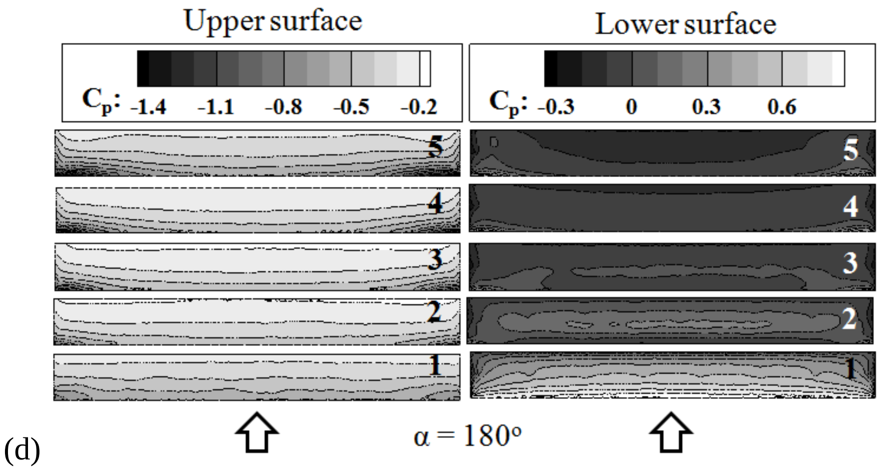

Figure 4.7: Mean C_p distributions on the upper and lower surfaces of the solar panels for (a) 0°, (b) 45°, (c) 135° and (d) 180° wind directions.

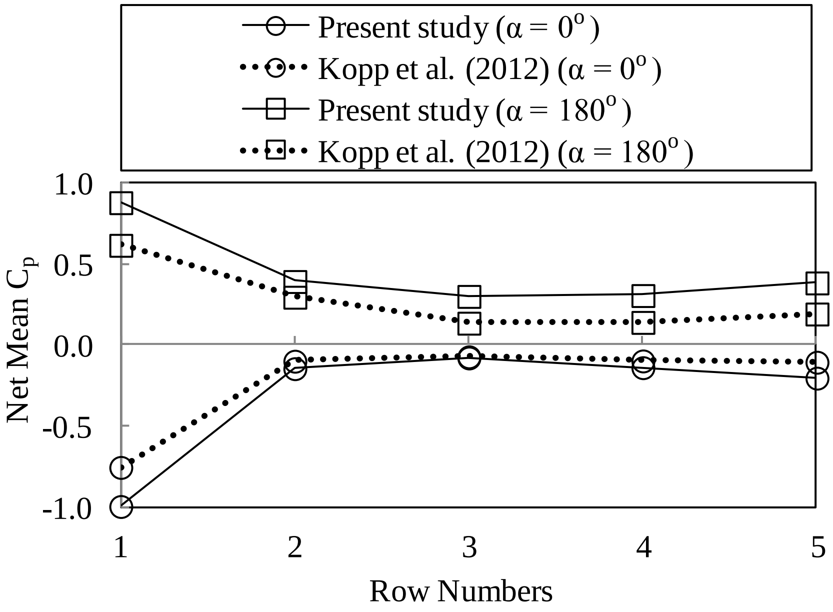

Figure 4.8: Comparison of the net mean C_p between the present study and Kopp et al. (2012).

4.4.3 Aerodynamic loading

Mean drag (C_D) and lift coefficients (C_L) for all four wind directions are shown in Figure 4.9. C_D is calculated using $C_D = \Sigma C_{Pi}A_i\cos(90\text{-}\theta)/A$, where C_{Pi} is the mean pressure coefficient on a specific grid point on the surface, A_i is the associated area on the panel surface of that grid cell (m^2) and A is the total upper or lower surface area of a single row of panels (m^2). from the upper and lower surface of the panel and θ the solar panel tilt angle (25^o). Similarly, C_L is calculated using $C_L = \Sigma C_{Pi}A_i\sin(90\text{-}\theta)/A$. Sign conventions used in Figure 4.9 are as follows: drag acting against the flow is positive and upward lift is positive. Figure 4.9 shows that for all four wind directions, the first windward row (Row 1) is the critical row compared to the rest of the rows (Rows 2-5) based on higher drag and lift. In terms of individual loading component, 180^o wind direction is critical for maximum uplift and 0^o wind direction is for maximum drag. Also, minimum wind loads (both drag and lift) are found at Row 3 for 0^o and 180^o wind directions, at Row 2 for 45^o wind direction and at Row 4 for 135^o wind direction. Another interesting observation from Figure 4.9 is that, for Rows 2 to 5, wind loads are higher for oblique winds (45^o and 135^o) than straight winds (0^o and 180^o). Higher wind speeds around Rows 2 to 5 for 45^o and 135^o wind directions than for 0^o and 180^o wind directions (Fig. 4.6 a-d) relates to the increased wind loads for oblique winds. Apart from drag and lift, the overturning moment is also an important design parameter for solar panels. In this study, overturning moment coefficients about Z axis (C_{Mz}) is found to be significantly higher than the moment coefficient about X and Y axis.

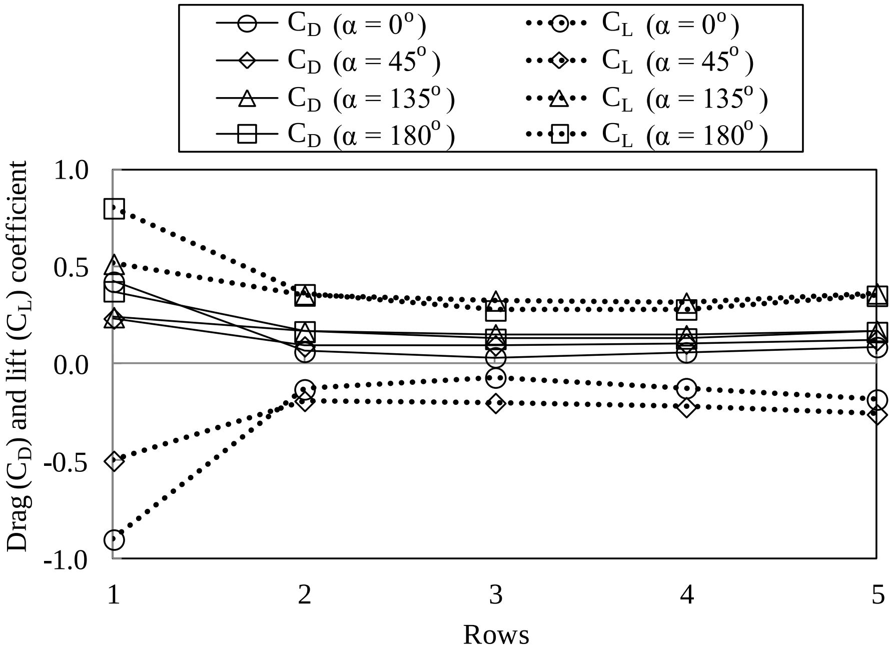

Figure 4.9: Mean drag (C_D) and lift coefficients (C_L).

Thus, only C_{Mz} is shown in Figure 4.10 for all wind directions. C_{Mz} is calculated using $C_{Mz} = M_z/(0.5\rho\overline{U_H}^2AB)$, here M_z is the vector sum of moments from the upper and lower surfaces of the panel (N-m), $\overline{U_H}$ is the reference velocity measured at panel height H (m/s) and B is the breadth of a row (m). The centre of the inclined surface of a single row of panels is taken as the reference point for the moment calculation. The sign convention for C_{Mz} is shown in Figure 4.10. Clearly, in terms of overturning moment, the 45^o and 135^o wind directions are critical cases. Unlike drag and lift, Rows 2 to 5 also experience higher overturning moments as Row 1 for 45^o and 135^o wind directions. However for 0^o and 180^o wind directions, C_{Mz} is significantly higher for Row 1 than Rows 2 to 5.

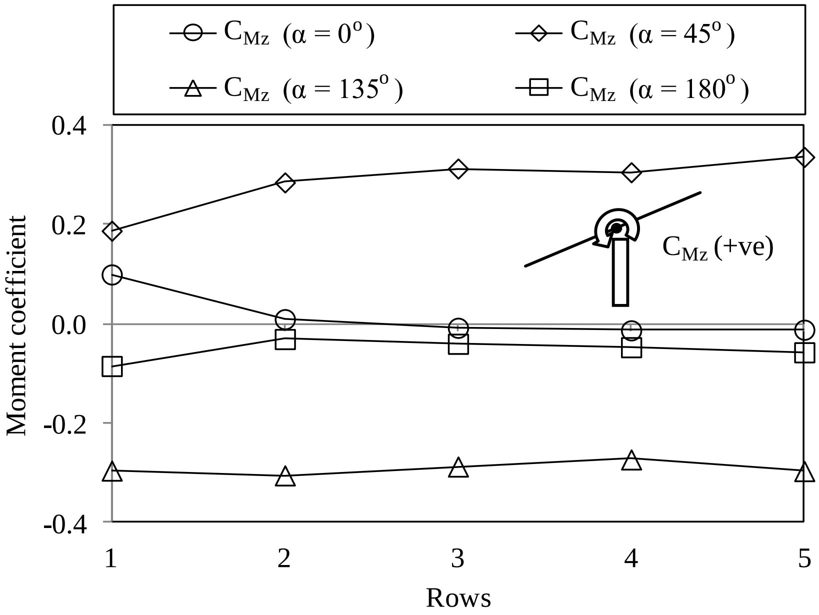

Figure 4.10: Mean overturning moment coefficients about Z axis (C_{Mz}).

4.5 Concluding remarks

The current study investigated the wind loads and the wind flow fields around an array of ground mounted solar panels using computational fluid dynamics (CFD). The validation study on a stand-alone solar panel system showed that the numerical modelling approach employed in this study, which is 3D Reynolds-Averaged Navier-Stokes (RANS) simulation with an unsteady solver and Shear Stress Transport (SST) k-ω turbulence model, predicted the wind speed around a ground mounted stand-alone solar panel system reasonably well. Based on the investigation carried out in this study on the array configuration, the following conclusion can be made:

- For 0^o and 180^o wind directions, Rows 2 to 5 are completely in the wake of the first windward row (Row 1).

- Corner vortices are observed on the leeward sides of all five rows of panels for 45^o and 135^o wind directions.
- Row 1 experiences the maximum wind loads (drag and lift) for all four wind directions (0^o, 45^o, 135^o and 180^o).
- At Row 1, the maximum uplift is observed for 180^o wind direction whereas the maximum drag is for 0^o wind direction.
- For 0^o and 180^o wind directions, the wind loads (lift, drag and moment) are minimum for Row 3. However, for 45^o and 135^o wind directions, the minimum wind loads (lift and drag) are encountered by Row 2 and 4 respectively.
- For Rows 2 to 5, the wind loads (lift and drag) are higher for oblique winds (45^o and 135^o) than for straight winds (0^o and 180^o).
- The maximum overturning moment is found to be acting for 45^o and 135^o wind directions, unlike 0^o and 180^o wind directions, all rows show similar overturning moment coefficients for the 45^o and 135^o wind directions.
- Overall, this study provides a very detail analysis of wind effects on ground mounted solar panel array by considering not just straight wind directions (0^o and 180^o) but also oblique wind directions (45^o and 135^o). Also, high resolution velocity and surface pressure distributions (in terms of pressure coefficients) for all arrays of panels are reported which is one of the advantages of CFD.

References

Aly, A., Bitsuamlak, G., 2014. Wind induced pressures on solar panels mounted on residential homes. Journal of Architectural Engineering 20, 04013003.

Aly, A., Bitsuamlak, G., 2013. Aerodynamics of ground-mounted solar panels: Test model scale effects. Journal of Wind Engineering and Industrial Aerodynamics 123, 250-260.

ASCE 7-10, 2010. Minimum Design Loads for Buildings and Other Structures. ASCE 7-10, Virginia, USA: American Society of Civil Engineers.

AS/NZS 1170.2, 2011. Australian/New Zealand Standard Structural Design Actions, Part 2: 2011. Standards Australia International Ltd., Sydney, Australia.

Banks, D., 2013. The role of corner vortices in dictating peak wind loads on tilted flat solar panels mounted on large, flat roofs. Journal of Wind Engineering and Industrial Aerodynamics 123, 192-201.

Bitsuamlak, G. T., Dagnew, A. K., Erwin, J., 2010. Evaluation of wind loads on solar panel modules using CFD. The Fifth International Symposium on Computational Wind Engineering, Chapel Hill, North Carolina, USA, May 23-27.

Blocken, B., Stathopoulos, T., Carmeliet, J., 2007. CFD simulation of the atmospheric boundary layer: wall function problems. Atmospheric Environment 41, 238-252.

Browne, M. T. L., Gibbons, M. P. M., Gamble, S., Galsworthy, J., 2013. Wind loading on tilted roof-top solar arrays: The parapet effect. Journal of Wind Engineering and Industrial Aerodynamics 123, 202-213.

Cao, J., Yoshida, A., Saha, P., Tamura, Y., 2013. Wind loading characteristics of solar arrays mounted on flat roofs. Journal of Wind Engineering and Industrial Aerodynamics 123, 214-225.

Chung, K. M., Chang, K. C., Chou, C. C., 2011. Wind loads on residential and large-scale solar collector models. Journal of Wind Engineering and Industrial Aerodynamics 99, 59-64.

Chung, K., Chang, K., Liu, Y., 2008. Reduction of wind uplift of a solar collector model. Journal of Wind Engineering and Industrial Aerodynamics 96, 1294-1306.

ESDU, 1982. Strong winds in the atmospheric boundary layer. Part 1: Mean hourly wind speeds. Engineering Sciences Data Unit Number 82026.

ESDU, 1983. Strong winds in the atmospheric boundary layer. Part 2: Discreet gust speeds. Engineering Sciences Data Unit Number 83045.

Franke, J., Hellsten, A., Schlunzen, H., Carissimo, B., 2007. Best practice guideline for the CFD simulation of flows in the urban environment. COST Action 732; Quality assurance and improvement of microscale meteorological models.

Issa, R. I., 1986. Solution of implicitly discretized fluid flow equations by operator splitting. Journal of Computational Physics 62, 40-65.

Jubayer, C. M., Hangan, H., 2014. Numerical simulation of wind effects on a stand-alone ground mounted photovoltaic (PV) system. Journal of Wind Engineering and Industrial Aerodynamics 134, 56-64.

Karava, P., Jubayer, C.M., Savory, E., 2011. Numerical modelling of forced convective heat transfer from the inclined windward roof of an isolated low-rise building with application to photovoltaic/thermal systems. Applied Thermal Engineering 31, 1950-1963.

Karava, P., Jubayer, C. M., Savory, E., Li, S., 2012. Effect of incident flow conditions on convective heat transfer from the inclined windward roof of a low-rise building with application to photovoltaic-thermal systems. Journal of Wind Engineering and Industrial Aerodynamics 104-106, 428-438.

Kopp, G. A., Farquhar, S., Morrison, M. J., 2012. Aerodynamics mechanisms for wind loads on tilted, roof-mounted, solar arrays. Journal of Wind Engineering and Industrial Aerodynamics 111, 40-52.

Kopp, G. A., Banks, D., 2013. Use of wind tunnel test method for obtaining design wind loads on roof-mounted solar arrays. Journal of Structural Engineering 139, 284-287.

Kopp, G. A., Surry, D., Chen, K., 2002. Wind loads on a solar array. Wind and Structures 5, 393-406.

Menter, F. R., 1994. Two-equation eddy-viscosity turbulence model for engineering applications. American Institute of Aeronautics and Astronautics (AIAA) Journal 32, 1598-1605.

Meroney, R. N., Neft, D. E., 2010. Wind effects on roof-mounted solar photovoltaic arrays: CFD and wind-tunnel evaluation. The Fifth International Symposium on Computational Wind Engineering, Chapel Hill, North Carolina, USA.

National Building Code of Canada, 2010. National Research Council of Canada, Ottawa, Canada.

Pratt, R. N., Kopp, G. A., 2013. Velocity measurements around low-profile, tilted, solar arrays mounted on large flat-roofs, for wall normal wind directions. Journal of Wind Engineering and Industrial Aerodynamics 123, 226-238.

Radu, A., Axinte, E., 1989. Wind forces on structures supporting solar collectors. Journal of Wind Engineering and Industrial Aerodynamics 32, 93-100.

Radu, A., Axinte, E., Theohari, C., 1986. Steady wind pressures on solar collectors on flat-roofed buildings Journal of Wind Engineering and Industrial Aerodynamics 23, 249-258.

REN 21, 2014. Renewables 2014 Global Status Report. REN 21 Secretariat, Paris, France.

Roache, P. J., 1994. Perspective: A method for uniform reporting of grid refinement studies. Journal of Fluids Engineering 116, 405-413.

SEAOC, 2012. Wind loads on low profile solar photovoltaic systems on flat roofs, Report SEAOC-PV2-2012.Structural Engineers Association of California.

Shademan, M., Barron, R. M., Balachandar, R., Hangan, H., 2014. Numerical simulation of wind loading on ground-mounted solar panels at different flow configurations. Canadian Journal of Civil Engineering 41, 728-738.

Spalart, P. R., Jou, W-H., Strelets, M., Allmaras, S. R., 1997. Comments on the feasibility of LES for wings, and on a hybrid RANS/LES approach, First AFOSR International Conference on DNS/LES, Ruston, LA, 4–8 August. In Advances in DNS=LES, Liu C, Liu Z (eds). Greyden Press: Columbus, OH, 1997.

Stathopoulos, T., Zisis, I., Xypnitou, E., 2014. Local and overall wind pressure and force coefficients for solar panels. Journal of Wind Engineering and Industrial Aerodynamics 125, 195-206.

Warsido, W. P., Bitsuamlak, G. T., Barata, J., 2014. Influence of spacing parameters on the wind loading of solar array. Journal of Fluids and Structures 48, 295-315.

Weller, H. G., 2005. Derivation, modelling and solution of the conditionally averaged two-phase flow equations. OpenCFD Ltd.

Wood, G. S., Denoon, R. O., Kwok, K. C. S., 2001. Wind loads on industrial solar panel arrays and supporting roof structure. Wind and Structures 4, 481-494.

Yang, Y., Gu, M., Jin, X., 2009. New inflow boundary conditions for modelling the neutral equilibrium atmospheric boundary layer in SST k-ω model. The Seventh Asia Pacific Conference on Wind Engineering, Taipei, Taiwan, November 8-12.

Chapter 5

CFD analysis of convective heat transfer from ground mounted solar panels

5.1 Introduction

Electrical efficiency of photovoltaic (PV) solar panels is greatly dependent on the PV cell temperature. According to Evans (1981), the electrical efficiency of silicone cell photovoltaic (PV) module reduces by 0.45% per degree temperature rise. Skoplaki and Palyvos (2009) analyzed the existing correlations between the operating temperature and the electrical efficiency of commercial grade silicone cell PV modules in detail and observed that the decrease in the electrical efficiency of the solar module with the rise of operating temperature follows a linear trend. An accurate prediction of solar panel temperature is therefore necessary for the estimation of the potential electrical output of the PV panel.

To measure or estimate the PV panel temperature, thermal energy balance of the entire solar panel system is required. Major parameters related to the thermal energy balance of a ground mounted PV system are shown in Figure 5.1. The incoming energy flux in the given system is the solar irradiance. A portion of this energy is reflected from the panel upper surface. The fraction of energy absorbed by the panel is converted into electrical energy and rest is converted into heat. This heat exits from upper and lower surfaces of the panel as convective and radiative heat losses. Convective heat loss is the dominant mode among two and is a strong function of the wind behaviour that flows over the panel (Karava et al., 2011). PV panels are normally installed on the roof tops or mounted on the ground as stand-alone units. Extensive studies have been performed to determine wind induced convective heat transfer from PV panels flush mounted on inclined roofs of low-rise buildings (e.g., Kind et al., 1983; Shakerin, 1987; Sharples and Charlesworth, 1998; Mittelman et al., 2009; Karava et al., 2011, 2012). However, due to significant difference in the wind flow behaviour around the roof-mounted and ground-mounted panels, the heat transfer characteristics from the study of roof-mounted panels cannot be applied to that on the ground-mounted stand-alone panels.

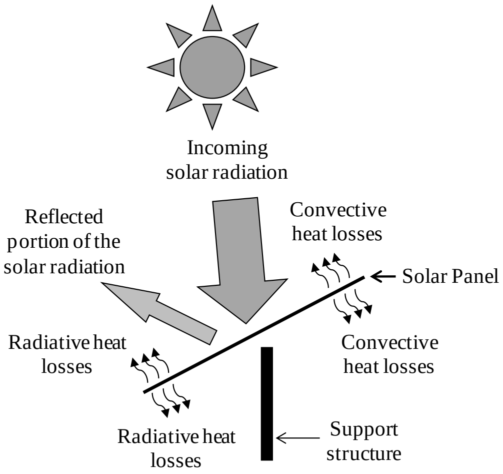

Figure 5.1: Thermal energy balance of a stand-alone ground mounted solar panel.

There is a scarcity of studies investigating the convective heat transfer due to wind from the ground-mounted stand-alone PV systems. The closest to such configuration is the inclined flat plate and several studies, two to three decades ago, have investigated the heat transfer from inclined plates as a classical heat transfer problem. Sparrow and Tien (1977) performed a wind tunnel experiment to determine the forced convective heat transfer from a flat square plate with varying inclination (25^o, 45^o, 65^o, 90^o) and yaw (0^o, 22.5^o, 45^o) angles. Reynolds number (Re) was varied from 2×10^4 to 1×10^5. A correlation of Convective Heat Transfer Coefficient (CHTC) with Re was provided. However, the Turbulence Intensity (TI) in the test section of the wind tunnel was only 0.2% which is significantly lower than the real environment. For forced convection over flat plate, lower turbulence level results in lower CHTC which has been shown by previous researchers (Simonich and Bradshaw, 1978; Maciejewski and Moffat, 1992). Test and Lessmann (1980) investigated the convective heat transfer from the surfaces of a rectangular body with inclinations from 0^o to 50^o at 10^o intervals, through wind tunnel measurements. The chord to thickness ratio was 6 and is lower than the typical current PV systems whose aspect ratios range from about 15 to 90. Laminar flow was observed on the upper surface of the body for inclinations higher than 30^o which might be due to the low free stream turbulent intensity (2.5%). Furthermore, both studies by Sparrow and Tien (1977) and Test and Lessmann (1980), were performed with uniform incoming flow rather than the Atmospheric Boundary Layer (ABL) flow and hence, the upstream conditions were substantially different from that experienced by ground-mounted panels. One of the very few studies that considered full scale test in the real environment was by Test et al.

(1981). In this full scale experiment, heat transfer behaviour from the top surface of an isolated flat plate with 40^o inclination angle was estimated. However, the mounting location of the plate (roof or ground) was not reported. About 200% higher heat transfer values were observed when compared with previous wind tunnel measurements and was believed to be due to the significantly higher free stream turbulence (20% to 50%) in the natural environment than that in the wind tunnel tests. List of existing CHTC correlations can be found in Palyvos (2008) and Defraeye et al. (2011).

The above literature review highlights the lack of scientific investigation of convective heat transfer from ground mounted stand-alone PV systems. Such investigations are needed to estimate the panel temperature and thus the panel's efficiency by performing a complete thermal energy balance of the system. The present study is undertaken to investigate the wind induced convective heat transfer from the surfaces of a ground mounted stand-alone PV system immersed in the ABL using Computational Fluid Dynamics (CFD) approach under varying wind directions (0^o and 180^o). For both wind directions, three different Reynolds numbers (1.0×10^5, 5.5×10^5 and 1.1×10^6), based on the wind speed at the panel height (H) and the length scale equal to the panel breadth (B), are considered.

5.2 CFD model

5.2.1 Solar panel geometry

The stand-alone solar panel system used in the present study consists of 24 individual PV modules. Each PV module has dimensions of 1.2 m (length) × 0.6 m (width) × 0.007 m (thickness). These 24 panels are arranged in an array of 4 rows and 6 columns making the overall dimensions of the stand-alone solar PV system equal to 2.48 m (B) × 7.29 m (W) × 1.65 m (H) (see Fig. 5.2). The PV system has 25° inclination (θ) which is the tilt angle for most of the solar farms at latitudes between 30° and 45° (e.g., 97 MW Sarnia solar farm in Ontario, Canada, latitude 43°; 30 MW Cimarron Solar Facility, New Mexico, USA , latitude 34°; 21 MW Blythe Solar Project, California, USA, latitude 37°).

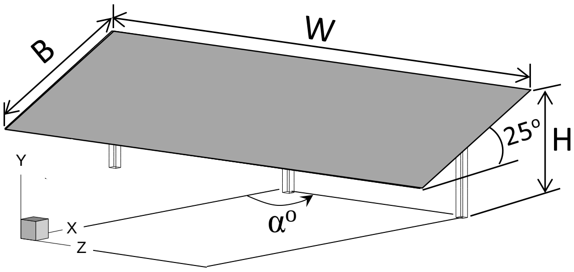

Figure 5.2: Computational model of the stand-alone PV system with wind direction (α^o) convention.

5.2.2 Computational domain and mesh

The guideline for the CFD simulation in the urban environment by Franke et al. (2007) is followed here to create the computational domain and mesh. The domain dimensions are set with reference to the panel system height, H. The domain has 5H of upstream length, 15H of downstream length, 5H between the top edge of the solar panel and the top of the domain and 9.9H clearance between the side edge of the panel and the side wall of the domain. Hence, the overall dimensions of the rectangular domain are 21.4H (X) × 6.0H (Y) × 24.2H (Z), see Figure 5.3. For this domain, the blockage ratio is about 2%. A hybrid mesh consists of 20 layers of hexahedral cells on the surface of the panel, tetrahedral cells in an interior rectangular block containing the entire panel and hexahedral cells else-where in the domain is created using Pointwise (Pointwise, Inc.). The block is used to reduce the number of tetrahedral mesh as much as possible since a combination of hexahedral – tetrahedral cells compared to a purely tetrahedral grid provides improved results (Franke et al., 2007). The first cell center height (y_p) is 50 microns from the surfaces of the solar panel which gives the dimensionless wall distance mostly $y^* < 1$ ($y^* = C_\mu^{1/4} k_p^{1/2} y_p / \nu$ where, C_μ is the turbulent model constant, k_p is the turbulent kinetic energy at the first cell center from the wall surface (m^2/s^2), y_p is the first cell center distance from the wall surface (m) and ν is the kinematic viscosity (m^2/s)) (Casey and Wintergerste, 2000) on the surfaces of the solar panel. In this study, y^* is chosen over the other commonly used dimensionless wall distance, y^+, because y^* is based on the turbulent kinetic energy and unlike y^+, does not become zero in the region of zero wall shear stress (Blocken et al., 2009). With $y^*<1$, the turbulent boundary layer is resolved all the way to the panel surface including the viscous sub-layer region and thus the use of semi-empirical “wall functions” approach is eliminated. According to Blocken et al. (2009), standard wall function over-estimates the convective heat transfer by 60% as it does not resolve the entire turbulent boundary layer. Two wind directions (α^o), 0^o and 180^o, are considered in this study relative to the panel orientation (see Fig. 5.2).

To test the grid sensitivity, three grids are generated with 998,295 (G1), 2,375,699 (G2), 4,010,931 (G3) cells for the 0^o wind direction case only. Grid refinement ratio of about 1.3 is applied in each co-ordinate direction between a coarser grid and a finer grid. The maximum expansion ratios between two consecutive cells are 1.27, 1.16 and 1.09 for G1, G2 and G3, respectively, and are within the maximum allowable ratio of 1.3 (Franke et al., 2007). Gird sensitivity study is performed for Re of 5.5×10^5 case. For grid convergence test, grids G2 and G3 are considered since the solution of the coarsest grid (G1) did not converge. The surface averaged CHTC values on upper and lower surfaces of the panel are used as the convergence criterion. Difference within 3% is observed between the two grids and hence, grid G2 is chosen for simulations in this study. Figure 5.3 shows the computational grid for 0^o wind direction with the close-up of the mesh at the lower edge of the panel in the X-Y plane view (Fig. 5.3 b). Dimensions are normalized with the solar panel height (H).

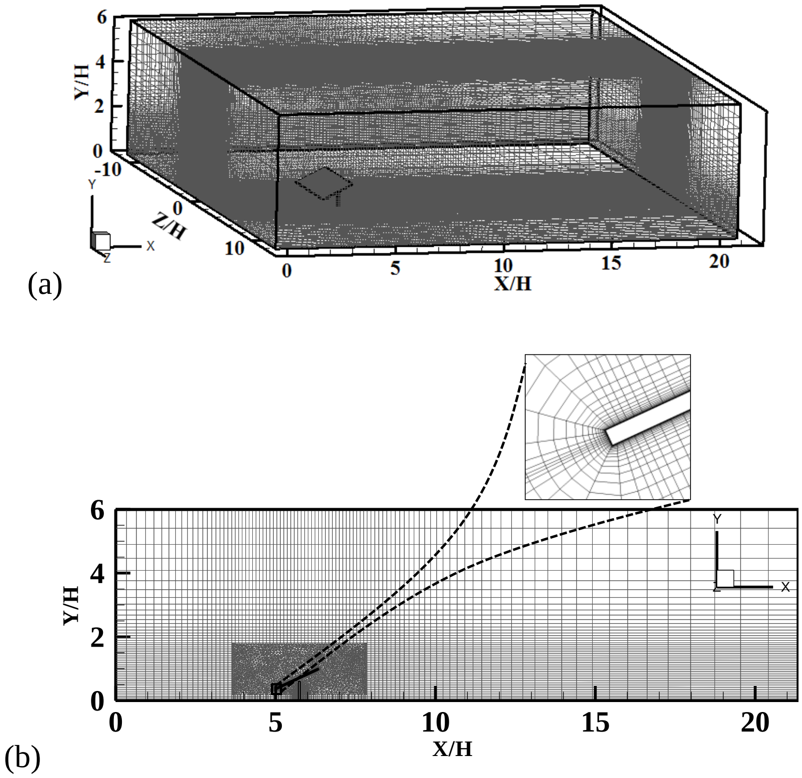

Figure 5.3: Computational grid for 0^o wind direction. (a) Isometric view (b) X-Y plane view with a close-up view of the mesh at the lower edge of the panel.

5.2.3 Boundary conditions

Mean wind speed and turbulence intensity profiles for aerodynamics roughness length (y_0) of 0.03 m (open terrain) from ESDU (ESDU 1982, 1983) are employed as the inlet boundary conditions at the domain entrance. Three different wind speeds (1, 5 and 10 m/s at 10 m height) are chosen that result in the Reynolds numbers of 1.0×10^5, 5.5×10^5 and 1.1×10^6, based on the wind speed at the panel height (H) and the length equal to the panel breadth (B). At the domain exit, a fixed uniform zero gauge pressure boundary is used. Side walls of the domain are treated as slip walls. Fixed values of velocity and turbulence properties at the top of the inlet boundary are employed throughout the top surface of the domain. Bottom of the domain is modeled as rough wall with no slip boundary condition. The panel surfaces are treated as no slip smooth walls. For the thermal boundary conditions, a typical hot summer day at locations between 30^o to 45^o latitudes is chosen. At the inlet and top planes of the domain, and support structures of the solar panel, a temperature of 303K (30^oC) is chosen whereas on the panel surfaces the temperature is set as 343K (70^oC). Overall, the whole domain is initialized with 303K temperature.

Finally, to accurately model the Atmospheric Boundary Layer (ABL) flow, it is essential to produce an equilibrium ABL (Blocken et al., 2007). Equilibrium ABL implies that the streamwise gradients of the flow parameters (e.g., velocity, turbulent kinetic energy (k), turbulence dissipation rate (ε) and specific turbulence dissipation rate (ω)) should be zero in an empty domain. To achieve an equilibrium ABL flow inside an empty domain, the same procedure as reported in Jubayer and Hangan (2014) is followed. The inlet and incident profiles of velocity and turbulence intensity in an empty domain are shown in Figure 5.4 that confirms the validity of the equilibrium ABL in the present study.

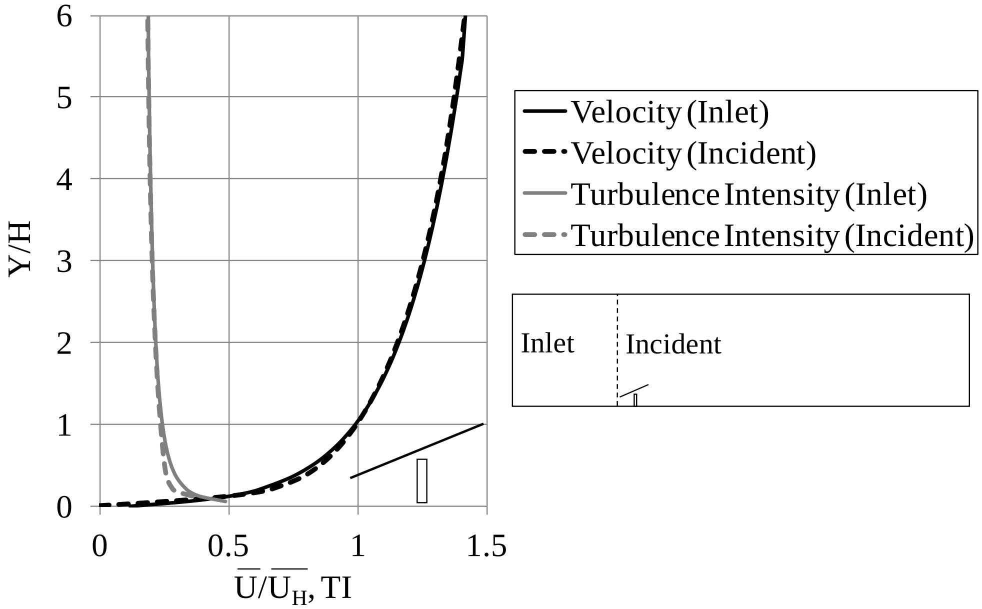

Figure 5.4: Inlet and incident velocity and turbulence intensity profiles. Here, heights (Y) are normalized with the height of the solar panel (H) and wind speeds ($\overline{U}$) are normalized with the velocity at H ($\overline{U_H}$).

5.2.4 Solver, turbulence model and numerical schemes

Open source object oriented C++ CFD code OpenFOAM 2.1.0 (ESI Group) is employed for the simulation. In this study, "buoyantBoussinesqPimpleFoam" solver by OpenFOAM is used. This solver is a transient solver for buoyant, turbulent flow of incompressible fluids and can be used for both forced and natural convection. It uses the Boussinesq approximation [$\rho_k = 1 - \beta (T - T_0)$, where ρ_k is the effective kinematic density (-), β is the expansion co-efficient (1/K), T is the field temperature (K) and T_0 is the reference temperature (K)]. The approximation is valid when $[\beta\ (T - T_0)/\ \rho_0] << 1$, where ρ_0 is the effective kinematic density at the reference temperature for the natural convection part of the heat transfer (Incropera et al., 2006). For three different Reynolds numbers considered in this study 1.0×10^5, 5.5×10^5 and 1.1×10^6, the Richardson numbers (Ri) based on wind speed at panel height (H) and the panel breadth (B) are 7.14, 0.26 and 0.06 respectively. The Richardson number represents the ratio of natural convection with respect to forced convection. The above results indicate that the lowest Reynolds number considered in this study, the natural convection is significantly dominant, while at the highest Reynolds number, the forced convection is dominant.

In this study, the Shear Stress Transport (SST) k-ω turbulence closure (Menter, 1994) is used. The SST k-ω turbulence model has been widely used for flows with adverse pressure gradient and flow separation as it performs better than the other two-equation linear eddy viscosity turbulence models (Karava et al., 2011; Shademan et al., 2014; Jubayer and Hangan, 2014). Pressure Implicit with Splitting of Operators (PISO) algorithm (Issa, 1985) is employed for the pressure velocity coupling to solve Navier-Stokes equations. A second order numerical scheme is chosen for the discretization of gradient, divergence and Laplacian terms in the equations being solved.

Linear interpolation scheme is chosen for the interpolation of values from cell center to face center. Time steps for the simulation are chosen to get the Courant number less than 1. Courant number reflects the number of cells the flow travels in a single time step and is defined as, $Cr = v\Delta t/\Delta l$ where v is the local mean wind speed (m/s), Δt is the time step (s) and Δl is the dimension of the grid cell (m). For all cases studied here, simulations are run for a non-dimensional time, t^*(= $t\overline{U_H}/B$, here t is the flow time, s) of 30. Flow statistics are calculated after t^* = 12. This duration is chosen by investigating the time history of the area-weighted average of CHTC on the surfaces of the panel. It is observed that after t^* of around 12, the initial numerical instability has not been reflected in the results.

5.3 Validation of the CFD model

Wind flow fields around the ground mounted stand-alone PV system obtained by the numerical simulations for 0^o and 180^o wind directions and for Re of 5.5×10^5 are validated against the experimental results obtained from the Particle Image Velocimetry (PIV) measurements on a 1:10 scale model of the stand-alone solar panel system in the Boundary Layer Wind Tunnel I (BLWT I) at the Western University, Canada. The Re of the incoming flow, based on the wind speed at height H and length scale of B for the experimental study was 8.3×10^4. Although there is an order of magnitude difference in the Reynolds number between the numerical model and wind tunnel experiment, for both cases complete flow separation on the leeward side of the panel is achieved. However, the complete flow separation occurred earlier in terms of Reynolds number in the wind tunnel due to the fluctuating incoming flow and higher thickness of the solar panel model (to get enough rigidity) compared to the exact 1:10 scale for the thickness of the panel. Also, once the flow field is fully turbulent and fully separated, aerodynamic characteristics of bluff bodies with sharp edges are almost insensitive to Reynolds number (Larose and D’Auteuil, 2006) and according to Tieleman (2003), “The mean flow Reynolds number equality can be relaxed for sharp-edged models, provided it does not fall below 50,000”. Measurements are taken at the plane between two support legs parallel to the side wall of the wind tunnel. Figure 5.5 shows the comparison of the normalized mean streamwise and vertical velocity profiles on the upper and lower surfaces of the solar panel, between the CFD study and PIV measurement, for both 0^o and 180^o wind directions. The results are presented at nine different locations equal distance apart from the leading edge to the trailing edge. Note that some of the profiles on the lower side of the panel from PIV experiments could not be obtained due to the interference by the solar panel support leg. For both streamwise and vertical velocity components for 0^o wind direction (Fig. 5.5 a,b), a good agreement is found between CFD and PIV results. However, close to the tunnel floor, streamwise velocity shows differences as high as 116% between the experimental and computational results. For 180^o wind direction (Fig. 5.5 c), the agreement between CFD and PIV results for the streamwise velocity is not as good as 0^o wind direction (Fig. 5.5 a), though the vertical component shows a very good agreement (Fig. 5.5 d). Overall, the observed differences between CFD and PIV results could be due to the structural elements on the experimental model of the panel which was not present in the numerical model and the thickness of the

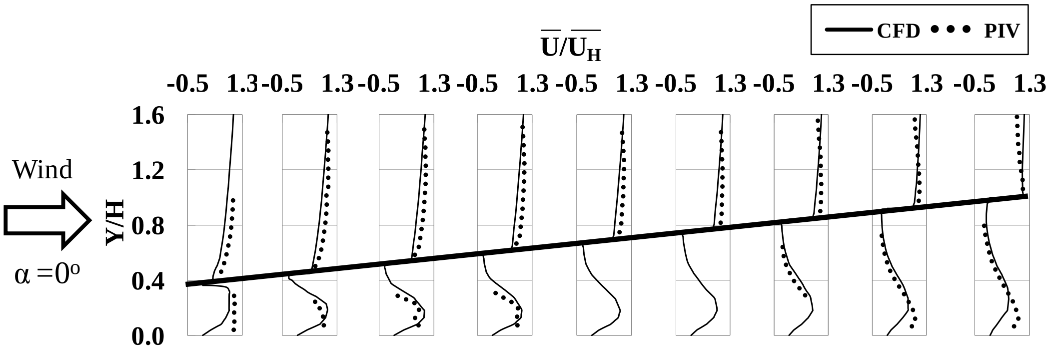

(a)

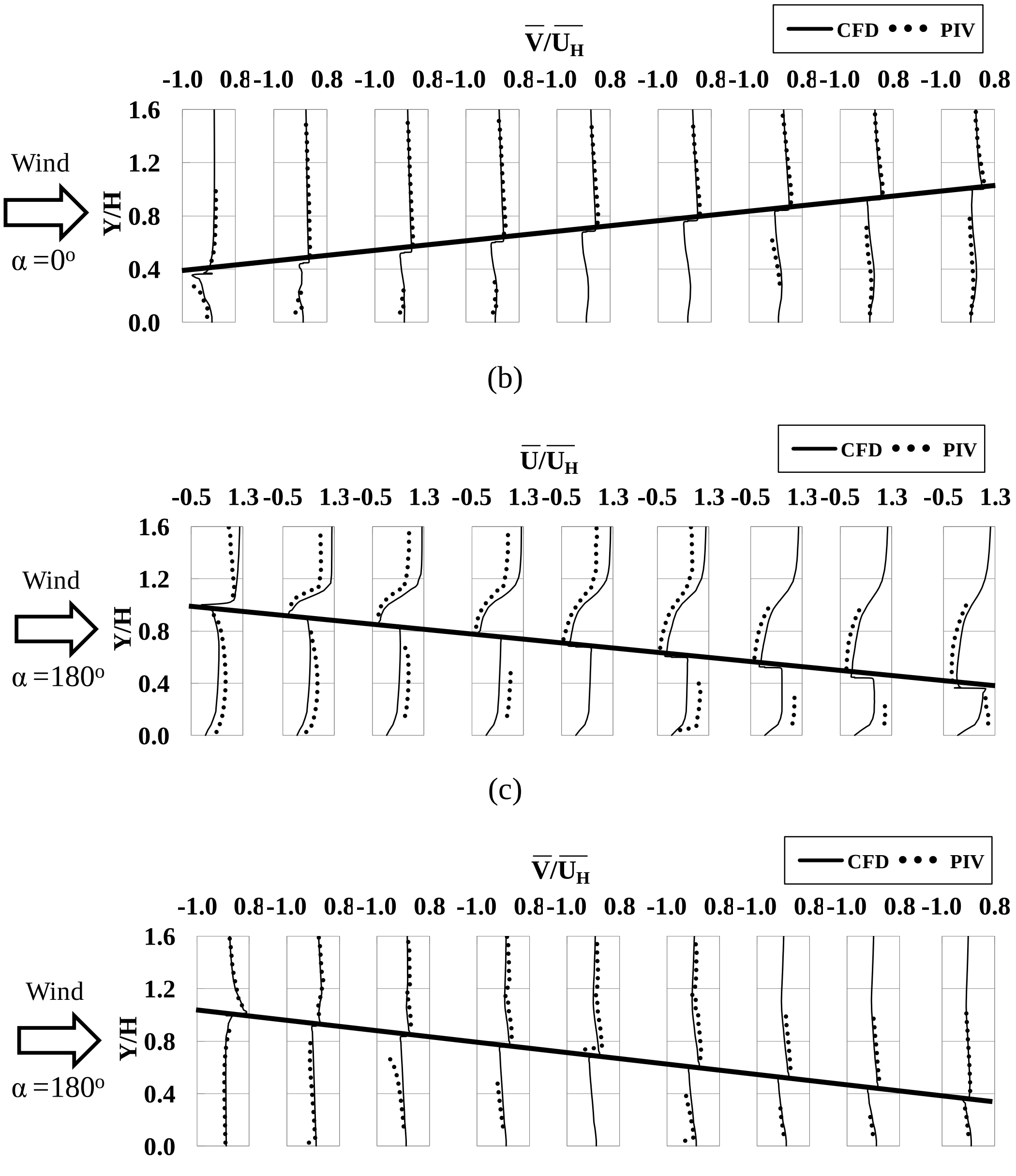

(b)

(c)

(d)

Figure 5.5: Comparison of the normalized mean streamwise ($\overline{U}$) and vertical ($\overline{V}$) velocity components on the surfaces of the solar panel between CFD and PIV for 0^o and 180^o wind directions. Here, four figures are for (a) 0^o-$\overline{U}$, (b) 0^o-$\overline{V}$, (c) 180^o-$\overline{U}$ and (d) 180^o-$\overline{V}$. Here, distances are normalized with the panel height (H) and velocities are normalized by the velocity at H in the undisturbed flow ($\overline{U_H}$).

solar panel which was higher in the experimental model than the specified geometric scaling of 1:10 to ensure that the solar panel model is rigid enough to sustain the wind. Nonetheless, the validation study showed a satisfactory agreement between the CFD and PIV in terms of mean velocities on the both upper and lower surfaces of the stand-alone solar panel.

5.4 Results and discussion

5.4.1 Convective heat transfer coefficient (CHTC)

Mean CHTC values on upper and lower surfaces of the solar panel at all three Reynolds numbers and two wind directions are shown in Figure 5.6. At the lowest Reynolds number of $1.0\times10^5$and for 0^o wind direction, both upper and lower surfaces of the solar panel have almost similar and very uniform CHTC distributions (Fig. 5.6 a). On the upper surface, about 84% of the total surface area has CHTC values within ±35% of the average value (1.25 W/m^2-K) and on the lower surface, the similar ±35% of the average value (1.10 W/m^2-K) covers about 66% of the total surface area. The results at 180^o wind direction for the same Reynolds number (Fig. 5.6 d) also showed similar uniform behaviour. For both upper and lower surfaces, CHTC values are within ±40% of the surface average value (about 1.23 W/m^2-K for both surfaces) for approximately 90% of the total surface area.

The CHTC values also increased with an increase in the Reynolds number as expected. The results also show that the values and distribution of CHTC on the upper and lower surfaces started to differ with an increase in the Reynolds number, which is due to the changes in the flow behaviour on the two surfaces. It is observed that the differences in the CHTC values on the windward and leeward surfaces increased on average by 55% and 32% as the Reynolds number increased to 5.5×10^5 and 1.1×10^6, respectively.

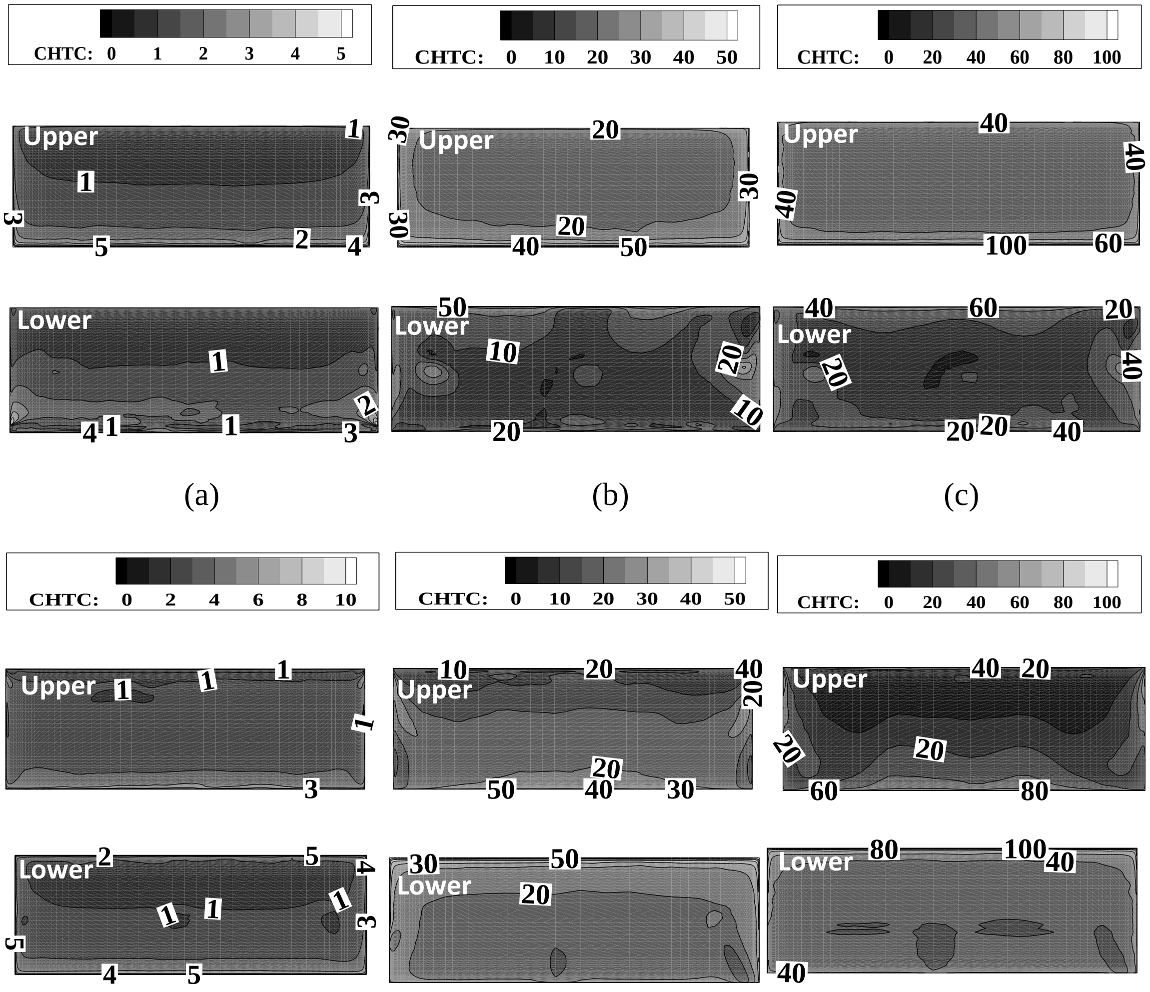

(a) (b) (c)

(d) (e) (f)

Figure 5.6: CHTC contours on the upper and lower surfaces of the solar panel for (a) Re 1.0×10^5-0° wind, (b) Re 5.5×10^5 -0° wind, (c) 1.1×10^6-0° wind, (d) 1.0×10^5-180° wind, (e) 5.5×10^5-180° wind and (f) 1.1×10^6-180° wind. For each image pair, upper contour is for the upper surface and the lower contour is the lower surface of the panel.

As expected, the CHTC values are significantly higher (up to 128%) on windward surfaces compared to leeward surfaces (Fig. 5.6 b,c,e,f) for both wind directions. Further, at higher Reynolds numbers (5.5×10^5 and 1.1×10^6), the CHTC distributions follow a very similar trend on the windward surface for both wind directions. That is, very small regions close to the leading edge and side edges have relatively higher heat transfer rate while the major portion (80 to 90%) of the total surface area up to the trailing edge has lower and relatively uniform heat transfer rate (40% difference). For 180^o wind direction however, there are small regions of low CHTC values downstream of the support legs on the windward surface (Fig. 5.6 e,f). In contrast, on the leeward surfaces (Fig. 5.6 b,c,e,f), the CHTC distribution is non-uniform with the minimum heat transfer rate around the middle of the surface for 0^o wind direction and close to the leading edge for 180^o wind direction

Figure 5.7 shows the mean CHTC profiles along the breadth (B) of the solar panel at mid-location between two support legs. The results show that except for the upper surface at 180^o wind direction between Re 5.5×10^5 and 1.1×10^6, CHTC increases with the Reynolds number. Although Re is increased from 5.5×10^5 to 1.1×10^6, CHTC on the upper surface for 180^o wind direction does not increase for about b/B = 0.6 from the leading edge. Overall, the critical case is the lowest Reynolds number case where the CHTC values are lowest, resulting in the maximum panel temperature and minimum electrical efficiency. The results also show that for a specific Reynolds number, the leeward surfaces are always have lower CHTC and hence the heat transfer rate from these surface would be lower especially when the forced convection is dominant over the natural convection.

5.4.2 Correlation between flow field and heat transfer

To better understand the CHTC behaviour described in the preceding section, streamlines around the solar panel in mid-plane between two support legs and parallel to the side edges of the panel are shown in Figure 5.8 for all cases. Streamlines for 0^o (Fig. 5.8 a) and 180^o (Fig. 5.8 b) wind direction cases at Re = 1.0×10^5 show that the flow separation-reattachment on the leeward surface occurs within a very short distance from the leading edge and hence, the flow behaviour on the leeward surface is very similar to that on the wind surface. This has resulted in almost similar CHTC distributions on both windward and leeward surfaces of the solar panel for this case. However, with an increase in the Reynolds number, the size of the separation bubble on the leeward surface increases,

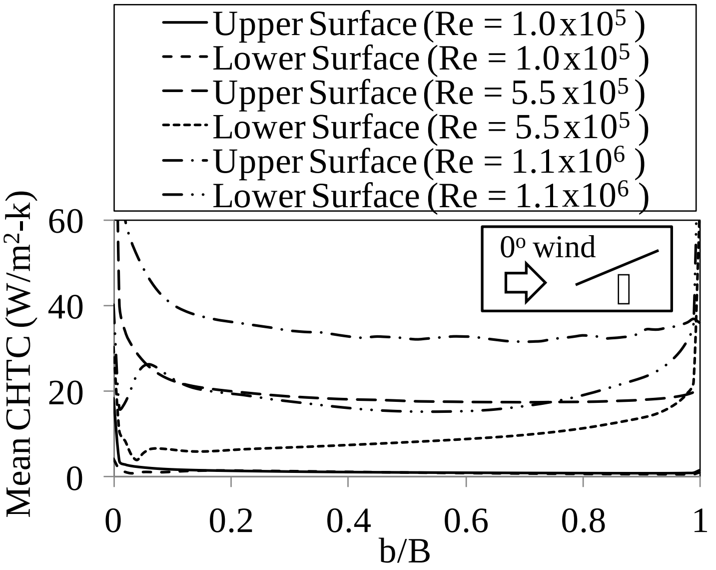

(a)

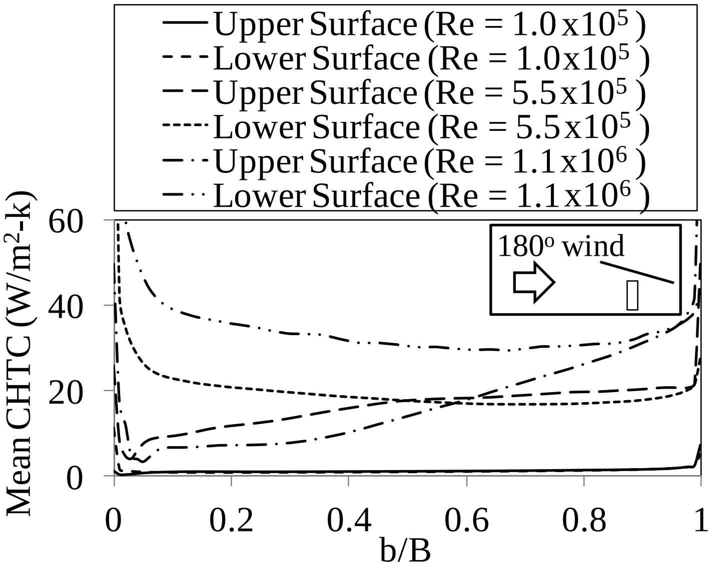

(b)

Figure 5.7: Mean CHTC profile at the line on the surfaces of the solar panel along the breadth of the panel between two support legs for (a) 0° and (b) 180° wind directions. Here, b is the local distance from the leading edge along the breadth (B) of the solar panel.

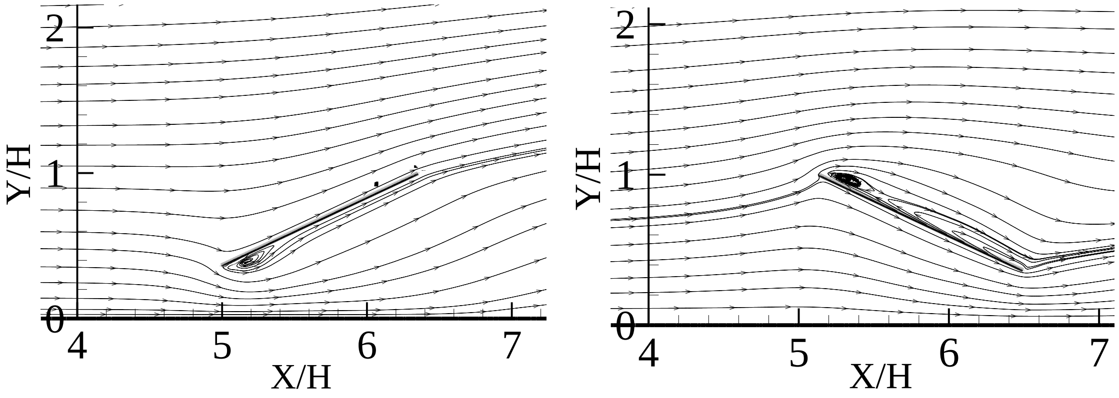

(a)

(b)

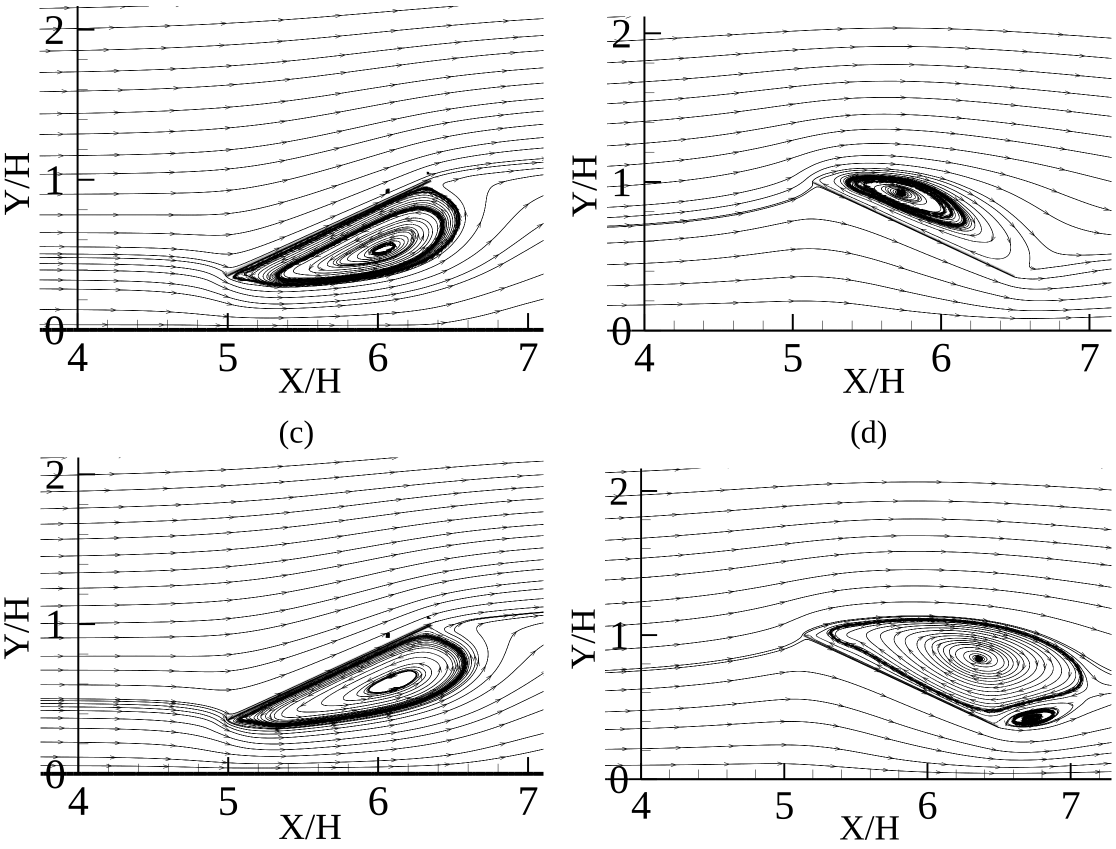

(c) (d)

(e) (f)

Figure 5.8: Streamlines at the plane between two support legs for (a) Re 1.0x10^5-0^o wind, (b) Re 1.0x10^5-180^o wind, (c) 5.5x10^5-0^o wind, (d) 5.5x10^5-180^o wind, (e) 1.1x10^6-0^o wind and (f) 1.1x10^6-180^o wind.

which envelops almost the entire leeward side of the solar panel, while the flow remains completely attach on the windward side (see Fig. 5.8 c-f). Hence the CHTC values on windward surfaces are up almost 130% higher than that on leeward surfaces. Further, the larger separation bubble for 180^o wind direction at the highest Reynolds number (1.1×10^6) compared to that at Re = 5.5×10^5 (Fig. 5.8 d,f) may have resulted in the lower CHTC values for the highest Reynolds number case described earlier in Figure 5.7 (b).

The flow patterns in Figure 5.8 provide an evidence of the substantial effect of Reynolds number on the flow around ground mounted solar panels and hence, the panel heat transfer rate.

The surface-averaged CHTC in the non-dimensional form as Nusselt number (Nu = $h_C B/k_m$, where, h_C is the convective heat transfer coefficient (W/m^2-K), B is the breadth of the panel (m) and k_m is the thermal conductivity of air (W/m-K)) versus the Reynolds number for both 0^o and 180^o wind directions is plotted in Figure 5.9. The results show that the Nusselt number on the windward surfaces for both wind directions match very closely with differences within 3%. However, the Nusselt number values on the leeward surface between 0^o and 180^o wind directions, showed a difference of up to 45% at the two higher Reynolds numbers. For the lowest Re case studied here, all Nusselt number values for both wind directions and both surfaces collapsed very closely. This is likely due to the reason that at this Reynolds number the natural convection is dominant over forced convection (as shown earlier, Ri = 7.14) and Reynolds number does not play a role in natural convection. This suggest that at lower Reynolds numbers, when natural convection is dominant over forced convection, the orientation of the panel with respect to incoming wind does not affect the average heat transfer rate from upper and lower surfaces. However, further Reynolds number values in this range need to be studied for further confirmation and also to determine a critical Reynolds number beyond which the wind direction effects start to become significant. For the Reynolds number range and wind directions studied here, Figure 5.9 can be used to estimate surface temperatures of the solar panel and thus, predict the electrical efficiency of the PV panel cautiously.

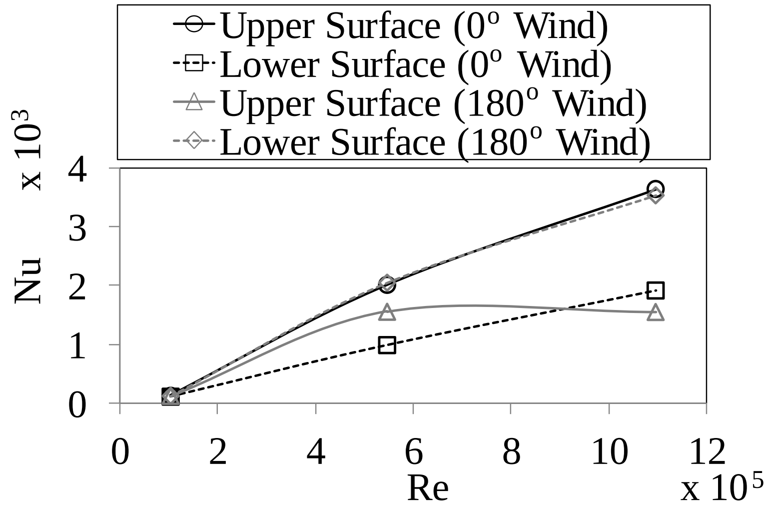

Figure 5.9: Correlation between Nusselt number (Nu) and Reynolds number (Re).

5.4.3 Comparison with existing correlations

Previous studies by Test et al. (1981), Kind and Kitaljevich (1985) and Karava et al. (2011) are chosen to compare with the present study. The work by Test et al. (1981) was for an isolated inclined (40°) solar panel on a horizontal surface. However, it was not clearly reported whether the horizontal surface was ground or horizontal roof. For 0° wind direction, they reported a correlation between CHTC (h_C) and the wind speed at 1 m above the top edge of the solar panel (U_{1m}) of the form: $h_C = 2.56U_{1m}+8.55$. The study by Kind and Kitaljevich (1985) was for an isolated inclined plate tilted at 60o on the horizontal roof of a low rise building. The correlation between heat transfer coefficient and wind speed was presented graphically. The work by Karava et al. (2011) was for the solar panel flush mounted on the windward inclined roof (30°) of a low-rise building. For open terrain roughness and 0° wind direction, they reported the correlation between Reynolds number at the eaves height (Re_{EH}) and Nu of the form: $Nu = 0.093Re_{EH}^{0.77}Pr^{1/3}$.

Although, the study by Kind and Kitaljevich (1985) and Karava et al. (2011) were for roof mounted solar panel, these studies are chosen to illustrate the effect of building on heat transfer coefficient. The comparative results between the present and previous studies are shown in Figure 5.10 for 0^o wind direction. Although the solar panel configuration used by Test et al. (1981) is similar to present study, differences in inclination angles and also the side attachments used by Test et al. (1981) to make the flow two-dimensional might be the reason for the difference in Nu values by Test et al. (1981) with the present study. Nusselt number values obtained from Kind and Kitaljevich (1985) are the lowest among the studies shown in Figure 5.10 in the forced convection region ($Re = 5.5\times10^5$ and 1.1×10^6). In the study by Kind and Kitaljevich (1985) the solar panel was in the flow separated region generated by the leading edge of the building roof and thus resulted in lower heat transfer values. Again in the forces convection region, the results show that the Nusselt number values on the windward surface of ground-mounted PV panel system (present case) is up to about 12% higher than that on the windward surface of a flushed roof-mounted PV panel system by Karava et al. (2011). Higher obstruction of flow by the low rise building compared to the stand-alone PV system and flow separation close to the leading edge on the windward roof might have resulted in lower heat transfer values on the roof compared to the ground mounted PV panel. For the natural convection case ($Re = 1.0\times10^5$), studies by Test et al. (1981) and Karava et al. (2011) may not give the correct results as the correlations provided by these studies are for forced convection. Overall, when forced convection is dominant over natural convection, heat transfer rate is higher for the ground mounted solar panels compared to the roof mounted systems.

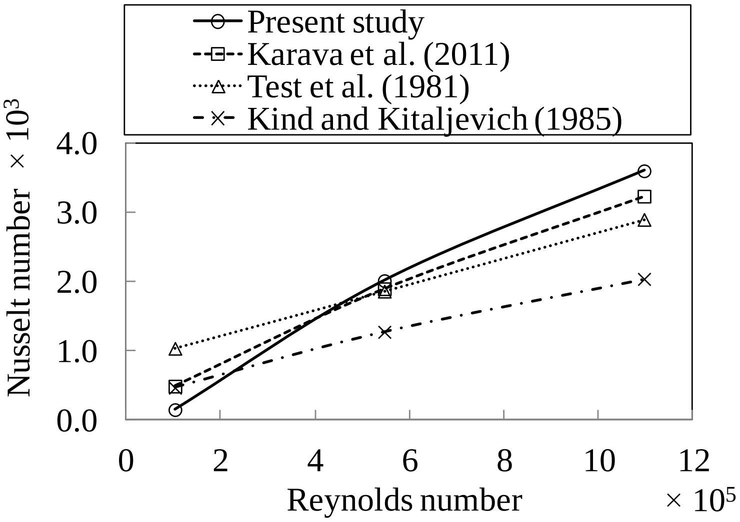

Figure 5.10: Comparison of the Nusselt number values obtained from the present study with previous studies.

5.4.4 Example case

To put the present study to practice, CHTC values obtained from this study are used to predict the solar panel surface temperature. For this purpose, the location of the 550MW Topaz solar farm: San Luis Obispo county, California, USA is chosen. The mean ambient temperature (T_{amb}) for the month of July at this location is 25°C or 298 K (The Weather Channel, LLC weather.com). Solar absorption coefficient, α_S is taken to be 0.9 (Santbergen et al., 2010) and it is assumed that convective heat loss, Q_c is about 40% of the absorbed heat flux (Karava et al., 2011). Monthly average solar insolation for the month of July at San Luis Obispo county is 7.78 kWh/m^2/day (http://www.nrel.gov/gis/data_solar.html). For the day length of about 14 hours in July, the solar flux, G is 556 W/m^2. To observe the effect of the surface orientation (windward or leeward) on the temperature, it is assumed that the total Q_c is equally divided between the upper and lower surfaces of the panel. Now using the equation, $Q_c = 0.4\alpha_S G = h_C(T_p - T_{amb})$ and CHTC (h_C) values given in Figure 5.8, distribution of the panel temperature (T_p) is obtained (Fig. 5.11). For Re of 1.0×10^5 (corresponding $U_{10m} = 1$ m/s), temperature on the surfaces of the panel for both 0^o and 180^o wind directions can reach up-to 160^oC (Fig 5.11 a,d). However, as the wind speed increases ($U_{10m} = 5$ and 10 m/s and Re of 5.5×10^5 and 1.1×10^6 respectively), significant reduction in temperature is observed, especially on windward surfaces (i.e., upper surface for 0^o wind direction and lower surface for 180^o wind direction) (Fig. 5.11 b,c,e,f). Also, on leeward sides of the panel for the Re of 5.5×10^5 and 1.1×10^6, temperatures on an average are about 5 to 10^oC higher compared to the windward surfaces. From Figure 5.11 it can be said that, for Re beyond 1.1×10^6 or $U_{10m} = 10$ m/s, temperature difference between the panel and the surrounding environment will slowly reduce. Thus to investigate the critical issues associated with the higher temperature of the panel, studies need to be focused on the lower Re ($<5.5\times10^5$) rather than higher Re cases ($>1.1\times10^6$). Various assumptions have been made while calculating the panel temperature and therefore the exercise presented in this section is strictly valid for demonstrating the utilization of energy balance of the PV system to predict the panel temperature from the heat transfer coefficient.

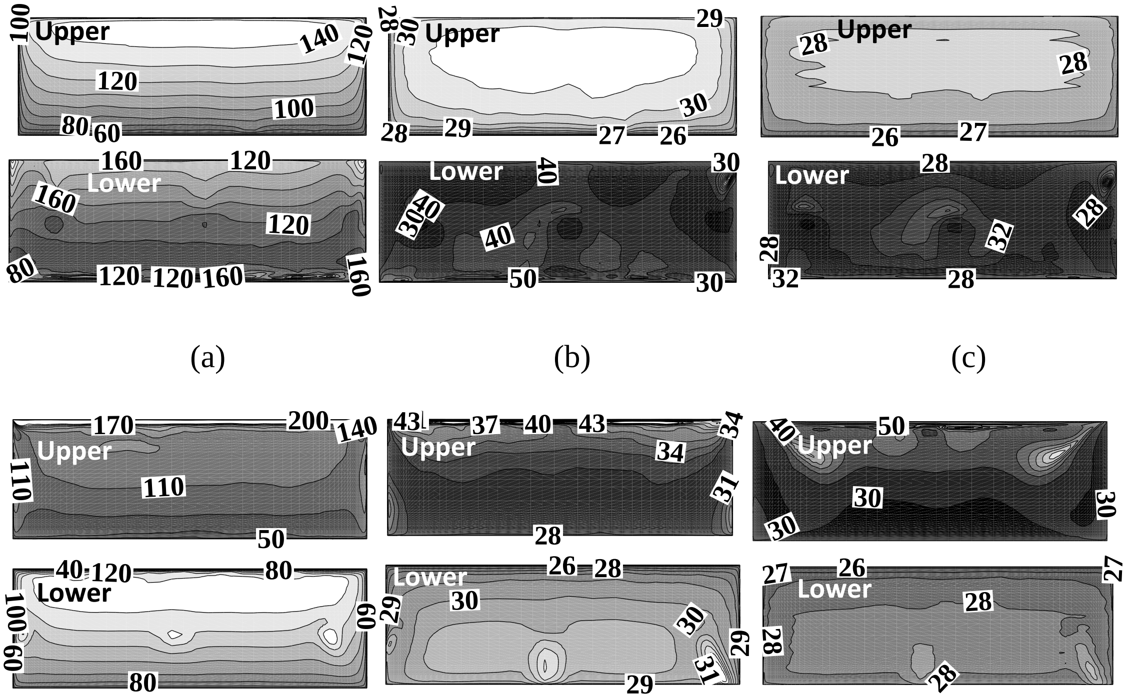

(a) (b) (c)

(d) (e) (f)

Figure 5.11: Temperature (^oC) contours on the surfaces of the panel for (a) Re 1.0×10^5-0^o wind, (b) Re 5.5×10^5 -0^o wind, (c) Re 1.1×10^6-0^o wind, (d) Re 1.0×10^5-180^o wind, (e) Re 5.5×10^5-180^o wind and (f) Re 1.1×10^6-180^o wind. For each image pair, upper contour is for the upper surface and the lower contour is the lower surface of the panel.

5.5 Conclusions

3D Reynolds Average Navier-Stokes simulations are performed to evaluate wind induced convective heat transfer from a ground mounted stand-alone solar panel with Shear Stress Transport (SST) k-ω turbulence closure. The validation experiment using Particle Image Velocimetry showed that the numerical modelling approach employed in this study predicted the mean wind speed around the solar panel reasonably well for 0^o and 180^o

wind directions. For Reynolds number (Re) of 1.0×10^5, natural convection is significantly dominant over the forced convection compared to the other two Re cases studied here, 5.5×10^5 and 1.1×10^6. Understandably, the lowest Re case is the critical case as it produces the lowest Convective Heat Transfer Coefficient (CHTC) and thus responsible for the highest temperature of the solar panel. For both 0^o and 180^o wind directions and for Re 1.0×10^5, similar CHTC distribution is observed between windward and leeward surfaces of the solar panel. However, for Re 5.5×10^5 and 1.1×10^6, up-to 130% higher CHTC is observed on the windward surfaces compared to the leeward surfaces due to the separated flow region on leeward surfaces. Nusselt number on windward surfaces for both 0^o and 180^o wind directions match very closely for all three Re studied here, which is not observed for leeward surfaces. Also, at lower Re, when natural convection is dominant over the forced convection, the heat transfer from the panel surface may not be significantly affected by the wind direction or the orientation of the solar panel. Comparison with previous studies shows that the heat transfer rate is higher for the ground mounted solar panel than the solar panel flush mounted on the inclined roof. Lastly, studies should be performed for oblique wind directions (45^o and 135^o) as well as more cases with lower Reynolds number ($< 5\times10^5$) which is considered as the critical condition, in terms of producing higher surface temperature and lower electrical efficiency of the solar panel.

References

Blocken, B., Stathopoulos, T., Carmeliet, J., 2007. CFD simulation of the atmospheric boundary layer: wall function problems. Atmospheric Environment 41, 238-252.

Blocken, B., Defraeye, T., Derome, D., Carmeliet, J., 2009. High-resolution CFD simulations for forced convective heat transfer coefficients at the façade of a low-rise building. Building and Environment 44, 2396-2412.

Defraeye, T., Blocken, B., Carmeliet, J., 2011. Convective heat transfer coefficients for exterior building surfaces: existing correlations and CFD modelling. Energy Conversion and Management 52, 512–522.

Casey, M., Wintergerste, T., 2000. ERCOFTAC Special Interest Group on ‘‘quality and trust in industrial CFD’’: best practice guidelines.

ESDU, 1982. Strong winds in the atmospheric boundary layer. Part 1: Mean hourly wind speeds. Engineering Science Data Unit Number 82026.

ESDU, 1983. Strong winds in the atmospheric boundary layer. Part 2: Discreet gust speeds. Engineering Science Data Unit Number 83045.

Evans, D.L., 1981. Simplified method for predicting photovoltaic array output. Solar Energy, 27, 555-560.

Franke, J., Hellsten, A., Schlunzen, H., Carissimo, B., 2007. Best practice guideline for the CFD simulation of flows in the urban environment. COST Action 732; Quality assurance and improvement of microscale meteorological models.

Incropera, F. P., DeWitt, D. P., Bergman, T.L. and Lavine A. S., 2006. Fundamentals of Heat and Mass Transfer. 6th edition, John Wiley & Sons. New Jersey.

Issa, R. I., 1985. Solution of implicitly discretized fluid flow equations by operator splitting. Journal of Computational Physics 62, 40-65.

Jubayer, C. M., Hangan, H., 2014. Numerical simulation of wind effects on a stand-alone ground mounted photovoltaic (PV) system. Journal of Wind Engineering and Industrial Aerodynamics. http://dx.doi.org/10.1016/j.jweia.2014.08.008i

Karava, P., Jubayer, C. M., Savory, E., 2011. Numerical modelling of forced convective heat transfer from the inclined windward roof of an isolated low-rise building with application to photovoltaic/thermal systems. Applied Thermal Engineering 31, 1950-1963.

Karava, P., Jubayer, C. M., Savory, E., Li, S., 2012. Effect of incident flow conditions on convective heat transfer from the inclined windward roof of a low-rise building with application to photovoltaic-thermal systems. Journal of Wind Engineering and Industrial Aerodynamics 104-106, 428-438.

Kind, R. J., Gladstone, D. H., Moizer, A. D., 1983. Convective heat losses from flat-plate solar collectors in turbulent winds. Transactions ASME, Journal Solar Energy Engineering 105, 80-85.

Kind, R. J., Kitaljevich, D., 1985. Wind induced heat losses from solar collector arrays on flat-roofed buildings. Journal of Solar Energy Engineering 107, 335-342.

Larose, G. L., D’Auteuil, A., 2006. On the Reynolds number sensitivity of the aerodynamics of bluff bodies with sharp edges. Journal of Wind Engineering and Industrial Aerodynamics 94, 365-376.

Maciejewski, P. K., Moffat, R. J., 1992. Heat transfer with very high free-stream turbulence. Part I - Experimental data. Journal of Heat Transfer 114, 827-833.

Maciejewski, P. K., Moffat, R. J., 1992. Heat transfer with very high free-stream turbulence. Part II – Analysis of Results. Journal of Heat Transfer 114, 834-839.

Menter, F. R., 1994. Two-equation eddy-viscosity turbulence model for engineering applications. American Institute of Aeronautics and Astronautics (AIAA) Journal 32, 1598-1605.

Mittelman, G., Alshare, A., Davidson, J. H., 2009. A model and heat transfer correlation for rooftop integrated photovoltaics with a passive air cooling channel. Solar Energy 83, 1150-1160.

Palyvos, J. A., 2008. A survey of wind convection coefficient correlations for building envelope energy systems modeling. Applied Thermal Engineering 28, 801-808.

Santbergen, R., Goud, J. M., Zeman, M., van Roosmalen, J. A. M., van Zolingen, R. J. C., 2010. The AM1.5 absorption factor of thin-film solar cells. Solar Energy Materials & Solar Cells 94, 715-723.

Shademan, M., Barron, R., M., Balachandar, R., Hangan, H., 2014. Numerical simulation of wind loading on ground-mounted solar panels at different flow configurations. Canadian Journal of Civil Engineering 41, 728-738.

Shakerin, S., 1987. Wind-related heat transfer coefficient for flat-plate solar collectors. Transaction of ASME: Journal of Solar Energy Engineering 109, 108-110.

Sharples, S., Charlesworth, P.S., 1998. Full-scale measurements of wind induced convective heat transfer from a roof-mounted flat plate solar collector. Solar Energy 62, 69-77.

Simonich, J. C., Bradshaw, P., 1978. Effect of free-stream turbulence on heat transfer through a turbulent boundary layer, Journal of Heat Transfer 100, 671-677.

Skoplaki, E., Palyvos, J. A., 2009. On the temperature dependence of photovoltaic module electrical performance: A review of efficiency/power correlations. Solar Energy 83, 614-624.

Sparrow, E. M., Tien, K. K., 1977. Forced convection heat transfer at an inclined and yawed square plate - Applications to solar collectors. Journal of Heat Transfer 99, 507-512.

Test, F. L., Lessman, R. C., 1980. An experimental study of heat transfer during forced convection over a rectangular body. Transaction of ASME: Journal of Heat Transfer 102, 146-151.

Test, F. L., Lessman, R. C., Johary, A., 1981. Heat transfer during wind flow over rectangular bodies in the natural environment. Transactions of the ASME: Journal of Heat Transfer 103, 262-267.

Tieleman, H. W., 2003. Wind tunnel simulation of wind loading on low-rise structures: a review. Journal of Wind Engineering and Industrial Aerodynamics 91, 1627-1649.

Chapter 6

Conclusions and recommendations

The work presented in this thesis is aimed towards evaluating and better understanding the effects of wind on ground mounted solar PV panels. In this regard, an extensive analysis has been performed based on numerical and experimental techniques. This chapter presents a summary on the findings of the work and it suggests directions for future development.

6.1 Conclusions

At the beginning of the study, a three dimensional (3D) unsteady numerical modelling approach with Reynolds-Averaged Navier-Stokes (RANS) simulation was developed to estimate mean wind loads (drag, lift and overturning moment) on a ground mounted solar panel as well as find correlations between the surface pressures on the panel and the wind flow around the panel for four wind directions (Southern 0^{o}, Southwest 45^{o}, Northwest 135^{o} and Northern 180^{o} winds). In order to investigate the turbulent characteristics of the flow and also to validate the numerical model, a set of experiments were conducted in the

Boundary Layer Wind Tunnel I using particle image Velocimetry (PIV) for the same wind directions as in the numerical model. Hot-wire anemometry (HWA) was also employed to characterize the flow in the wake of the solar panel. The analysis was then continued for an array of ground mounted solar panels for utility scale PV power plants applications using the numerical modelling approach. Interaction between the wind flow and each row of solar panel was examined with the evaluation of the aerodynamic forces acting on each row of the panel for the aforementioned wind directions. Acknowledging the importance of the solar panel's temperature on the electrical efficiency of the panel, higher resolution numerical simulations were also carried out to predict wind induced convective heat transfer from the surface of the solar panel. The major conclusions from this study are:

- By taking proper care of the boundary conditions and making modifications to inflow turbulence model constants, satisfactory equilibrium ABL flows can be achieved for unsteady RANS simulations.
- For the stand-alone PV system, maximum wind loads (in terms of net pressure) acted close to the leading edge of the panel regardless of wind directions studied here.
- Higher drag and lift were observed for 0^o and 180^o wind directions, whereas higher overturning moments were observed for 45^o and 135^o wind directions.
- When the mean drag and lift coefficient for 0^o and 180^o wind directions for the stand-alone system were compared with the monoslope free roof structure in

ASCE 7-10 (2010), percentage differences within 20% for load case A (ASCE 7-10, 2010) and 2% for load case B (ASCE 7-10, 2010) were observed.

- Although an unsteady solver was used, RANS modelling approach could not capture the vortex shedding from the panel. However, corner vortices were detected on the leeward side of the panel for 45^o and 135^o wind directions.
- The Particle Image Velocimetry measurements revealed the general flow structure around the PV panel and provided a detailed data-base for numerical simulations of PV panels flows.
- Among the four wind directions studied with PIV, 135^o and 180^o wind direction cases showed the maximum level of turbulence on the leeward side of the panel.
- Hot Wire Anemometry measurements detected weak vortex shedding formation with St = 0.2 only from the leading edge of the panel and for 180^o wind direction.
- Comparison between the numerical simulations with SST k-ω turbulence model and the PIV experiments showed reasonable agreement despite some differences in geometry and Reynolds number. For the array configuration and for all wind direction cases (0^o, 45^o, 135^o and 180^o), Row 1 experienced the maximum mean wind loads (drag and lift) while the leeward rows were completely shadowed by Row 1. However, higher overturning moment was found for all rows for the oblique wind direction cases.
- Heat transfer simulation for the stand-alone PV system revealed that for Reynolds number (Re) of 1.0×10^5, natural convection on the panel surface was dominant over the forced convection. This case was the most critical case among the three

Re cases studied here (1.0×10^5, 5.5×10^5, 1.1×10^6) as it produced the minimum heat transfer rate and thus it would result in the maximum panel surface temperature and lowest electrical efficiency.

- For the Re of 5.5×10^5 and 1.1×10^6, in which forced convection was dominant, up-to 130% higher convective heat transfer coefficient (CHTC) was observed on the windward surfaces than the leeward surfaces of the panel for the 0^o and 180^o wind directions.
- A correlation between dimensionless convective heat transfer coefficient, Nusselt number and Reynolds number has been established for both upper and lower surfaces of the solar panel for 0^o and 180^o wind direction cases.

6.2 Contributions

The original contributions of the present study to the scientific knowledge are provided below:

- Proper numerical modelling approach to simulate improved equilibrium (horizontally homogeneous) atmospheric boundary layer (ABL) flow. This approach can be followed in any ABL flow simulations.
- Detailed analysis of mean surface pressure coefficients in relation to the wind flow field around the solar panel both in stand-alone and array configuration under varying wind directions (0^o, 45^o, 135^o and 180^o).
- For the first time, experimental investigation of wind flow field on both windward and leeward side of a stand-alone ground mounted solar panel was performed

using particle image velocimetry (PIV) technique for four critical wind directions. These experimental results will serve as a detailed benchmark for numerical simulations.

- For the first time, correlations between dimensionless heat transfer coefficient and Reynolds number have been established for a ground mounted stand-alone PV system which will help in better approximating the solar panel temperature.

6.3 Recommendations for future work

Despite the rigorous investigations made in this thesis, there is still room for further development and improvement. In this regard, the following recommendations can be made:

- Large eddy simulation (LES) and detached eddy simulation (DES) can be carried out to numerically investigate the unsteady characteristics of the flow around ground mounted solar panels for both stand-alone and array configurations. However, proper care should be given on generating a fluctuating inlet for the LES and DES simulations (Tabor and Baba-Ahmadi, 2010).
- Wind tunnel experiments with synchronized pressure and velocity measurements are highly recommended to analyze the aerodynamic mechanisms that are responsible for peak wind loading on the ground mounted solar panels.
- For the stand-alone PV system, surface pressures and velocity field were validated with the wind tunnel experiments. However, the heat transfer results

were not validated. In this regard, a heat transfer experiment can be performed to validate the heat transfer results presented here.

- More cases with different Reynolds numbers (especially below 5.0×10^5) can be considered for the heat transfer simulation to increase the range and resolution of the heat transfer correlation established here. Wind directions other than 0^o and 180^o as well as array configuration should be considered for the heat transfer simulation in the future.

References

ASCE 7-10, 2010. Minimum Design Loads for Buildings and Other Structures. ASCE 7-10, Virginia, USA: American Society of Civil Engineers.

Tabor, G. R., Baba-Ahmadi, M. H., 2010. Inlet conditions for large eddy simulation: A review. Computers and Fluids 39, 553-567.

Appendix A

Governing equations

In this study, Reynolds-Averaged Navier-Stokes (RANS) equations with an unsteady solver are employed to solve the flow. RANS equations for an incompressible fluid with the unsteady term retained in the equation are provided below:

$$\frac{\partial \overline{\mathrm{U}}_{\mathrm{i}}}{\partial \mathrm{x}_{\mathrm{i}}} = 0 \tag{A.1}$$

$$\frac{\partial \overline{\mathrm{U}}_{\mathrm{i}}}{\partial \mathrm{t}} + \frac{\partial}{\partial \mathrm{x}_{\mathrm{j}}}\left(\overline{\mathrm{U}}_{\mathrm{i}}\overline{\mathrm{U}}_{\mathrm{j}}\right) = -\frac{1}{\rho}\frac{\partial \overline{\mathrm{P}}}{\partial \mathrm{x}_{\mathrm{i}}} + \nu\frac{\partial^{2}\overline{\mathrm{U}}_{\mathrm{i}}}{\partial \mathrm{x}_{\mathrm{j}}\,\partial \mathrm{x}_{\mathrm{j}}} - \frac{\partial \overline{\mathrm{u}_{\mathrm{i}}'\mathrm{u}_{\mathrm{j}}'}}{\partial \mathrm{x}_{\mathrm{j}}} \tag{A.2}$$

RANS equations are obtained employing the Reynolds decomposition ($\mathrm{U} = \overline{\mathrm{U}} + \mathrm{u}'$, here U is the instantaneous velocity, $\overline{\mathrm{U}}$ is the mean velocity and $\mathrm{u}'$is the fluctuating component of the instantaneous velocity) in the Navier-Stokes equation. In Equation (A.2), $\overline{\mathrm{u}_{\mathrm{i}}'\mathrm{u}_{\mathrm{j}}'}$ is called the Reynolds stress components and for a three dimensional problem, $\overline{\mathrm{u}_{\mathrm{i}}'\mathrm{u}_{\mathrm{j}}'}$ corresponds to six additional terms compared to the Navier-Stokes equation. Additional equations are needed to solve the RANS equations with these additional terms and thus the turbulence models. In this study, Shear Stress Transport (SST) k-ω turbulence model is employed. The transport equations for the SST k-ω turbulence model are as follow:

$$\frac{\partial \rho k}{\partial t}+\frac{\partial}{\partial x_j}\left(\rho \overline{U}_j k-\left(\mu+\frac{\mu_t}{\sigma_k}\right)\frac{\partial k}{\partial x_j}\right)=P_k-\beta^{*}\rho\omega k \tag{A.3}$$

$$\frac{\partial \rho\omega}{\partial t}+\frac{\partial}{\partial x_j}\left(\rho \overline{U}_j \omega-\left(\mu+\frac{\mu_t}{\sigma_\omega}\right)\frac{\partial \omega}{\partial x_j}\right)$$

$$=\alpha_n\frac{\omega}{k}P_k-\beta_n\rho\omega^2+2(1-F_1)\frac{\rho}{\sigma_{\omega 2}\omega}\frac{\partial k}{\partial x_j}\frac{\partial \omega}{\partial x_j} \tag{A.4}$$

Here, P_k is the production of turbulent kinetic energy, F_1 is the blending function and μ_t is the eddy viscosity and is defined by:

$$\mu_t=\rho\frac{k}{\omega} \tag{A.5}$$

The temperature equation for the heat transfer analysis employed in this study is also given in Equation (A.6).

$$\frac{\partial \overline{T}}{\partial t}+\frac{\partial}{\partial x_j}\left(\overline{T}\overline{U}_j\right)-\frac{\partial}{\partial x_k}\left(k_{eff}\frac{\partial \overline{T}}{\partial x_k}\right)=0 \tag{A.6}$$

where, k_{eff} is the effective thermal conductivity.

Appendix B

Comparison between SST k-ω and Realizable k-ε turbulence models

An investigation to compare the performance of two turbulence models, Shear Stress Transport k-ω (SST k-ω) and Realizable k-ε (R k-ε), has been carried out in this study for wind flow over a ground mounted stand-alone solar panel. The details of the solar panel geometry and the numerical model have already been reported in Chapter 2 of this thesis. Only the results of this comparison are shown here. Both surface pressures and wind velocities around the solar panel are compared with experimental results provided in Chapter 2 (for pressure) and Chapter 3 (for velocity). Here, 0^o wind direction is considered in this comparative study.

Mean pressure coefficients (C_p) along the mid-line on the upper and lower surfaces obtained from numerical simulations using SST k-ω and R k-ε are plotted with experimental results reported by Abiola-Ogedengbe (2013) in Figure B.1. On the upper surface of the solar panel, clearly SST k-ω performed better in estimating experimental mean C_p values than R k-ε. On an average, R k-ε overestimated mean C_p values by around 83% than the SST k-ω turbulence model. However, on the lower surface, it is not too evident which turbulence model performed better in predicting experimental values. For the lower surface, the percentage differences between the experimental values and the numerical values on an average are about 19% with SST k-ω and 21% with R k-ε turbulence models.

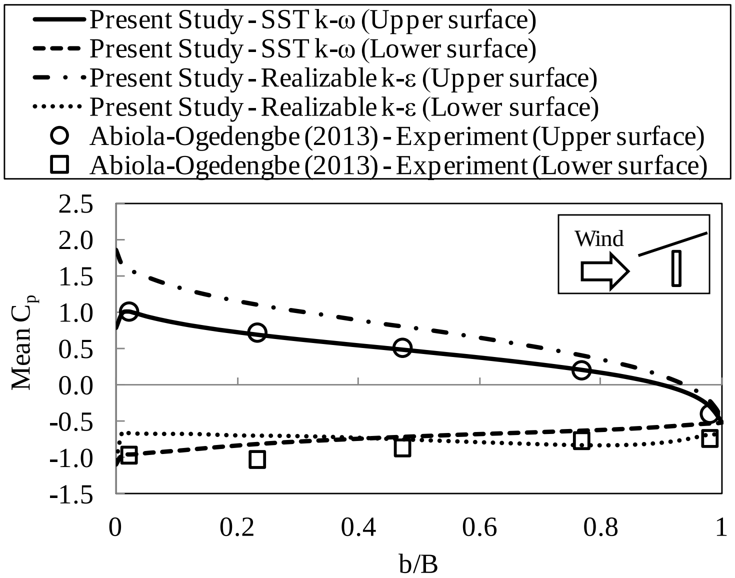

Figure B.1: Mean C_p profiles along the mid-line of the panel surface. Here, b is the distance from the leading edge along the breadth of the solar panel.

Mean streamwise and vertical velocity profiles on the panel surfaces obtained with SST k-ω and R k-ε turbulence models are compared with the PIV results reported in Chapter 3 (Fig. B.2). In total 8 profiles (at B/8 distance interval, B is the panel breadth) are plotted on each of the upper and lower surfaces of the panel. For the streamwise velocity component, on the upper surface of the panel, profiles from SST k-ω and R k-ε are

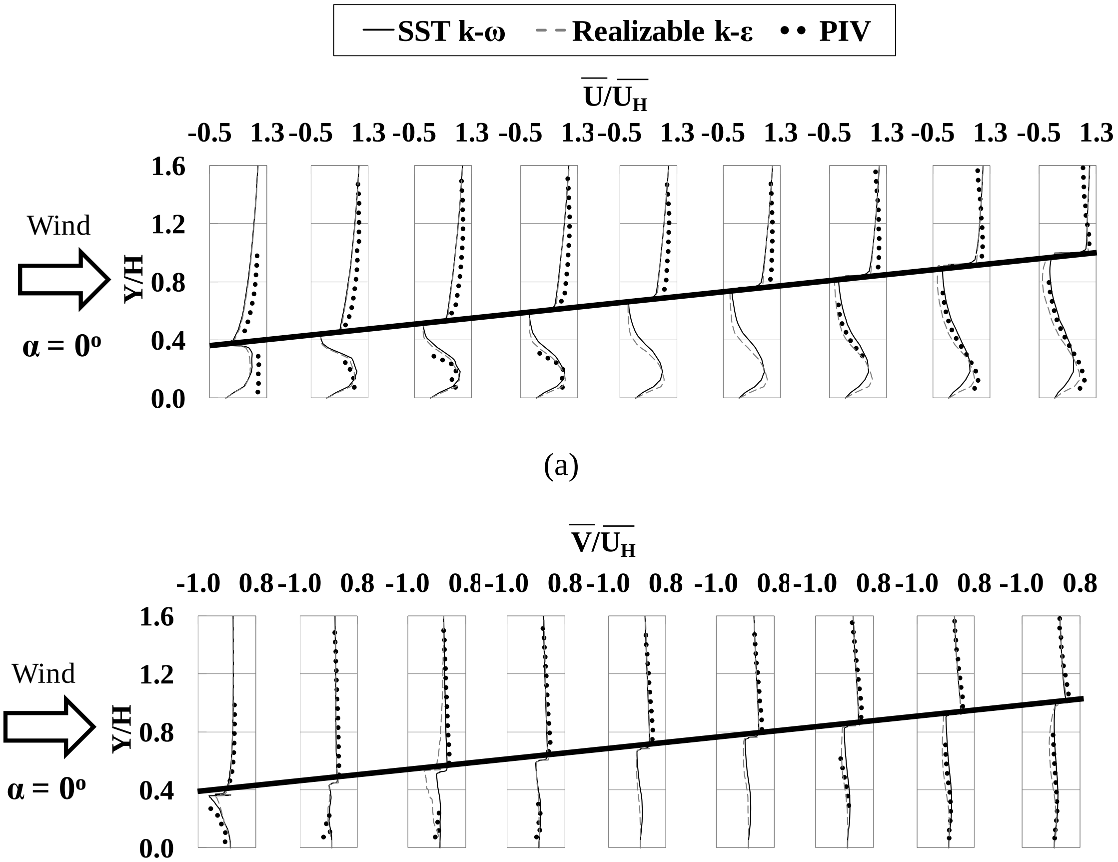

(a)

(b)

Figure B.2: Normalized mean (a) streamwise ($\overline{U}$) and (b) vertical ($\overline{V}$) velocity profiles on the solar panel. Here, $\overline{U_H}$ is the mean streamwise velocity at height H.

almost overlapped with each other without any significant differences (Fig. B.2 a). For the same velocity component, on the lower surface of the panel, differences between SST k-ω and R k-ε increase gradually from the leading edge towards the trailing edge of the panel. For the profile at the trailing edge on the lower surface, R k-ε performs better close to the ground surface whereas SST k-ω performs better close to the panel surface when compared with the PIV results. Now, for the vertical velocity components, no significant differences are observed between SST k-ω and R k-ε on both upper and lower surfaces of the panel (Fig. B.2 b), except the profile at 3B/8 from the leading edge, where the agreement between SST k-ω and PIV is better than R k-ε turbulence model. The general conclusion from this study is: SST k-ω is a better choice than R k-ε turbulence model for simulating flow around stand-alone ground mounted solar panel.

Appendix C

Modification of turbulence model constants

In the commercial CFD tool boxes such as in OpenFOAM, standard turbulence model constants are used by default. To have an equilibrium ABL flow inside an empty domain, turbulence model constants should be modified according to the flow conditions. In this study SST k-ω turbulence model is considered and a list of all the constants used in the turbulence models is given in Table C.1.

Table C.1: SST k- ω turbulence model constants.

σ_{k1}	σ_{k2}	$\sigma_{\omega 1}$	$\sigma_{\omega 2}$	β_1	β_2	β^*	γ_1	γ_2	a_1	c_1

In the SST k- ω turbulence model constants, subscript 1 and 2 refer to the near-wall region and outer region respectively. β^* in this model is actually C_μ, which is a model constant for Standard k-ε turbulence model (Johansson, 2002) and can be calculated using Equation (C.1) (Gorle et al., 2009).

$$\beta^* = C_\mu = \frac{u_*^4}{A\ln(y_P + y_0) + B} \tag{C.1}$$

where, u* is the friction velocity (m/s), y_p is the wall adjacent cell center height (m) and y_0 is the aerodynamics roughness height (m). A and B in equation (C.1) are calculated based on turbulent kinetic energy (k) profile matching with equation (C.2) as described in Gorle et al. (2009).

$$k(y) = \sqrt{A\ln(y + y_0) + B} \tag{C.2}$$

Here, y is the vertical distances (m). Standard constants values for σ_{k1} (1.176), $\sigma_{\omega 1}$ (2.0), σ_{k2} (1.0), $\sigma_{\omega 2}$ (1.168), a_1 (0.31) and c_1 (10.0) are used. Other constants are calculated using the following equations (Johansson, 2002).

$$\beta^*/\beta_1 = 1.2 \tag{C.3}$$

$$\gamma_1 = \beta_1/\beta^* - \kappa^2/\left(\sigma_{\omega 1}\sqrt{\beta^*}\right) \tag{C.4}$$

$$C_2 = 1 + \beta_2/\beta^* \tag{C.5}$$

$$\gamma_2 = \beta_2/\beta^* - \kappa^2/\left(\sigma_{\omega 2}\sqrt{\beta^*}\right) \tag{C.6}$$

where, C_2 is the same as in S k-ε model, 1.92.

Appendix D

PIV error calculation

According to Cowen and Monismith (1997), accuracy of Particle Image Velocimetry (PIV) is affected by the particle size, dynamic range, seeding density, out-of-plane motions, gradient strength and interpolation error. Figures 5 (a-f) in Cowen and Monismith (1997) provided the expected errors in the PIV results due to the aforementioned parameters. Overall, Cowen and Monismith (1997) categorized the error in three different types; gradient biasing, tracking biases and rms error. Gradient biasing is due to the in-plane loss-of-correlation, tracking biases is associated with the biased estimate of the sub-pixel fit estimators to locate the center of the correlation peak and the rms error is the uncertainty due to the random noises (e.g., light quantization, CCD dark current, particle blocking, etc.). Errors associated with the different parameters in the present PIV study are described below.

Particle size:

The size of the olive oil particle in this study was about 1 μm which is equivalent to 0.011 pixel. However, the smallest particle size in Fig 5 (a) in Cowen and Monismith

(1997) is 1 pixel. So, error for particle size of 1 pixel is used in this uncertainty analysis.

Error related to particle size, $\varepsilon_{ps} = (-0.03) + 0.095 = 0.065$ pixels

However, an additional 30% error was estimated by Refan (2014) to better predict the error for the particle size of 0.0117 pixel.

$$\varepsilon_{ps} = 1.3 \times 0.065 = 0.0845 \text{ pixels}$$

Dynamic range:

Dynamic range for CMOS image sensor type cameras can be up-to 154 counts. From Figure 5 (b) in Cowen and Monismith (1997), error in PIV due to dynamic range is almost constant for dynamic range over 55.

Error related to dynamic range, $\varepsilon_{dr} = (-0.03) + 0.08 = 0.05$ pixels

Seeding density:

Seeding density changes from one image to the other and so the number of particles in a 32x32 window. However, assuming an approximate average of 30 particles in a 32x32 window, error from Figure 5 (c) in Cowen and Monismith (1997) is given below.

Error related to seeding density, $\varepsilon_{sd} = (-0.03) + 0.05 = 0.02$ pixels

Out-of-plane motions:

In the measurement area, the thickness of the laser sheet was about 3 mm which is equivalent to 33 pixels. The maximum in plane pixel displacement in this experiment was about 15 pixels which is lower than the thickness of the laser sheet. Therefore, the error due to out-of-plane motion of particles is considered negligible. The maximum in plane pixel displacement was obtained from the first windward measurement frame for 0^o wind direction.

Gradients:

Figure 5 (e) from Cowen and Monismith (1997) is used to calculate mean and rms error due to the velocity gradient. Based on the maximum velocity gradient (du/dy = 27.46 s^{-1}), the corresponding error is the following:

Error related to velocity gradient, $\varepsilon_g = (-0.005) + 0.01 = 0.005$ pixels

Interpolation error:

Error associated with the Adaptive Gaussian Window (AGW) interpolation is calculated using Figure 5 (f) in Cowen and Monismith (1997). Only rms error was reported in Figure 5 (f) as the mean results were unaffected. Error is obtained for the maximum dynamic range of 154.

Interpolation error, $\varepsilon_{AGW} = 0.08$ pixels

The total error is calculated by adding all the aforementioned error, which is,

Total error = 0.2395 pixels

Therefore, the total error in terms of velocity is 0.12 m/s, which is 2.4% of the mean wind speed at height H from the tunnel floor ($\overline{U_H}$).

Appendix E

HWA error calculation

Uncertainty analysis of the mean velocity measured with the hot-wire anemometry during the experiment is presented here.

Precision error

Precision error or random error is caused by a lack of repeatability in the output of the measuring system. If the sample size is too small, precision errors of individual samples will affect the average value. If the sample size is large (n>30, where n is the number of samples), the distribution for the mean velocity is normal. This normal distribution is used to calculate a confidence interval for the mean velocity. The precision uncertainty interval is found from the following equation,

$$\bar{\mathrm{U}} - \mathrm{S_a} \leq \mu_\mathrm{P} \leq \bar{\mathrm{U}} + \mathrm{S_a} \qquad (\mathrm{E.1})$$

where, $\bar{\mathrm{U}}$ is the sample mean, μ_P is the population mean and $\mathrm{S_a}$ is the uncertainty calculated from

$$\mathrm{S_a} = \frac{\mathrm{z}_{\alpha/2}.\mathrm{S_U}}{\mathrm{n}^{0.5}} \qquad (\mathrm{E}.2)$$

where, $\mathrm{z}_{\alpha/2}$ is the limits on the confidence intervals which is commonly available in a tabular form (Wheeler and Ganji, 2003; p 144). A sampling time of 30s is used for measuring the flow at each location during the experiment. For a 30s sample at 1 kHz, n = 30,000. $\mathrm{S_U}$ is the precision index or unbiased estimator of the population standard deviation is calculated from

$$\mathrm{S_U} = \left[\frac{\sum_{\mathrm{i}=1}^{\mathrm{n}}(\mathrm{U_i} - \overline{\mathrm{U}})^2}{\mathrm{n} - 1}\right]^{1/2} \qquad (\mathrm{E}.3)$$

Mean velocities measured at the empty wind tunnel with precision uncertainty are presented in Table E.1. Table E.2 presents the mean velocities over the windward roof with precision uncertainty. A confidence interval of 95% is used.

Table E.1: Precision uncertainty of the measurement of mean streamwise velocity at the empty wind tunnel (here, Y is the height from the wind tunnel floor and H is the panel height)

Sample	$\overline{\mathrm{U}} \pm \mathrm{S_a}$ for a 95% confidence level (m/s)
Y/H = 0.18	4.24±0.0126
Y/H = 1.00	4.97±0.0156
Y/H = 2.47	6.51±0.0162
Y/H = 6.12	8.46±0.0158

Table E.2: Precision uncertainty of the mean streamwise velocity in the wake of the solar panel at different heights (here, Y is the height from the wind tunnel floor and H is the panel height)

Sample	$\bar{U} \pm S_a$ for a 95% confidence level (m/s)	
	0^o wind direction	180^o wind direction
Y/H = 0.18	2.86±0.0162	3.06±0.0195
Y/H = 0.52	3.26±0.0178	4.42±0.0195
Y/H = 1.00	3.98±0.0158	5.31±0.0182
Y/H = 1.14	4.27±0.0172	5.43±0.0188
Y/H = 2.05	6.16±0.0166	6.39±0.0175
Y/H = 2.95	6.78±0.0170	7.10±0.0156

Bias error

Bias errors are generated from electrical noise in the environment. To reduce these errors, BNC (Bayonet Neill-Concelman) cables were shielded using plastic sleeves wrapped around the coaxial cable and junctions to avoid ground loops and noise pickup from metal-to-metal contact. According to the HWA manufacturer, the voltage from a CTA with a wire probe can be acquired and converted into a velocity sample with an uncertainty of approximately 1% with a 95% confidence interval with reference to the calibration and neglecting the uncertainty of the calibrator itself. However, with the calibrator, the uncertainty of a velocity sample increases to 3% (Dantec User Guide 9040U6163). Over a velocity calibration range of about 9 m/s, the bias error along with the calibration error is B_a = 0.27 m/s.

Data acquisition errors

The United Electronics Industries (www.ueidaq.com) WIN-10/30DS data acquisition card has 12 bit resolution for the analog-to-digital conversion of the hot-wire signals. A range of 0-5 V allows a precision of 0.3 mV.

Bias uncertainties:

Total system accuracy: ± 3.5 LSB (Least Significant Bit)

Differential non-linearity error: ± 1 LSB max

$(4.5/2^{12})\times 100 = 0.11\%$ of the full scale velocity range.

$B_b = 0.0011\times 9\ \mathrm{m/s} = 0.0099\ \mathrm{m/s}$

Gain error: ± 5 LSB

$(5/2^{12})\times 100 = 0.12\%$ of the full scale velocity range.

$B_c = 0.0012\times 9\ \mathrm{m/s} = 0.011\ \mathrm{m/s}$

Precision uncertainties:

Quantization uncertainty: ±0.5 LSB

$(0.5/2^{12})\times 100 = 0.01\%$ of the full scale velocity range

$S_b = 0.0001\times 9\ \mathrm{m/s} = 0.0009\ \mathrm{m/s}$

Noise uncertainty: 0.5%

$S_c = 0.005\times 9\ \mathrm{m/s} = 0.045\ \mathrm{m/s}$

Combining bias and precision uncertainties

$$B_U = \left(B_a^2 + B_b^2 + B_c^2\right)^{1/2} = (0.27^2 + 0.0099^2 + 0.011^2)^{1/2} = 0.27\ \mathrm{m/s}$$

$$S_U = \left(S_a^2 + S_b^2 + S_c^2\right)^{1/2} = (0.0195^2 + 0.0009^2 + 0.045^2)^{1/2} = 0.049\ \mathrm{m/s}$$

For a 95% confidence level, $z_{\alpha/2} = 1.96$ is used on the precision uncertainty,

$$W_u = \left(B_U^2 + z_{\alpha/2} \times S_U^2\right)^{1/2} = (0.27^2 + 1.96 \times 0.049^2)^{1/2} = 0.28\ \mathrm{m/s}$$

Thus, an estimate of the maximum uncertainty of the local velocity measurements is $\pm$ 0.28 m/s, which is 5.6% of mean streamwise wind speed at height H ($\overline{U_H}$).

Appendix F

Copyright agreement

Title:	Numerical simulation of wind effects on a stand-alone ground mounted photovoltaic (PV) system
Author:	Chowdhury Mohammad Jubayer,Horia Hangan
Publication:	Journal of Wind Engineering and Industrial Aerodynamics
Publisher:	Elsevier
Date:	November 2014

Copyright © 2014 Elsevier Ltd. All rights reserved.

Logged in as:
Chowdhury Jubayer

Order Completed

Thank you very much for your order.

This is a License Agreement between Chowdhury M Jubayer ("You") and Elsevier ("Elsevier"). The license consists of your order details, the terms and conditions provided by Elsevier, and the payment terms and conditions.

Get the printable license.

License Number	3505440911500
License date	Nov 10, 2014
Licensed content publisher	Elsevier
Licensed content publication	Journal of Wind Engineering and Industrial Aerodynamics
Licensed content title	Numerical simulation of wind effects on a stand-alone ground mounted photovoltaic (PV) system
Licensed content author	Chowdhury Mohammad Jubayer,Horia Hangan
Licensed content date	November 2014
Licensed content volume number	134
Licensed content issue number	n/a
Number of pages	9
Type of Use	reuse in a thesis/dissertation
Portion	full article
Format	both print and electronic
Are you the author of this Elsevier article?	Yes
Will you be translating?	No
Title of your thesis/dissertation	Wind and thermal effects on ground mounted photovoltaic (PV) panels
Expected completion date	Dec 2014
Estimated size (number of pages)	200
Elsevier VAT number	GB 494 6272 12
Permissions price	0.00 CAD
VAT/Local Sales Tax	0.00 CAD / 0.00 GBP
Total	0.00 CAD

References

Abiola-Ogedengbe, Ayodeji, 2013. Experimental investigation of wind effect on solar panels. University of Western Ontario - Electronic Thesis and Dissertation Repository. Paper 1177. http://ir.lib.uwo.ca/etd/1177.

Cowen, E. A., Monismith, S. G., 1997. A Hybrid Digital Particle Tracking Velocimetry Technique. Experiments in Fluids 22, 199-211.

Gorle, C., van Beeck, J., Rambaud, P., Van Tendeloo, G. (2009), CFD modelling of small particle dispersion: The influence of the turbulent kinetic energy in the atmospheric boundary layer. *Atmospheric Environment*, Vol. 43, pp. 673-681.

Johansson, A., 2002. Engineering turbulence models and their development, with emphasis on explicit algebraic Reynolds stress models theories of turbulence. Springer, Berlin, 253-300.

Menter, F. R., 1994. Two-equation eddy-viscosity turbulence models for engineering applications. American Institute of Aeronautics and Astronautics (AIAA) Journal 32, 1598-1605.

Maryam, R., 2014. Physical Simulation of Tornado-Like Vortices. University of Western Ontario - Electronic Thesis and Dissertation Repository. Paper 1923. http://ir.lib.uwo.ca/etd/1923

Wheeler, A. J., Ganji, A. R., 2003. Introduction to engineering experimentation. 2nd edition. Pearson Education Inc., New Jersey, USA.

CURRICULUM VITAE

Name: Chowdhury Mohammad Jubayer

Post-secondary Education and Degrees:

Western University
London, Ontario, Canada
2011-Present
Doctor of Philosophy
Civil and Environmental Engineering

Western University
London, Ontario, Canada
2008-2010
Master of Engineering Science
Mechanical and Materials Engineering

Bangladesh University of Engineering and Technology
Dhaka, Bangladesh
2003-2008
Bachelor of Science in Engineering
Mechanical Engineering

Honors and Awards:

Western Engineering Scholarship 2008-2014

University Merit Scholarship 2003-2004

Bangladesh Government Scholarship
(awarded twice) 2000-2002, 2003-2006

Related Work Experience:

Research Assistant, 2008-2014
Western University

Teaching Assistant, 2009, 2011-2014
Western University

Publications

Journal Articles and Transaction

1. Jubayer, C. M., and Hangan, H., 2014. Numerical simulations of wind effects on a stand-alone ground mounted Photovoltaic (PV) system. *Journal of Wind Engineering and Industrial Aerodynamic* 134, 56-64.

2. Karava, P., Jubayer, C. M., Savory, E., and Li, S., 2012. Effect of incident flow conditions on convective heat transfer from the inclined windward roof of a low-rise building with application to photovoltaic-thermal systems. *Journal of Wind Engineering and Industrial Aerodynamics* 104-106, 428-438.

3. Karava, P., Jubayer, C. M., and Savory, E., 2011. Numerical modelling of forced convective heat transfer from the inclined windward roof of an isolated low-rise building with application to photovoltaic/thermal systems. *Applied Thermal Engineering* 31, 1950-1963.

Conference proceedings

1. Jubayer, C. M., and Hangan, H., 2014. Numerical simulations of wind effects on an array of ground mounted solar panels. *The ASME 2014 4th Joint US-European Fluids Engineering Division Summer Meeting and 11th International Conference on Nanochannels, Microchannels and Minichannels*, Chicago, Illinois, USA, August 3-7.

2. Szeto, K. , Vogiatzis, K., Hangan, H., Jubayer, C. M., Breckenridge, C., Loewen, N., Bauman, C. and Salmon, D., 2014. Conceptual design study to determine optimal enclosure vent configuration for the Maunakea Spectroscopic Explorer (MSE). *Proceedings of SPIE 945, Ground Based and Airborne Telescope V, 91450A*, July 22.

3. Jubayer, C. M., Hangan, H., and Siddiqui, K., 2014. Numerical and experimental investigations of wind flow around ground mounted solar panels. *XIII Conference of the Italian Association for Wind Engineering*, Genova, Italy, June 22-25.

4. Jubayer, C. M., and Hangan, H., 2014. Numerical study of wind induced convective heat transfer from ground mounted solar panels. *The Sixth International Symposium on Computational Wind Engineering*, Hamburg, Germany, June 8 -12.

5. Jubayer, C. M., and Hangan, H., 2013. Numerical study of wind effects on ground mounted solar panels under varying wind directions. *1000 Islands Fluid Dynamics Meeting*, Gananoque, Ontario, Canada, April 26-28.

6. Jubayer, C. M., Abiola-Ogedengbe, A., Siddiqui, K., and Hangan, H., 2012. Numerical and experimental study of wind effects on photovoltaic (PV) panels. *3rd American Association for Wind Engineering Workshop*, Hyannis, Massachusetts, USA, August 12-14.

7. Jubayer, C. M., and Hangan, H., 2012. Wind effects on photovoltaic (PV) panels – A CFD approach. *1000 Islands Fluid Dynamics Meeting*, Gananoque, Ontario, Canada, April 27-29.

8. Jubayer, C. M., and Hangan, H., 2012. Numerical simulation of wind loading on photovoltaic panels. *ASCE Structures Congress 2012*, Chicago, Illinois, March 29-31.

9. Karava, P., Jubayer, C. M., and Savory, E., 2011. Effect of terrain on the forced convective heat transfer from the inclined windward roof of a low-rise building. *The 13th International Conference on Wind Engineering,* Amsterdam, The Netherlands, July 10-15.

10. Jubayer, C. M., Karava, P. and Savory, E., 2010. Building-integrated Photovoltaic/Thermal systems – numerical prediction of exterior convective heat transfer coefficients and parametric analysis. *First International High Performance Building Conference*, Purdue University, USA. July 12- 15.

11. Jubayer, C. M., Karava, P. and Savory, E., 2010. CFD simulations for evaluation of forced convective heat transfer coefficients on Photovoltaic/Thermal systems integrated on the windward roof surface of a low-rise building. Proceedings of *the Fifth International Symposium on Computational Wind Engineering*, Chapel Hill, North Carolina, USA, May 23-27.